

POLITECNICO DI MILANO
Department of Physics
Doctoral Programme in Physics

Coherent Raman Spectroscopy from a single femtosecond oscillator

Doctoral Dissertation of:
Vikas Kumar
Matr. 738991

Supervisor:
Prof. **Marco Marangoni**

Co-supervisor:
Prof. **Giulio Cerullo**

The Chair of the Doctoral Program:
Prof. **Franco Ciccacci**

Jan, 2012; Cycle: $XXIV^0$

"But optics sharp it needs, I ween, To see what is not to be seen."
John Trumbull, American Poet

to my parents

Acknowledgements

At the outset, I would like to express my deep indebtedness with fullest sense of gratitude to my revered Supervisor Prof. Marco Marangoni, Department of Physics, Politecnico di Milano, for his valuable guidance, incessant encouragement, expedient advices, constructive criticism and keen interest throughout the course of this study. I feel myself very fortunate for getting the opportunity to work and learn under his guidance.

With my deepest gratitude, I would like to thank my revered Co-supervisor Prof. Giulio Cerullo, Department of Physics, Politecnico di Milano, for suggesting the research problem, providing inspiring guidance and rendering a very comfortable and suitable atmosphere to work throughout the course of this research work that led to the successful completion of this arduous task.

I respectfully offer my thanks to Prof. Roberta Ramponi and Prof. Roberto Osellame for their kind co-operation and support during the course of the study.

I feel myself very fortunate for getting the opportunity to work with and learn from Alessio Gambetta during my first year of the course.

I respectfully offer my thanks to Cristian Manzoni and Dario Polli for fruitful scientific discussion with them and for their valuable suggestions and kind co-operation. It is always my pleasure to work with them.

Academic life without friends is incomprehensible. I am grateful to my friend and lab-mate Michele Casella for invaluable suggestions and earnest enthusiasm shown by him during the research work. I want to thank him for making a healthy environment in the laboratory.

I would like to thank my lab-mate and friend Egle Molotokaite for her supporting attitude.

I express my sincere thanks to my friends specially, Nicola Bellini, Andrea Crespi, Davide Gatti, Shane Eaton, Krishna Chaitanya V., Rebeca Martz, Federico Bottegoni, for all the support and help they have rendered to me irrespective of time constrains.

I respectfully offer my thanks to all the faculty members / teachers of the Department of Physics for their encouragement and co-operation in my research work.

I would like to thank all the non-teaching staff of Department of Physics, Politecnico di Milano for their kind co-operation.

From bottom of my heart, I respectfully express my thanks to my teachers Dr. T. P. S. Nathan, Dr. A. K. Singh and Prof. P. A. Naik for developing interest in Physics inside me at the beginning of my educational carrier.

I feel short of words when emotions erupt. The blessing and hardships of my parents, brother and sister and their enterprizing and unbiased support encouraged me to ensconce and cope through all situations. Acknowledging their nurturing presence in my life gives me a sense of overwhelming and greatest satisfaction, I can think for. I grope for words to express deep sense of gratitude to my brother Vishal Kumar for his affection, unflinching support and constant encouragement.

Being a human being, I must have forgotten to mention few names, for which I ask for their forgiveness.

Above all, I am thankful to God, the almighty, for carving a path where there seemed to be none in each step of my life. His presence is always more real than the reality itself whether I see it or not! There cannot be any denial to this fact as He is the very reason of my existence.

Vikas Kumar

List of publications/conference contributions

This thesis is based on following publications in journals and conference contributions:

M. Marangoni, A. Gambetta, C. Manzoni, **Vikas Kumar**, R. Ramponi, and G. Cerullo, *Fiber-format CARS spectroscopy by spectral compression of femtosecond pulses from a single laser oscillator*, **Opt. Lett. 34**, pp. 3262-3264 (2009).

Alessio Gambetta, **Vikas Kumar**, Giulia Grancini, Dario Polli, Roberta Ramponi, Giulio Cerullo and Marco Marangoni, *Fiber-format stimulated Raman scattering microscopy from a single laser oscillator*, **Opt. Lett. 35**, pp.226-228 (2010).

Vikas Kumar, R. Osellame, R. Ramponi, G. Cerullo and M. Marangoni, *Background-free broadband CARS spectroscopy from a 1-MHz ytterbium laser*, **Opt. Express 19**, pp.15143- 15148 (2011).

Vikas Kumar, M. Casella, E. Molotokaite, D. Polli, G. Cerullo, M. Marangoni, *Coherent Raman spectroscopy with a fiber-format femtosecond oscillator*, Accepted **J. Raman Spectrc.**.

Vikas Kumar, M. Casella, E. Molotokaite, P. Kukura, C. Manzoni, D. Polli, M. Marangoni and G. Cerullo, *Balanced-detection Raman induced Kerr effect microscopy*, Abstract submitted to **CLEO 2012**.

M. Marangoni, **Vikas Kumar**, C. Manzoni, A. Gambetta, R. Ramponi, and G. Cerullo, *CARS spectroscopy from a single fiber laser oscillator*, **European Conference on Lasers and Electro-Optics (CLEO) and the XIth European Quantum Electronics Conference 2009**.

M. Marangoni, A. Gambetta, **Vikas Kumar**, G. Grancini, D. Polli, C. Manzoni, R. Ramponi, G. Cerullo,*Coherent Raman Microscopy with a Fiber-Format Femtosecond Laser Oscillator*, **Conference on Lasers and Electro-Optics (CLEO) 2010**.

A. Gambetta, **Vikas Kumar**, G. Grancini, D. Polli, C. Manzoni, R. Ramponi, G. Cerullo, M. Marangoni, *Coherent Raman Microscopy with a Fiber-Format Femtosecond Laser Oscillator*, **International Conference on Ultrafast Phenomena (UP) 2010**.

Contents

Acknowledgements **v**

List of publications/conference contributions **vii**

Motivation **xiii**

1 Introduction to Coherent Raman spectroscopy **1**

1.1 Introduction to nonlinear spectroscopy techniques 2

1.2 Spontaneous Raman spectroscopy 4

1.3 Coherent Raman Spectroscopy 8

1.4 Nonlinear coupled equations for CRS processes 17

2 CARS and SRS **23**

2.1 Coherent ant-Stokes Raman Spectroscopy 23

2.1.1 The CARS process 25

2.1.2 Presence of non-resonant background in CARS and its effect 27

2.2 NRB suppression techniques 30

2.2.1 Epi-detection CARS 30

2.2.2 Counter-propagating CARS 31

2.2.3 Polarization-sensitive CARS 31

2.2.4 Frequency modulation CARS 33

2.2.5 Time-resolved CARS (TR-CARS) 35

2.2.6 Interferometric CARS (I-CARS) 38

2.3 Stimulated Raman Scattering 40

2.4 SRS vs CARS 43

2.5 Broad-band CARS 44
2.6 State of the art for CARS and SRS 46
2.6.1 Laser optimal parameters for CRS 46
2.6.2 Laser sources for CRS 48

3 Fiber-format CRS microscopy 55

3.1 Introduction 55
3.2 Experimental setup 56
3.3 CARS Experiments 60
3.4 Experiment on Interferometric-CARS 61
3.5 SRS Experiments 64
3.6 Upgraded version of the fiber-format CRS microscopy setup . . . 69
3.6.1 Experimental setup 69
3.6.2 CARS and SRS experiments 72
3.6.3 Results and discussion 72
3.6.4 Key features offered by the third amplified branch 75
3.6.5 Conclusions 78

4 NRB-free broadband CARS from a powerful ytterbium laser 79

4.1 Introduction 79
4.2 Experimental Setup 81
4.2.1 Repetition-rate advantage 83
4.2.2 Degenerate-CARS configuration 84
4.2.3 The TR-CARS configuration 86
4.3 Conclusions 87

5 Balanced-detection Raman Induced Kerr Effect spectroscopy 89

5.1 Raman Induced Kerr Effect(RIKE) 89
5.1.1 Linear RIKE 90
5.1.2 Circular RIKE 92
5.2 The polarization sensitive detection schemes for RIKE 94

5.2.1 Crossed polarizers RIKE 95
5.2.2 Optically Heterodyne Detection RIKE (OHD-RIKE) . . . 96
5.3 Balanced Detection RIKE Spectroscopy 101
5.3.1 BD-RIKE response 104
5.4 BD-RIKE experiments from a single fiber oscillator 106
5.4.1 Experimental results 108
5.5 Conclusions 111

6 Conclusions **113**

A Spontaneous Raman process **115**

B Spectral compression in periodically poled crystals **119**

C Optical Kerr Effect **125**
C.0.1 Kerr Effect 125
C.0.2 Optical Kerr Effect(OKE) 126

D Optical Heterodyne Detection **131**

E Effect of waveplate and Wollaston prism on polarized light **135**
E.1 Half waveplate and Wollaston prism 137
E.1.1 Calculations for aligning the balanced detection setup: In absence of pump 137
E.1.2 Calculations for balanced detection RIKE signal:pump is ON 139
E.2 Quarter waveplate and Wollaston prism 144
E.2.1 Calculations for aligning the balanced detection setup: In absence of pump 144
E.2.2 Calculations for balanced detection RIKE signal:pump is ON 145

Motivation

Coherent Raman Scattering (CRS) has been recognized as a very powerful approach for label-free vibrational imaging of biological species and chemical compounds with high spatial resolution and acquisition speed. The advent of its first form, Coherent Anti-stokes Raman Scattering (CARS)[1] in 1963 following the advent of laser in 1960, has paved a pathway for high speed chemical imaging by enhancing the sensitivity of Spontaneous Raman Scattering process to many orders of magnitude. Widespread applications of such techniques to vibrational imaging in biology and medicine require laser excitation setups, typically composed by two synchronized laser pulse trains called "pump" and "Stokes" at different optical frequencies focused onto the sample with the possibility to tune their frequency difference to a Raman-active vibrational frequency of the investigated sample. In this way, resonant excitation of the sample is achieved, which is used to uniquely identify its chemical composition.

Independent tunability and synchronization of the required two pulse trains impose a strict demand on laser source. In commonly used setups, it is done by exploiting two tunable free-space laser sources with their cavities being electronically synchronized. Tunable free-space lasers, for example Ti:sapphire laser and Optical Parametric Oscillators (OPOs), are inherently bulky and costly. Incorporation of such two lasers makes the overall setup bulkier, complex and costly.

In addition, since the beginning of Coherent Raman era, CARS community has been facing a serious issue associated with the process. CARS[2] in fact is accompanied by a non-resonant four-wave-mixing background, generated from other simultaneously occurring nonlinear processes, which is vibrationally insensitive and does not contain any spectral information. This non-resonant background

usually interferes with CARS signal and spectrally distorts it making it hard to distinguish between two closely spaced lines coming from different molecules. While investigating a very low concentration of molecules, the non-resonant signal can even overwhelm the CARS signal.

The two aforementioned problems initiated two research streams in the Coherent Raman field during the last quarter of the past century. The one was for the development of a reliable simplified laser source to provide synchronized pump and Stokes pulse trains. The other stream was to invent techniques to get rid of the non-resonant background. A plethora of solutions has been devised since then to remove or suppress the effect of non-resonant background. Some of them are Polarization-CARS[3; 4; 5; 6; 7; 8; 9], Interferometric CARS[10; 11; 12], Frequency Modulation CARS[13; 14], Time-resolved CARS[15], Dual pump CARS[16], Raman Induced Kerr Effect (RIKE)Spectroscopy , Optically Heterodyne Detected RIKES (OHD-RIKES)[17; 18] and the most popular widely accepted in recent years Stimulated Raman Scattering(SRS)[19]. Also for the laser source, attempts have been made to simplify the setup by using a single free-space oscillator and deriving from it inherently synchronized pump and Stokes pulses.

This thesis is devoted to the development of radically simplified CRS setups based on a single femtosecond oscillator. All setups lend themselves to the implementation of aforementioned techniques for background suppression, thanks to the possibility of deriving a third independent pulse trains synchronized to the ones used for the pump and the Stokes. In the above framework, my research activity has contributed to the development of three new approaches to CRS spectroscopy/microscopy with overall much simplified laser excitation setups.

The first approach is based on spectral compression of femtosecond pulses emitted by a compact Er-fiber oscillator. Spectral compression is achieved by group-velocity mismatched second harmonic generation in periodically-poled nonlinear crystals, and it allows efficient synthesis of synchronized narrow-bandwidth (less than $10cm^{-1}$) pump and Stokes pulses with frequency difference continuously tunable up to $3200cm^{-1}$. By taking advantage of the unique possibility of synthesizing a third phase-coherent tunable pulse, CARS signal enhancement

by up to three orders of magnitude has been demonstrated by interferometric superposition of the CARS signal with a phase-coherent local oscillator field, also synthesized by spectral compression. The developed fiber-laser based approach, besides being much more compact than commonly used laser systems, presents thus a much higher degree of versatility. The same architecture has been exploited in another experiment, in which Stimulated Raman Scattering microscopy of a sample of thin film of poly(9,9-dioctylfluorene) (PFO), blended with polymethylmethacrylate (PMMA) was performed. The developed system proved to have high sensitivity (2×10^{-7}) and spectral resolution (sub 15 cm^{-1}), while offering an unprecedented flexibility for multi-color imaging.

The second approach is mostly oriented to the solution of one of the most critical issues of CARS apparatuses as mentioned above, which is the presence of a non-resonant four-wave-mixing background. This non-resonant background significantly reduces the signal-to-noise ratio and hence lowers the detection sensitivity. In addition it interferes with the coherent Raman signal and distorts it. The problem becomes even more prominent in a broadband CARS regime. We found a solution in a three-beams non-degenerate CARS configuration where the pump, the Stokes and the probe pulses are all derived from a single high power amplified Yb-doped femtosecond laser (8W at a central wavelength λ of 1040 nm with a repetition rate of 500 kHz). A narrow-band pump ($\lambda : 520\ nm$), a broadband Stokes (500-635 nm) and a spectrally narrowed probe ($\lambda : 1040\ nm, \Delta\lambda : 1.5\ nm$) are respectively obtained by spectral compression in a periodically-poled nonlinear crystal, by white light generation in 4 mm YAG crystal, and by inline etalon line-narrowing of the laser beam. The spatially and temporally synchronized pump and Stokes pulses resonantly drive a broadband vibrational excitation, while the third narrowband delayed probe allows for the retrieval of the narrowband spectral features. The delay allows to get rid of the instantaneous nonresonant response, while preserving the CARS signal, which survives few picoseconds due to the rather long relaxation time of the vibrational levels. In this way nearly distortion-free CARS spectra are acquired at once with high S/N ratio. To check the sensitivity of our system, we have performed a dilution test of methanol in de-

ionized water, by obtaining a remarkable lower detection limit at 0.72% methanol concentration. We also acquired time-resolved CARS(TR-CARS) spectra of several solvents, with spectral resolution of 5 cm^{-1}, in very good agreement with the corresponding Raman spectra.

The third approach represents an advancement over the first approach based on spectral compression of pulses emitted by an amplified Er-fiber oscillator. The new setup can be quickly reconfigured in order to address either CARS or SRS or RIKE spectroscopy/microscopy. Such an increased flexibility derives from a new fiber laser equipped with a third amplified branch that makes it possible to generate a third beam to be employed either for the simultaneous detection of multiple molecular species, and/or for the implementation of NRB suppression techniques in CARS. Provided microscope objectives with near-infrared antireflection-coating are used, the available power levels of the new laser source, i.e. 100 mW for the pump and 10mW for the Stokes at 40 MHz repetition frequency, allow for state-of-the-art performances both in the CARS and SRS configurations. Optionally, by exploiting the inherently broad bandwidth of the laser pulses and supercontinuum generation processes in a highly nonlinear fiber, broadband Stokes pulses can be synthesized, giving access to a multiplex CRS regime in which a wealth of molecular signatures can be addressed at once. The spectra of several solvents were acquired in order to test the performances of the system and to compare them with those obtained with the previous dual-branch fiber system which was operating at 100 MHz with power levels lower by a factor of 3 for the pump (40 mW at 780 nm) and up to 5 for the Stokes (1 mW at 1000 nm).

A fourth important point of my Ph.D. research activity is the demonstration of a novel coherent Raman technique hereafter defined as balanced-detection Raman Induced Kerr Effect Spectroscopy (BD-RIKES), which combines the advantages of SRS microscopy, i.e. the absence of nonresonant background and the linear dependence of the signal on the number of oscillators in the focal volume, with the advantage of CARS, namely the absence of any linear background. Balanced detection inherently offers an effective way to cancel laser intensity noise,

so that high-signal-to-noise ratios are achieved even with low pump modulation frequencies. BD-RIKES images of polystyrene beads, when compared to those acquired in a SRS regime with the same modulation frequencies, result indeed much smoother and with better contrast. A last extremely interesting property of BD-RIKES, is that according to the choice of the waveplates in excitation and detection for the pump and Stokes beams, different components of the nonlinear optical susceptibility tensor of the sample can be selected. This has been experimentally demonstrated by acquiring spectra proportional either to the real or to the imaginary part of the third-order susceptibility of Acetone molecules.

The thesis is structured in five Chapters which summarize the main theoretical and experimental work done during my Ph.D. studies. The Chapter *One* is introductive and prepares the theoretical grounds for rest of the Chapters. In particular this Chapter discusses the main physical aspects of CRS techniques and the derivation of four coupled equations for four-wave mixing process derived from Maxwell's equations.

The Chapter *Two* describes Coherent Anti-stokes Raman Spectroscopy and Stimulated Raman Spectroscopy techniques theoretically in detail. The effect of presence of non-resonant background on CARS signal is discussed and a short description to different non-resonant background suppression techniques commonly applied to CARS, is given. In the end of Chapter, laser sources and their optimal parameters for state-of-the-art CARS and SRS techniques are presented.

In Chapter *Three*, the compact versatile fiber-format Coherent Raman microscopy setup developed in our laboratory is discussed. Then experiments on CARS and SRS spectroscopy/microscopy performed on this setup with their results closed to current state-of-the-art, are presented. Showing added advantage of the third branch, results on the experiment on Interferometric-CARS done with the setup are given.

The Chapter *Four* is totally dedicated to the broadband time-resolved CARS (TR-CARS) experiment on a different type of setup developed in the laboratory. Again this setup is based on a single, but free-space, ytterbium laser. In this Chapter, spectroscopy results from both normal broadband CARS and the

broadband TR-CARS on different solvents are compared.

The Chapter *Five* first presents the Raman Induced Kerr Effect(RIKE) spectroscopy and then introduces our novel technique BD-RIKES with a brief description of its working principle. Experimental results of BD-RIKE spectroscopy/ microscopy performed on the same fiber-format laser setup being used for CARS/SRS, are presented. At the end, microscopy results from BD-RIKE and SRS on beads are compared.

At the end of all Chapters, Appendixes are attached in support of the materials discussed in the Chapters.

Chapter 1

Introduction to Coherent Raman spectroscopy

This introductive Chapter provides the conceptual and theoretical grounds for Coherent Raman Scattering (CRS) techniques. In the first section, a brief introduction of nonlinear spectroscopy techniques and in particular of Coherent Raman techniques for non-invasive spectroscopy/microscopy is presented. The second section includes a description of the spontaneous Raman process through a semiclassical approach. The third section describes Coherent Raman Scattering processes in the light of third-order nonlinear response of the matter. The third-order nonlinear responses are originated from third-order polarization induced in the material by superposition of four electric fields inside the material. The kernel of third-order polarization is the third-order susceptibility of the material. The subsequent part of the section describes the resonant and non-resonant character of third-order susceptibility, depicting its tensorial nature, for the CRS process. In the last Section, the four nonlinear coupled equations for the interaction of four fields involved in CRS process are derived through a semiclassical approach. The evolution of these coupled equations with respect to the space coordinates in the direction of the propagation gives the energy exchange among the fields during CRS process.

1.1 Introduction to nonlinear spectroscopy techniques

Optical spectroscopy/microscopy has been in a pivotal role in investigation of molecular structure and dynamics. Optical microscopy has the unique capability of imaging biological samples with submicron level resolution. Fluorescence microscopy, in particular which has been widely used in material and life sciences, offers sensitivity down to single molecule limit and high chemical specificity, at the price of sample staining with fluorescent marker molecules[20]. Staining can, in fact, perturb the target molecules and/or alter their physiological environment, since the fluorescence levels often have sizes comparable to molecules under study. To overcome this limitation, other noninvasive contrast mechanisms are needed. A representative example is phase contrast and differential interference contrast (DIC) microscopy[21; 22] which takes advantage of minor refractive index changes across the label-free sample to highlight particles and interfaces. But both of them are not chemically selective.

Vibrational contrast mechanisms, such as infrared spectroscopy and Raman scattering spectroscopy/microscopy, both based on characteristic vibrational frequencies of the investigated molecules, allow for level-free, non-invasive chemically selective imaging. Unfortunately infrared absorption microscopy/spectroscopy suffers from poor spatial resolution due to the use of long excitation wavelength (diffraction limit). Additionally due to the fact that IR bands arise from the transitions associated with a change in the dipole moment of the molecule. Such transitions are forbidden in a cento-symmetric molecule, then no modes are infrared active. On the other hand, Raman spectroscopy/microscopy overcomes these limitations due to the fact that Raman bands arises from a change in the molecular polarizability. However the sensitivity of the spontaneous Raman scattering technique is limited by the inherently small cross-section of the process, often with the additional problem of a strong fluorescence background. In Surface enhanced Raman Scattering (SERS)[23; 24] technique, the sensitivity can be boosted up to the single molecule detection limit by making target molecules to be

adsorbed on rough metal surfaces, providing intense field enhancement. Strict requirements for the optimized parameters of these nano-structured metal surfaces restricts the potential of such approach to justfy. Also this kind of preparation is nearly impossible for most biological applications in vivo.

With the advent of laser in 1960, a new era of modern spectroscopy began as these new light sources can provide intense coherent narrowband tunable radiation and hence are able to significantly excite nonlinear modes of the molecules. This initiated a path for a plethora of different nonlinear optical (NLO) microscopy/spectroscopy techniques. The most commonly used and developed since then include Two-photon Excited Fluorescence (TPEF), Second Harmonic Generation (SHG), Third Harmonic Generation (THG), Two Photon Absorption (TPA) microscopy and Coherent Raman Spectroscopy (CRS) techniques. A general characteristic and potential advantage of these techniques is their 'self-sectioning' property. Owing to the nonlinear dependence of the detected signal on the input field(s), the signal is generated only within the small volume around the focal point. This permits imaging of optical slices and subsequent reconstruction of the three dimensional structure of the specimen. TPEF in particular has been used by neuroscientists to image physiological functioning in microscopic and subcellular neural compartments[25]. The TPEF imaging relies either on endogenous fluorophores which are limited and not present in every sample, or exogenous fluorophores (with large absorption cross-section) which may alter the functionality of the system under study. SHG imaging exploits the lack of inversion symmetry in the molecules as contrast mechanism and for this reason its application range is rather limited. THG imaging is especially suited for the three-dimensional imaging of transparent specimens. It is generated near gradients in the refractive index and in general in the presence of a third-order nonlinear susceptibility[26]. This is non-invasive but nonresonant in the nature, therefore provides no chemical selectivity. TPA microscopy provides a contrast mechanism for nonfluorescent chromophores that has appreciable two-photon absorption cross-section[27; 28; 29], TPA spectroscopy is a useful tool to study materials having one-photon forbidden but two-photon allowed excited states.

Coherent Raman Spectroscopies/Microscopies are extremely popular techniques offering high molecular specificity based on coherently enhanced Raman-active vibrational contrast. In the following paragraphs, we will discuss these processes in more detail.

1.2 Spontaneous Raman spectroscopy

The *Raman effect* is an inelastic scattering of incident light photons which involves the generation of new frequencies during the light-matter interaction. It was first discovered by Sir C. V. Raman[30] and independently by Grigory Landsberg and Leonid Mandelstam[31]. When light is incident on matter, the majority of photons are scattered elastically and do not change their frequency. This is known as *Rayleigh Scattering*. However a small fraction of photons are scattered inelastically changing their frequencies. This is known as *Raman scattering*.

Classical theory reveals that for a molecule, the superposition of the applied radiation field ($E_0 \cos(\omega_l t)$) and the molecular vibrations (ω_k) induced by radiation field can generate linearly induced electric dipole $P^{(1)}$ oscillating additionally at side-band frequencies given by [Derivation of equation (1.1) is presented in Appendix (A)]:

$$P^{(1)} = P^{(1)}(\omega_l) + P^{(1)}(\omega_l - \omega_k) + P^{(1)}(\omega_l + \omega_k) \tag{1.1}$$

where

$$P^{(1)}(\omega_l) = \alpha_0 E_0 \cos(\omega_l t) \tag{1.2a}$$

$$P^{(1)}(\omega_l - \omega_k) = {\alpha_k}^{Ram} E_0 \cos[(\omega_l - \omega_k)t + \delta_k] \tag{1.2b}$$

$$P^{(1)}(\omega_l + \omega_k) = {\alpha_k}^{Ram} E_0 \cos[(\omega_l + \omega_k)t + \delta_k] \tag{1.2c}$$

and

$${\alpha_k}^{Ram} = \frac{1}{2}{\alpha_k}' Q_k,$$

where α_0 and ${\alpha_k}'$ are the polarizability tensor component at equilibrium and the derived polarizability tensor component for a particular normal mode of molecular vibration Q_k at equilibrium respectively.

As result of equation (1.1)the linear induced electric dipole has three distinct frequency components :-

- $P^{(1)}(\omega_l)$, which gives rise to radiation at ω_l and accounts for *Rayleigh scattering*
- $P^{(1)}(\omega_l - \omega_k)$, which gives rise to radiation at $\omega_l - \omega_k$ and accounts for *Stokes Raman scattering*
- $P^{(1)}(\omega_l + \omega_k)$, which gives rise to radiation at $\omega_l + \omega_k$ and accounts for *anti-Stokes Raman scattering*

The energy level schemes for the three processes refer to Figure (1.1).

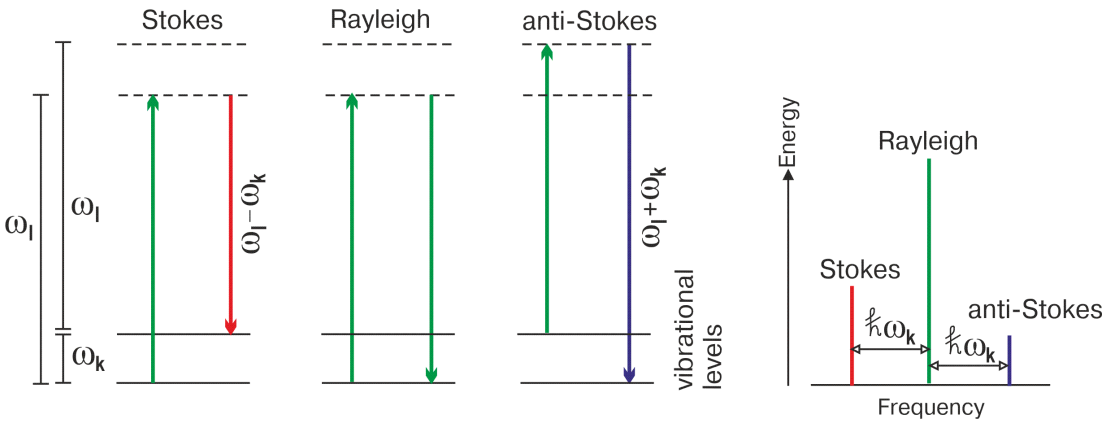


Figure 1.1: Rayleigh scattering, Stokes scattering and anti-Stokes scattering.

Thus, Rayleigh scattering arises from the electric dipole oscillation at the frequency ω_l induced by the external electric field, while the frequencies produced by Raman scattering can be seen as beat frequencies between the radiation frequency ω_l and molecular frequency ω_k. All molecules exhibit Rayleigh scattering, because all the molecules are polarizable to a greater or lesser extent, α_0 will always have some non-zero components. The corresponding necessary condition for Raman scattering associated with a molecular frequency ω_k requires that at least change in one of the tensor components of the derived polarizability tensor α_k with respect to the normal coordinate of the vibration Q_k, must be non-zero at the equilibrium position. It should be noted that induced dipoles $P^{(1)}(\omega_l \pm \omega_k)$

are shifted in phase relative to the incident field by δ_k. The quantity δ_k will be different for different molecules.

Although classical theory discussed above provides qualitative information about Raman scattering, it is unable to provide quantitative information; the magnitude of $\alpha_k{}'$ as well as the vibrational frequencies related to the properties of the scattering molecule. The quantum mechanical theory provides this information and forms the basis for a complete treatment of all aspects of Raman scattering. This treatment reveals Raman scattering as a tool for spectroscopy.

Both Stokes Raman scattering and anti-Stokes Raman scattering are called *Spontaneous Raman scattering*. In Stokes scattering, the population of the ground state is transferred into excited states, whereas in anti-Stokes scattering, the population of excited states (for high temperature samples that have considerable population in the excited vibration states) is transferred to the ground state. The intensity of spontaneous Raman scattering is linearly proportional to the concentration of the sample and reflects the population of the energy states. Because the position of the vibrationally excited states determines the frequency-shift between the incident light and Raman scattering photons, the spectrum of spontaneous Raman contains information about the energy level structures of the sample. This spectroscopic method is called *Raman Spectroscopy*. And the frequency difference between incident and scattered radiation is called *Raman shift*. Raman shift is independent of the frequency of the incident light. It is constant and characteristic of the sample molecule.

Advantages of Spontaneous Raman Spectroscopy

- Raman spectroscopy can be used as a chemical selective tool, not only for gases but also for liquids and solids that exhibit very diffuse absorption band.

- Both polar molecules and non-polar molecules can exhibit Raman effect, which is not the case for absorption spectroscopy since non-polar molecules do not present electric-dipole allowed transitions. Rotational-vibrational changes in non-polar molecule can be exhibited only by Raman spectroscopy.

(For example, spectroscopy of O_2, N_2 molecules).

- Raman spectroscopy involves the measurement of radiation frequencies which differ from incident radiation frequency. The absolute frequency of incident radiation can be chosen arbitrarily, for example, in order to match the transparency window of the sample and/ or to bring the scattered spectra into convenient spectral region for detection generally in the visible region.

- Raman spectroscopy makes use of visible or ultraviolet radiation rather than infrared radiation, hence providing higher spatial resolution.

Disadvantages of Spontaneous Raman Spectroscopy

The main disadvantage of spontaneous Raman spectroscopy is that the Raman signal is weak and incoherent. The cross-section of Raman scattering is only $10^{-31} - 10^{-26}\ cm^2$ per molecule while for fluorescence it is about $10^{-16}\ cm^2$ per molecule. Fluorescence can easily overwhelm the Raman signal. As seen in our previous discussion that the Raman scattering signal from each molecule bears an arbitrary phase relationship with respect to phase of the incident field, since initial phase of the vibrational mode δ_k changes from molecule to molecule. In a real experimental situation, we do not probe a single molecule, instead an assembly of molecules with their random initial phases and random orientations in space (relaxing the assumption of being space-fixed), thus the molecules act as independent sources of radiation irrespective of degree of correlation among their positions. Hence the Raman scattering signal will be an incoherent radiation spread in a 4π steradian solid angle. Practically we can collect only a small fraction of the entire signal, which makes the spontaneous Raman spectroscopy not suitable for microscopic imaging at fast acquisition rates. The weak and incoherent Raman signal can be enhanced by many orders of magnitude in Coherent spectroscopy.

1.3 Coherent Raman Spectroscopy

Incoherency of spontaneous Raman signals is removed by implementing coherent spectroscopy techniques. Coherent techniques are based either on the coherent excitation of the target atoms or molecules or on the superposition of coherently scattered light from the target atoms or molecules[32]. Laser pulses can excite coherently and establish a definite phase relationship among the amplitudes of atomic or molecular wavefunctions of the target atoms or molecules. Such a definite phase relationship in turn determines the total amplitude of the scattered, emitted or absorbed radiation. In addition the spatial coherence of the incident laser pulse also creates a definite spatial distribution of the coherently excited molecules. This ends up with a spatial coherence in the scattered signal leading to a directional signal. Thus coherent property constitutes the major and fundamental difference between Coherent Raman Spectroscopy (CRS) technique and its incoherent counterpart, spontaneous Raman spectroscopy. With proper implementation of the coherent excitation beams and the collecting optics, entire CRS signal can be detected experimentally.

Coherent Raman Spectroscopy (CRS) techniques can be considered as two-step processes. In the first step, a set of multiple laser pulses centered at different optical frequencies, but whose combination matches the vibrational frequency of the target molecules, is incident on the sample and generates a vibrational coherence state in the molecules. These coherent collective induced vibrations in the first step prepare the sample for the second step. Under this criterion the difference between spontaneous Raman and CRS is that in spontaneous Raman, the target molecules are vibrating randomly in phase, while in CRS, after the first step, target molecules are vibrating coherently. In analogy with the spontaneous Raman effect, in the second step of CRS, another laser pulse called *probe pulse*, either at the same frequency of one of the first-step laser pulses or at a different frequency, interacts with the sample and modulates the vibrational coherence generated in the first step. At the output we detect the beat frequency between the vibrational resonance frequency and the probe pulse frequency to identify

the presence of the target molecules. Thus, in CRS, at least two laser photons, called *pump* (ω_p) and *Stokes*(ω_s) respectively, whose frequency difference($\omega_p - \omega_s$) matches a molecular vibration, are needed in the first step, and a third laser photon, either degenerate or not with respect to the former pair, is needed as a probe (ω_{pr}) in the second step. The whole mechanism generates fourth photon ($\omega_p - \omega_s + \omega_{pr} \equiv \omega_{CRS}$). It implies that CRS processes are a kind of four-wave mixing (FWM) process, driven by nonlinear response of the material.

All optical phenomena that arise from light-matter interaction can be described by introducing a proper polarization term P. In the framework of classical electromagnetic theory, the nonlinear response of a medium to an applied electromagnetic field can be given by the following functional form of the total induced polarization[33]:

$$P(r,t) = f[E(r,t), E(r^{'},t)], \tag{1.3}$$

which means the nonlinear response at point (r,t) is not only due to the action of the applied fields at the same point, but also of the fields at a different point $(r^{'},t)$. A typical approximation is to express the total polarization as a power series with respect to the fields,

$$P(r,t) = P^{(1)}(r,t) + P^{(2)}(r,t) + P^{(3)}(r,t) + ... \tag{1.4}$$

where $P^{(i)}$ is the i^{th} order polarization,and

$$P^{(1)}(r,t) = \epsilon_0 \int_{-\infty}^{+\infty} \chi^{(1)}(r-r',t-t') : E(r,t')dr'dt' \tag{1.5}$$

$$\begin{aligned} P^{(2)}(r,t) = \int_{-\infty}^{+\infty} & \chi^{(2)}(r-r',t-t';r-r'',t-t'') \\ & : E(r',t')E(r'',t'')dr'dr''dt'dt'' \end{aligned} \tag{1.6}$$

$$\begin{aligned} P^{(3)}(r,t) = \int_{-\infty}^{+\infty} & \chi^{(3)}(r-r',t-t';r-r'',t-t'';r-r''',t-t''') \\ & : E(r,t')E(r'',t'')E(r''',t''')dr'dr''dr'''dt'dt''dt''' \end{aligned} \tag{1.7}$$

and so on.

In the above equations the double dot (:) indicates a tensorial product between $\chi^{(i)}$ and the electric fields E, where E is a first-rank tensor, and $\chi^{(i)}$ is a $(i+1)^{th}$-rank tensor. $\chi^{(1)}, \chi^{(2)}, \chi^{(3)}$ are respectively called linear dielectric susceptibility,

second order dielectric susceptibility, third-order dielectric susceptibility of the bulk material. They contain characteristic response of the bulk material when interacting with an electromagnetic field.

The total polarization P in equation (1.4)can be classified as following:

$$P = P_L + P_{NL}, \tag{1.8}$$

where P_L is *linear* contribution containing the first term $P^{(1)}(r,t)$, linear in electric field, and P_{NL} is *nonlinear* contribution containing the rest higher order terms in electric field.

Fourier transformation of equations (1.5),(1.6), (1.7) gives,

$$P^{(1)}(k,\omega) = \epsilon_0 \chi^{(1)}(k,\omega) : E(k,\omega) \tag{1.9a}$$

$$P^{(2)}(k,\omega) = \chi^{(2)}(k,k',k'',\omega,\omega',\omega'') : E(k',\omega')E(k'',\omega'') \tag{1.9b}$$

$$P^{(3)}(k,\omega) = \chi^{(3)}(k,k',k'',k''',\omega,\omega',\omega'',\omega''') : E(k',\omega')E(k'',\omega'')E(k''',\omega''') \tag{1.9c}$$

where k, k', k'', k''' are spatial frequencies and $\omega, \omega', \omega'', \omega'''$ are the angular frequencies.

If the i^{th}-order susceptibility $\chi^{(i)}(r,t)$ is independent of r, its Fourier transform $\chi^{(i)}(k,\omega)$ is independent of k. In this case, the response is called *local*. For simplicity hereafter we will assume valid this assumption, thus obtaining:

$$P^{(1)}(k,\omega) = \epsilon_0 \chi^{(1)}(\omega) : E(k,\omega) \tag{1.10a}$$

$$P^{(2)}(k,\omega) = \chi^{(2)}(\omega,\omega',\omega'') : E(k',\omega')E(k'',\omega'') \tag{1.10b}$$

$$P^{(3)}(k,\omega) = \chi^{(3)}(\omega,\omega',\omega'',\omega''') : E(k',\omega')E(k'',\omega'')E(k''',\omega''') \tag{1.10c}$$

If the response of the medium is *instantaneous*, the expressions for $P^{(2)}$ and $P^{(3)}$ become simple tensorial product of electric fields *. But this is not the case of Coherent Raman processes. The Coherent Raman response of a medium, since mediated by the vibrational motion, is inherently not instantaneous.

*That is

$$P^{(2)}(t) = \chi^{(2)} : E(t)E(t)$$
$$P^{(3)}(t) = \chi^{(3)} : E(t)E(t)E(t)$$

Since CRS is related to a non-instantaneous response of the material and to an interaction of four-fields at different optical frequencies ω', ω'', ω''' and ω, CRS processes can all be described within the formalism of equation(1.10c).

For simplicity we will replace the symbols of these four fields as following :

$$\begin{aligned} \omega' \equiv \omega_1 \quad \omega'' \equiv \omega_2 \\ \omega''' \equiv \omega_3 \quad \omega \equiv \omega_4 \end{aligned} \tag{1.11}$$

Equation(1.10c) takes the form:

$$P^{(3)}(k_4, \omega_4) = \chi^{(3)}(\omega_4; \omega_1, \omega_2, \omega_3) : E(k_1, \omega_1)E(k_2, \omega_2)E(k_3, \omega_3) \tag{1.12}$$

which corresponds in the time space, after inverse Fourier transform, as:

$$\begin{aligned} P^{(3)}(r_4, t_4) = \int_{-\infty}^{+\infty} \chi^{(3)}(t_4 - t_1, t_4 - t_2, t_4 - t_3) \\ : E(r_1, t_1)E(r_2, t_2)E(r_3, t_3)dr_1dr_2dr_3dt_1dt_2dt_3 \end{aligned} \tag{1.13}$$

Now, we will discuss the properties of $\chi^{(3)}(\omega_4; \omega_1, \omega_2, \omega_3)$ (or $\chi^{(3)}(t_4 - t_1, t_4 - t_2, t_4 - t_3)$) because it is the kernel of third-order polarization induced in the material and it contains Coherent Raman response which is of interest for our discussion.

All CRS processes in general involve virtual levels[†] except real vibrational levels we want to probe. For example in Figure (1.2) which is the representative energy-level diagram for the CRS processes, $< m|$ and $< q|$ are virtual states while we want to probe transition between real vibrational levels $< k|$ and $< n|$.

[†]a short-lived intermediate quantum state that mediates otherwise forbidden transitions in a multistep process

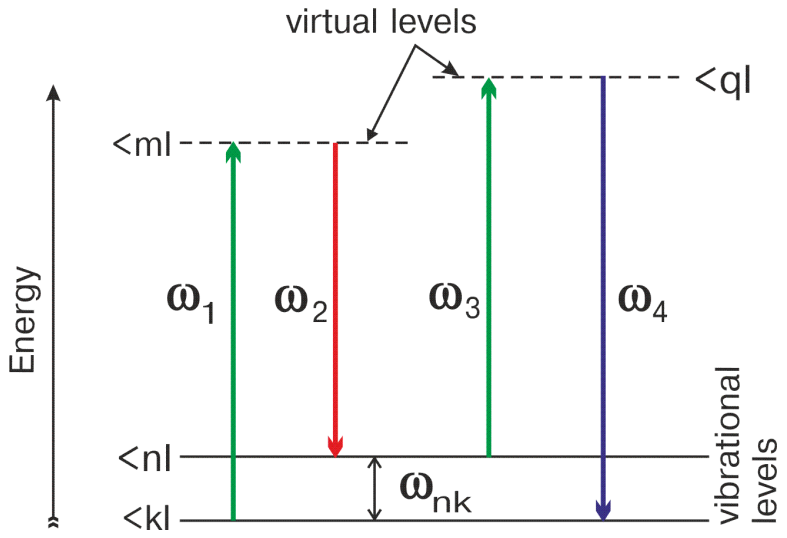


Figure 1.2: Representative energy level diagram for CRS processes.

The process involves four photons, one each at frequencies ω_1 and ω_3 respectively are destroyed and one each at frequencies ω_2 and ω_4 respectively are created. We will follow the convention that the frequencies that are destroyed in the process are written with positive signs while the created frequencies with negative signs. If we adopt from Shen and Byod books, the sequential labeling method for frequencies for distinctive representation of $\chi^{(3)}$, then going from left to right in the figure and following energy conservation law, represent the third-order susceptibility for the process as $\chi^{(3)}(-\omega_4;\omega_1,-\omega_2,\omega_3)$.

Mathematical expression for $\chi^{(3)}(-\omega_4;\omega_1,-\omega_2,\omega_3)$ for FWM process in Figure (1.2) is written as[34]:

$$\chi^{(3)}(-\omega_4;\omega_1,-\omega_2,\omega_3) = \frac{N}{\hbar}\mathbf{P}_F \sum_{m,n,q} \frac{\mu_{km}\mu_{mn}\mu_{nq}\mu_{qk}}{(\omega_{mk}-\omega_1-i\gamma_{mk})}\cdot \frac{1}{(\omega_{nk}-\omega_1+\omega_2-i\gamma_{nk})}\cdot\frac{1}{(\omega_{qk}-\omega_4-i\gamma_{qk}))}, \tag{1.14}$$

where $\mathbf{P}_F$ is the full permutation operator; $\mu_{km},\mu_{mn},\mu_{nq},\mu_{qk}$ are transition dipole moments; $\omega_{mk},\omega_{nk},\omega_{qk}$ are the energy differences between associated energy levels; N is density of molecules(number of molecules per unit volume) and $\gamma_{mk},\gamma_{nk},\gamma_{qk}$ are the homogeneous linewidth [half-width at half maximum (HWHM)] of the associated electronic or vibrational transition. A more comprehensive expression of $\chi^{(3)}$ can be found elsewhere ([35]).

Thus, for our representative example, in equation (1.14), on right hand side in the denominator, inside the first and third factors, the terms $(\omega_{mk}-\omega_1)$ and $(\omega_{qk}-\omega_4)$ will be identically zero due to fact that virtual levels are possible everywhere and they are always in resonance with all the incident frequency combination. This means that in the denominator the first and third factors will remain pure imaginary and their product gives a real term. With this consideration, equation (1.14) for $\chi^{(3)}$ for CRS will be rearranged as follows:

$$\chi^{(3)}(-\omega_4;\omega_1,-\omega_2,\omega_3) = \frac{N}{\hbar}\mathbf{P}_F \sum_{m,n,q} \frac{\Delta}{(\omega_{nk}-\omega_1+\omega_2-i\gamma_{nk})}, \tag{1.15}$$

where Δ is a real quantity *proportional to spontaneous Raman differential cross-section.*

The complex $\chi^{(3)}$ term given by equation (1.15) is typically written as:

$$\chi^{(3)}(-\omega_4;\omega_1,-\omega_2,\omega_3) = \mp(\chi^{(3)R}_{Re} + i\chi^{(3)R}_{Im} + \chi^{(3)NR}_{Re}), \tag{1.16}$$

where

$$\Rightarrow \qquad \chi^{(3)R}_{Re} = \frac{N}{\hbar}\mathbf{P}_F \sum_{m,n,q} \Delta \frac{(\omega_{nk}-(\omega_1-\omega_2))}{(\omega_{nk}-(\omega_1-\omega_2))^2+(\gamma_{nk})^2} \tag{1.17a}$$

$$\Rightarrow \qquad \chi^{(3)R}_{Im} = \frac{N}{\hbar}\mathbf{P}_F \sum_{m,n,q} \Delta \frac{\gamma_{nk}}{(\omega_{nk}-(\omega_1-\omega_2))^2+(\gamma_{nk})^2} \tag{1.17b}$$

$$\Rightarrow \qquad \chi^{(3)NR}_{Re} = constt. \tag{1.17c}$$

In equations (1.16) and (1.17), the superscript "R" represents *resonance* that means these parts of $\chi^{(3)}$ are coming from incident frequency combinations which are in *resonance* with vibrational frequency of the investigated molecules. The resonant contribution $\chi^{(3)R}$ has real and imaginary components: $\chi^{(3)R}_{Re}$ and $\chi^{(3)R}_{Im}$. Far from any electronic resonances, the imaginary component $\chi^{(3)R}_{Im}$ is the resonance Raman response and it involves nuclear contribution from the molecules. It has a typical Lorentzian line shape of spontaneous Raman spectra (centered at resonant frequency of the molecule). Its spectrum is shown by red line in Figure(1.3). On the other hand, the real component $\chi^{(3)R}_{Re}$ involves the electronic contribution from the investigated molecules. It has a dispersive shape [Shape is shown by green line in Figure(1.3)].

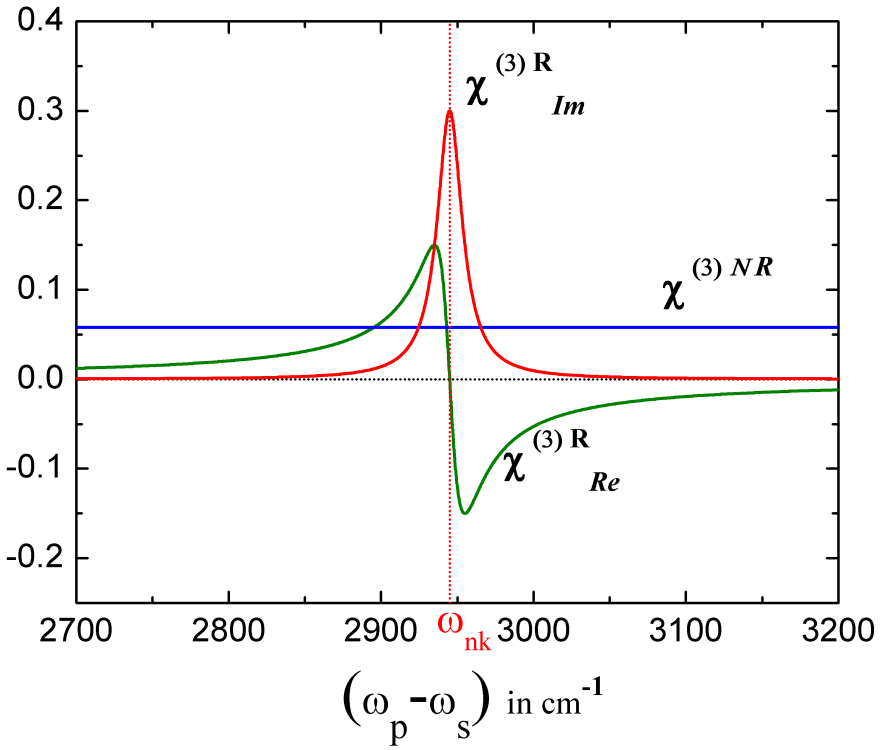


Figure 1.3: Spectral shape of different components of $\chi^{(3)}$.

It may be stated that $\chi_{Re}^{(3)R}$ *is related to nonlinear refractive index and* $\chi_{Im}^{(3)R}$ *is associated with the spontaneous Raman transition* ([36; 37]). All the Coherent Raman Spectroscopic techniques share the common property that frequency difference $(\omega_1 - \omega_2)$ is tuned to match a vibrational Raman mode ω_{nk} of the molecule and when this happens, material coherently responses through $\chi^{(3)R}$ and then this intrinsic labeling of the molecule is identified by probing the generated frequency ω_4.

Figure (1.4) demonstrates the energy-level diagrams of mechanisms which contribute to resonant and non-resonant parts of $\chi^{(3)}$. Panel(a) shows resonant Raman contribution from the investigated molecule when $\omega_1 - \omega_2$ is in resonance with its molecular vibration ω_{nk}. Panel(b) shows that there exists another FWM mechanism which utilizes the same input frequency components but their different combination, and can generate photons at frequency ω_4. Since this combination of input frequencies is not in resonance with the investigated molecule's vibrational frequency ω_{nk}, it contributes to non-resonant(NR) part $\chi^{(3)NR}$. In real practical environment, other molecules may also present in the sample, for

example, substrate molecules or solvent molecules. Panel(c) shows this situation. The same input frequencies combination, which is in resonance with the vibrational frequency of investigated molecule, but is not in resonance with vibrational frequency ω_{pk} of other background molecules. These molecules can generate light at frequency ω_4 by this mechanism and add a non-resonant(NR) contribution $\chi^{(3)NR}$. Hence in equation (1.16),$\chi^{(3)NR}_{Re}$ represents combined non-resonant contribution from both investigated molecules and the background molecules. Since all the non-resonant contribution $\chi^{(3)NR}_{Re}$ originates from the electronic response of the molecules and does not probe any vibrational resonance, it is instantaneous. And that is why $\chi^{(3)NR}_{Re}$ is real and constant over near about frequency range [Blue line in Figure(1.3)].

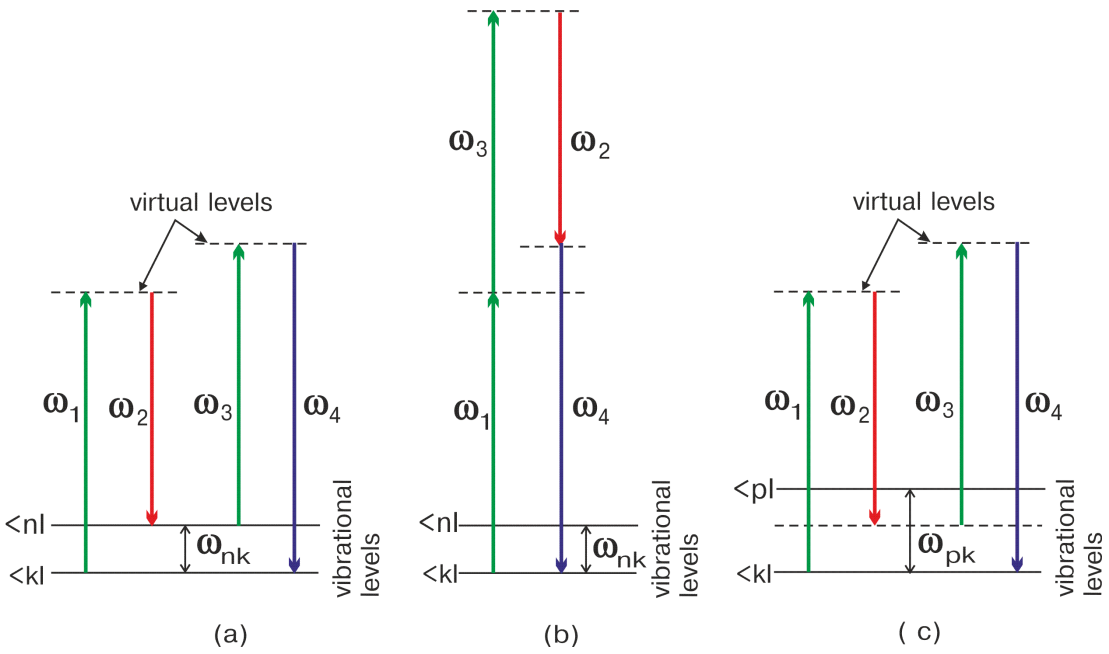


Figure 1.4: Energy-level diagram for a CRS process, demonstration of the mechanisms for:(a)Resonant Raman contribution and (b)non-resonant contribution from investigated molecule when $\omega_1 - \omega_2$ is in resonance with the molecular vibration ω_{nk} and (c)non-resonant contribution from other molecule present in the sample when $\omega_1 - \omega_2$ is not in vibrational resonance with its molecular vibration ω_{pk}.

From equation (1.12),it can be seen that total incident field comprises of three frequency components $E(\omega_1)$, $E(\omega_2)$ and $E(\omega_3)$. There are several possible combinations of the frequency components that induce same component of nonlinear polarization $P^{(3)}(\omega_4)$. For example, for the representative CRS pro-

cess in Figure(1.2), frequency component $\omega_4 = \omega_1 - \omega_2 + \omega_3$ to induce $P^{(3)}(\omega_4)$, can arise from 6 possible combinations: $E(\omega_1)E^*(\omega_2)E(\omega_3)$, $E(\omega_1)E(\omega_3)E^*(\omega_2)$, $E^*(\omega_2)E(\omega_1)E(\omega_3)$, $E^*(\omega_2)E(\omega_3)E(\omega_1)$, $E(\omega_3)E^*(\omega_2)E(\omega_1)$ and $E(\omega_3)E(\omega_1)E^*(\omega_2)$; and corresponding nonlinear susceptibilities will be

$$\chi^{(3)}(-\omega_4;\omega_1,-\omega_2,\omega_3),\chi^{(3)}(-\omega_4;\omega_1,\omega_3,-\omega_2),\quad \chi^{(3)}(-\omega_4;-\omega_2,\omega_1,\omega_3),$$
$$\chi^{(3)}(-\omega_4;-\omega_2,\omega_3,\omega_1),\chi^{(3)}(-\omega_4;\omega_3,\omega_1,-\omega_2),\quad \chi^{(3)}(-\omega_4;\omega_3,-\omega_2,\omega_1)$$

respectively. Here we have adopt the convention that electric field with negative value of frequency is replaced by its complex conjugate with positive value of frequency. This justifies the presence of permutation operator $\mathbf{P}_F$ in equation(1.14). For our representative CRS process $\mathbf{P}_F = 6$.

In mathematical term, $\chi^{(3)}$ is a fourth-rank tensor, encompassing $3^4 = 81$ elements, as obtained by permutation of the (i,j,k,l) indices over the three Cartesian coordinates $1,2,3$ corresponding to X-, Y-, and Z-axes respectively. In an isotropic medium with inversion symmetry, the 81 elements reduces to four independent components, since the following equations take place :

$$\chi^{(3)}_{1111} = \chi^{(3)}_{2222} = \chi^{(3)}_{3333} = \chi^{(3)}_{1122} + \chi^{(3)}_{1212} + \chi^{(3)}_{1221}, \tag{1.18a}$$
$$\chi^{(3)}_{1122} = \chi^{(3)}_{1133} = \chi^{(3)}_{2211} = \chi^{(3)}_{2233} = \chi^{(3)}_{3311} = \chi^{(3)}_{3322}, \tag{1.18b}$$
$$\chi^{(3)}_{1212} = \chi^{(3)}_{1313} = \chi^{(3)}_{2121} = \chi^{(3)}_{2323} = \chi^{(3)}_{3232} = \chi^{(3)}_{3131}, \tag{1.18c}$$
$$\chi^{(3)}_{1221} = \chi^{(3)}_{1331} = \chi^{(3)}_{2112} = \chi^{(3)}_{2312} = \chi^{(3)}_{3113} = \chi^{(3)}_{3223} \tag{1.18d}$$

For CRS processes, the convention, for generic $\chi^{(3)}_{ijkl}$, is to assign indices i, j, k, l to ω_4, ω_1, ω_2, ω_3 respectively to represent their electric field's polarization states. In such componentwise representation of $\chi^{(3)}$, the induced polarization at frequency ω_4 for the representative CRS process is written as:

$$P^{(3)}_i(-\omega_4;\omega_1,-\omega_2,\omega_3) \propto \mathbf{P}_F . \sum_{jkl} \chi^{(3)}_{ijkl}(-\omega_4;\omega_1,-\omega_2,\omega_3) E_j(\omega_1) E^*_k(\omega_2) E_l(\omega_3) \tag{1.19}$$

This induced polarization is the source for the Raman response of the medium in a CRS process.

1.4 Nonlinear coupled equations for CRS processes

In this section, we will derive the equations that describe the evolution of an electric field in the presence of nonlinear polarization produced in the material. Let us consider an electric field at frequency ω_0 in the presence of a nonlinear polarization term at the same frequency ω_0.

Applying the hypothesis of monochromatic plane wave approach and a generally valid slowly varying envelop approximation (SVEA), a single laser pulse centered at frequency ω_0 is written, in cartesian coordinates, as:

$$E(r,t) = \frac{1}{2}\left[A(r,t)e^{i(\omega_0 t - \vec{k}.\vec{r}+\phi)} + C.C.\right], \tag{1.20}$$

where $A(r,t)$ is the slowly varying envelope of the pulse with respect to a fast (temporally and spatially) oscillating carrier $e^{i(\omega_0 t - \vec{k}.\vec{r}+\phi)}$; ϕ is the absolute phase between envelope and carrier; C.C. represents the complex conjugate of the term.

In CRS although the four interacting fields in general propagate in four different directions, one can define a reference direction $+Z$-axis to describe their interaction and propagation. Equation (1.20) takes the form:

$$E(r,t) = \frac{1}{2}\left[A(r,t)e^{i(\omega_0 t - k_0 z)} + C.C.\right], \tag{1.21}$$

where k_0 is the z-component of k and an initial phase $\phi = 0$ is assumed.

Under the same arguments, the corresponding induced polarization is given by:

$$P_{NL}(r,t) = \frac{1}{2}\left[p_{NL}(r,t)e^{i(\omega_0 t - k_p z)} + C.C.\right] \tag{1.22}$$

where p_{NL} is the envelope and k_p is the wave vector of the carrier.

Generally $k_0 \neq k_p$ and the quantity $\Delta k = k_p - k_0$ is called *wave vector mismatch* for this component wave.

The Fourier transforms[‡] of equations (1.21) and (1.22) are given by following equations:

$$\tilde{E}(r,\omega) = \frac{1}{2}\left[\tilde{A}(r,\omega-\omega_0)e^{-ik_0 z} + C.C.\right] \tag{1.23}$$

[‡]

$$\mathcal{F}\left[e^{\left[i\pi(ax+by)\right]}\right] = \delta(f_x - \frac{a}{2}, f_y - \frac{b}{2})$$

$$\tilde{P}_{NL}(r,\omega) = \frac{1}{2}\Big[\tilde{p}_{NL}(r,\omega-\omega_0)e^{-ik_p z} + C.C.\Big] \tag{1.24}$$

Using a semi-classical approach, starting from Maxwell's equations and referring to a non-magnetic charge-free and current-free medium, under the plane wave hypothesis, the following equation can be readily obtained:

$$\nabla^2 E(r,t) - \frac{1}{c^2}\frac{\partial^2 E(r,t)}{\partial t^2} = \mu_0 \frac{\partial^2 P(r,t)}{\partial t^2} \tag{1.25}$$

$$\Rightarrow \nabla^2 E(r,t) - \frac{1}{c^2}\frac{\partial^2 E(r,t)}{\partial t^2} = \mu_0 \frac{\partial^2 \big[P_L(r,t) + P_{NL}(r,t)\big]}{\partial t^2} \tag{1.26}$$

Without any loss of generality we can ignore $\nabla_\perp^2 E$.

Derivation of equations (1.21) and (1.22)leads to the following terms,

$$\begin{aligned}\frac{\partial^2 E(r,t)}{\partial z^2} \equiv{}& \frac{\partial^2 A(r,t)}{\partial z^2}e^{i(\omega_0 t - k_0 z)} - 2ik_0\frac{\partial A(r,t)}{\partial z}e^{i(\omega_0 t - k_0 z)} \\ &- k_0^2 A(r,t)e^{i(\omega_0 t - k_0 z)} + C.C.\end{aligned} \tag{1.27a}$$

$$\begin{aligned}\frac{\partial^2 E(r,t)}{\partial t^2} \equiv{}& \frac{\partial^2 A(r,t)}{\partial t^2}e^{i(\omega_0 t - k_0 z)} + 2i\omega_0\frac{\partial A(r,t)}{\partial t}e^{i(\omega_0 t - k_0 z)} \\ &- \omega_0^2 A(r,t)e^{i(\omega_0 t - k_0 z)} + C.C.\end{aligned} \tag{1.27b}$$

$$\begin{aligned}\frac{\partial^2 P(r,t)}{\partial t^2} \equiv{}& \frac{\partial^2 p(r,t)}{\partial t^2}e^{i(\omega_0 t - k_p z)} + 2i\omega_0\frac{\partial p(r,t)}{\partial t}e^{i(\omega_0 t - k_p z)} \\ &- \omega_0^2 p(r,t)e^{i(\omega_0 t - k_p z)} + C.C.\end{aligned} \tag{1.27c}$$

Equation (1.26) takes the form,

$$\frac{\partial^2 E(r,t)}{\partial z^2} - \frac{1}{c^2}\frac{\partial^2 E(r,t)}{\partial t^2} = \mu_0 \frac{\partial^2 \big[P_L(r,t) + P_{NL}(r,t)\big]}{\partial t^2} \tag{1.28}$$

Since the amplitude of the nonlinear polarization $p_{NL}(r,t)$ is very small compared to frequency ω_0, we can neglect any fluctuation of it in time, therefore[§],

$$\frac{\partial^2 E(r,t)}{\partial z^2} - \frac{1}{c^2}\frac{\partial^2 E(r,t)}{\partial t^2} = \mu_0 \frac{\partial^2 \big[P_L(r,t)\big]}{\partial t^2} - \mu_0\omega_0^2 p(r,t)e^{i(\omega_0 t - k_p z)} \tag{1.29}$$

Applying Fourier transform to equation (1.29), we have:

$$\frac{\partial^2 \tilde{E}(z,\omega)}{\partial z^2} + \frac{\omega^2}{c^2}\tilde{E}(z,\omega) = -\mu_0\omega^2\tilde{P}_L(z,\omega) - \mu_0\omega_0^2\tilde{p}_{NL}(z,\omega-\omega_0)e^{-ik_p z} \tag{1.30}$$

Calculating the derivative from equation (1.23),

$$\frac{\partial^2 \tilde{E}(z,\omega))}{\partial z^2} = \big[\frac{\partial^2 \tilde{A}(z,\omega-\omega_0)}{\partial z^2} - 2ik_0\frac{\partial \tilde{A}(z,\omega-\omega_0)}{\partial z} - k_0^2\tilde{A}(z,\omega-\omega_0)\big]e^{-ik_0 z} \tag{1.31}$$

[§]Just for convenience, from here now we will ignore writing "C.C." in the equation

Introducing equation (1.31) into equation (1.30), we get:

$$\begin{aligned}\Big[\frac{\partial^2\tilde{A}(z,\omega-\omega_0)}{\partial z^2}-2ik_0\frac{\partial\tilde{A}(z,\omega-\omega_0)}{\partial z}-k_0^2\tilde{A}(z,\omega-\omega_0)\Big]e^{-ik_0z}\\ +\frac{\omega^2}{c^2}\tilde{E}(z,\omega)=-\mu_0\omega^2\tilde{P}_L(z,\omega)-\mu_0\omega_0^2\tilde{p}_{NL}(z,\omega-\omega_0)e^{-ik_pz}\end{aligned} \tag{1.32}$$

Slowly varying envelope approximation (SVEA) translates into the following inequality:

$$\left|\frac{\partial^2\tilde{A}(z,\omega-\omega_0)}{\partial z^2}\right| \lll \left|k_0\frac{\partial\tilde{A}(z,\omega-\omega_0)}{\partial z}\right|$$

Hence, in equation (1.32), the first term can be neglected.

Since $\tilde{P}_L(z,\omega)=\epsilon_0\chi^{(1)}\tilde{E}(z,\omega)$ and $\chi^{(1)}+1=n^2(\omega)$, where $n(\omega)$ is the linear refractive index of the material for frequency ω, equation (1.32) becomes:

$$\begin{aligned}\big[-2ik_0\frac{\partial\tilde{A}(z,\omega-\omega_0)}{\partial z}-k_0^2\tilde{A}(z,\omega-\omega_0)\big]e^{-ik_0z}+\big[\frac{\omega^2}{c^2}\tilde{A}(z,\omega-\omega_0)\\ +\mu_0\omega^2\epsilon_0\chi^{(1)}\tilde{A}(z,\omega-\omega_0)\big]e^{-ik_0z}=-\mu_0\omega_0^2\tilde{p}_{NL}(z,\omega-\omega_0)e^{-ik_pz}\end{aligned} \tag{1.33}$$

Using $\mu_0\epsilon_0=\frac{1}{c^2}$,

$$\begin{aligned}\big[2ik_0\frac{\partial\tilde{A}(z,\omega-\omega_0)}{\partial z}-\big[k^2(\omega)-k_0^2\big]\tilde{A}(z,\omega-\omega_0)\big]e^{-ik_0z}\\ =\mu_0\omega_0^2\tilde{p}_{NL}(z,\omega-\omega_0)e^{-ik_pz}\end{aligned} \tag{1.34}$$

$$\Rightarrow 2ik_0\frac{\partial\tilde{A}(z,\omega-\omega_0)}{\partial z}-\big[k^2(\omega)-k_0^2\big]\tilde{A}(z,\omega-\omega_0)=\mu_0\omega_0^2\tilde{p}_{NL}(z,\omega-\omega_0)e^{-i\Delta kz}, \tag{1.35}$$

where $k(\omega)=\frac{\omega n(\omega)}{c}$ is the generic wave vector at angular frequency ω; $\Delta k=k_p-k_0$ is the wave vector mismatch between the polarization wave and the electromagnetic wave.

For $k(\omega)$ close to k_0 (as in the case within a single pulse spectrum), following approximation is plausible:

$$k^2(\omega)-k_0^2=\big[k(\omega)+k_0\big]\big[k(\omega)-k_0\big]\approx 2k_0\big[k(\omega)-k_0\big], \tag{1.36}$$

$k(\omega)$ can be expanded in Taylor series as:

$$k(\omega)=k_0+\frac{\partial k}{\partial\omega}\bigg|_{\omega_0}(\omega-\omega_0)+\frac{1}{2}.\frac{\partial^2k}{\partial\omega^2}\bigg|_{\omega_0}(\omega-\omega_0)^2+\cdots \tag{1.37}$$

$$=k_0+\frac{1}{v_g}\bigg|_{\omega_0}(\omega-\omega_0)+\frac{1}{2}.GVD\bigg|_{\omega_0}(\omega-\omega_0)^2+\cdots \tag{1.38}$$

where by definitions $v_g \equiv \frac{\partial k}{\partial \omega}$ and $GVD \equiv \frac{\partial^2 k}{\partial \omega^2}$.

Introducing above result in equation (1.36) and neglecting the higher order terms in $(\omega - \omega_0)$, we have:

$$k^2(\omega) - k_0^2 = 2k_0\Big[\frac{1}{v_g}\Big|_{\omega_0}(\omega - \omega_0) + \frac{1}{2}.GVD\Big|_{\omega_0}(\omega - \omega_0)^2\Big] \tag{1.39}$$

Now with help of equation (1.39), equation (1.35) becomes:

$$\begin{aligned} 2ik_0\frac{\partial \tilde{A}(z, \omega - \omega_0)}{\partial z} - 2k_0\Big[\frac{1}{v_g}\Big|_{\omega_0}(\omega - \omega_0) + \frac{1}{2}.GVD\Big|_{\omega_0}(\omega - \omega_0)^2\Big] \\ \tilde{A}(z, \omega - \omega_0) = \mu_0\omega_0^2\tilde{p}_{NL}(z, \omega - \omega_0)e^{-i\Delta kz} \end{aligned} \tag{1.40}$$

Applying inverse Fourier transform to above equation to come back to time domain, we arrive at:

$$2ik_0\frac{\partial A(r,t)}{\partial z} + 2i\frac{k_0}{v_g}\frac{\partial A(r,t)}{\partial t} + k_0.GVD\frac{\partial^2 A(r,t)}{\partial t}^2 = \mu_0\omega_0^2 p_{NL}(r,t)e^{-i\Delta kz}$$

$$\Rightarrow \frac{\partial A(r,t)}{\partial z} + \frac{1}{v_g}.\frac{\partial A(r,t)}{\partial t} - \frac{i}{2}.GVD\frac{\partial^2 A(r,t)}{\partial t}^2 = -i\frac{\mu_0\omega_0 c}{2n_{\omega_0}}[p_{NL}(r,t)]e^{-i\Delta kz} \tag{1.41}$$

The second and third terms in the left hand side of the above equation express the linear effect of propagation and of the material dispersion respectively. If $GVD \neq 0$, the pulse during the propagation will broaden in time. Here we will assume that our material is GVD-free (which is practically reasonable in CRS, since the input pulses have picosecond duration and thus pulse broadening due to GVD is negligible). In this case third term will be neglected.

Choosing a frame of reference moving with the pulse at the group velocity v_g (the so-called *retarded frame*) by making the transformations $z' \equiv z$ and $t' \equiv t - \frac{z}{v_g}$, equation (1.41) becomes:

$$\frac{\partial A(r,t)}{\partial z}e^{i\omega_0 t} = -i\frac{\mu_0\omega_0 c}{2n(\omega_0)}[p_{NL}(r,t)]e^{i\omega_0 t}e^{-i\Delta kz} \tag{1.42}$$

$$\Rightarrow \frac{\partial A(r,t)}{\partial z} = -i\frac{\mu_0\omega_0 c}{2n(\omega_0)}[p_{NL}(r,t)]e^{-i\Delta kz} \tag{1.43}$$

The right hand side of the above equation takes into account the effect of the nonlinear response of the material.

To simplify the mathematics for our calculations, let us assume a centrosymmetric material (that means $\chi^{(2)} = 0$) and neglect the terms higher than third

order(usually they are very smaller) in p_{NL}; for a particular combination of frequencies we have,

$$P_{NL}(r,t) \equiv P_i^{(3)}(-(\omega_4;\pm\omega_1,\pm\omega_2,\pm\omega_3)) \propto \chi_{ijkl}^{(3)}(-\omega_4;\pm\omega_1,\pm\omega_2,\pm\omega_3) \\ E(r,t)E(r,t)E(r,t), \tag{1.44}$$

where $\pm$ means that, at a time, either + or - sign is considered; at least one frequency is with + sign (otherwise all frequencies will be created without any input which is physically impossible); and $E(r,t)$ is the superposition of the four interacting fields, given as:

$$\begin{aligned} E(r,t) &= E_{\omega_1}(r,t) + E_{\omega_2}(r,t) + E_{\omega_3}(r,t) + E_{\omega_4}(r,t) \\ \Rightarrow E(r,t) &= \frac{1}{2}\Big[A_1(r,t)e^{i(\omega_1 t - k_1 z)} + A_2(r,t)e^{i(\omega_2 t - k_2 z)} + \\ &\quad A_3(r,t)e^{i(\omega_3 t - k_3 z)} + A_4(r,t)e^{i(\omega_4 t - k_4 z)} + C.C.\Big] \end{aligned} \tag{1.45}$$

When equation (1.45) is introduced into equation (1.44), a vast number of terms arises from the cube of the electric field. These terms can be sorted to form several groups, each one being responsible for a peculiar third-order effect (If one includes the case of degeneracy among the frequencies, the terms responsible for the effects; third-harmonic generation(THG), sum frequency generation(SFG),coherent anti-Stokes Raman scattering(CARS), stimulated Raman scattering(SRS), Raman induced Kerr effect(RIKE) etc, can be obtained). For the CRS processes, which are of our interest in these terms, the four fields are related to each-other by energy-conservation law $\omega_4 = \omega_1 - \omega_2 + \omega_3$. The relevant nonlinear polarization terms that drive four fields in a CRS process can be shown to be equal to:

$$P_{NL}^{(\omega_1)}(r,t) = P_F.\chi^{(3)}\frac{A_2(r,t)A_3^*(r,t)A_4(r,t)}{8}e^{i\left[(\omega_2-\omega_3+\omega_4)t-(k_2-k_3+k_4)z\right]} \tag{1.46a}$$

$$P_{NL}^{(\omega_2)}(r,t) = P_F.\chi^{(3)}\frac{A_1(r,t)A_3(r,t)A_4^*(r,t)}{8}e^{i\left[(\omega_1+\omega_3-\omega_4)t-(k_1+k_3-k_4)z\right]} \tag{1.46b}$$

$$P_{NL}^{(\omega_3)}(r,t) = P_F.\chi^{(3)}\frac{A_1^*(r,t)A_2(r,t)A_4(r,t)}{8}e^{i\left[(-\omega_1+\omega_2+\omega_4)t-(-k_1+k_2+k_4)z\right]} \tag{1.46c}$$

$$P_{NL}^{(\omega_4)}(r,t) = P_F.\chi^{(3)}\frac{A_1(r,t)A_2^*(r,t)A_3(r,t)}{8}e^{i\left[(\omega_1-\omega_2+\omega_3)t-(k_1-k_2+k_3)z\right]} \tag{1.46d}$$

where $P_F = 6$ is the number of permutations for frequencies on right hand side of the equation pertinent to left hand side induced polarization frequency component.

Each equation (1.46) is in the form of equation (1.22). Substituting each equation (1.46) one by one into equation (1.43), we get following four coupled equations:

$$\frac{\partial A_1(r,t)}{\partial z} = -i\alpha_1\chi^{(3)}A_2(r,t)A_3^*(r,t)A_4(r,t)e^{-i\Delta kz} \tag{1.47a}$$

$$\frac{\partial A_2(r,t)}{\partial z} = -i\alpha_2\chi^{(3)}A_1(r,t)A_3(r,t)A_4^*(r,t)e^{i\Delta kz} \tag{1.47b}$$

$$\frac{\partial A_3(r,t)}{\partial z} = -i\alpha_3\chi^{(3)}A_1^*(r,t)A_2(r,t)A_4(r,t)e^{-i\Delta kz} \tag{1.47c}$$

$$\frac{\partial A_4(r,t)}{\partial z} = -i\alpha_4\chi^{(3)}A_1(r,t)A_2^*(r,t)A_3(r,t)e^{i\Delta kz} \tag{1.47d}$$

where $\alpha_j \equiv \frac{P_F\mu_0\omega_0 c}{2.n_j.8} \equiv \frac{3\mu_0\omega_0 c}{8.n_j}$ and $(\Delta k \equiv k_4 + k_2 - k_1 - k_3)$ is the *wave vector mismatch*.

It is worth noting that the effect that dominates is the one for which corresponding phase-matching term $e^{i\Delta kz}$ approaches to unity ($\Delta k = 0$). Acting on the phase-matching, it is possible to select the desired effect. We will discuss in more detail the *phase-matching condition* in the next chapter.

Here we have arrived at *four coupled equations* (1.47) for the representative process governing the amplitudes of the interacting four fields. In the following chapters, we will use these equations to describe the CARS, SRS and RIKES processes. These coupled equations can be solved collectively only with numerical methods, or introducing some assumptions. We will use the second option to solve each equation separately to understand what happens to a given frequency component.

Chapter 2

CARS and SRS

This chapter provides a physical insight into the processes of Coherent anti-Stokes Raman Spectroscopy (CARS)and Stimulated Raman Spectroscopy (SRS), which are the most widely applied to the field. Particular attention is given to the problem of non-resonant background (NRB) associated with the processes and its effect on CARS. A short description of some NRB suppression techniques is included. A brief overview of the state-of-the-art of CARS and SRS concludes the Chapter.

2.1 Coherent ant-Stokes Raman Spectroscopy

Coherent anti-Stokes Raman Spectroscopy (CARS)[2; 38] is a well established label-free non-invasive nonlinear spectroscopy technique and is one of a number of different Coherent Raman processes that have been developed since the availability of reliable pulsed lasers sources. It is rapidly gaining recognition for non-invasive biomedical imaging of cells and living tissues. In comparison with spontaneous Raman spectroscopy, CARS offers the advantages of higher signal levels allowing for video-rate imaging even with moderate excitation power levels. CARS is associated with the conversion of two laser beams into a coherent laser-like beam at the anti-Stokes frequencies. Because of its anti-Stokes character, CARS radiation is spectrally isolated from the input beams(Figure 2.1(b)), and typically also from parasitic fluorescence background.

In CARS, in general, two narrowband pulses, the pump and Stokes with their angular frequencies ω_p and ω_s respectively, are focused on the sample and their

difference frequency $(\omega_p - \omega_s)$ is tuned to a Raman-active molecular vibration Ω. When this occurs, a strong anti-Stokes signal called *CARS signal* is generated at the angular frequency $\omega_{as} = 2\omega_p - \omega_s$, providing a chemically specific signature that can be used to uniquely identify the molecule. The corresponding energy-level diagram for CARS is shown in Figure (2.1(a)).

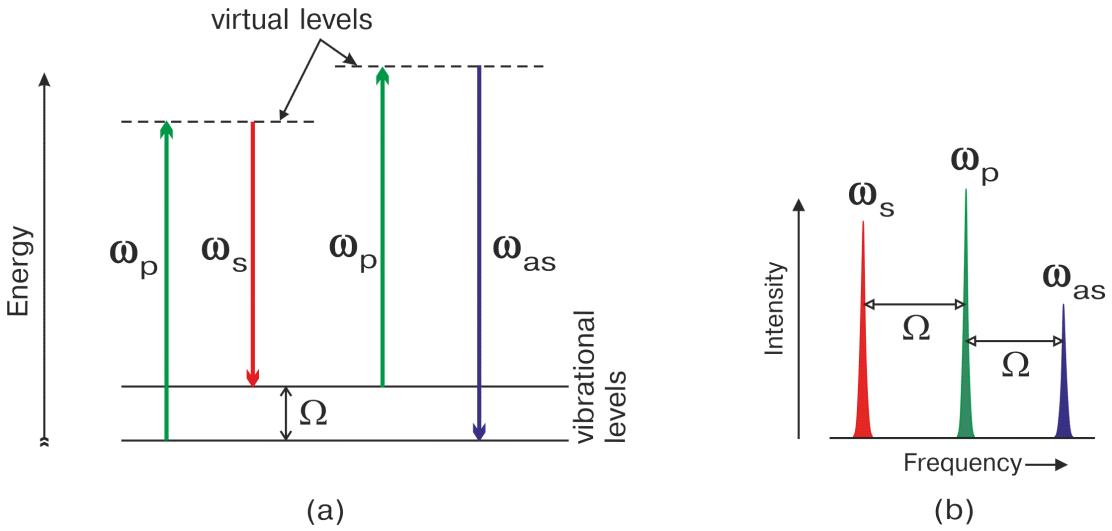


Figure 2.1: (a) Energy-level diagram for CARS, (b) Spectral positions of the beams

The first CARS was reported by R. W. Terhune[39] in 1963 as a by-product of stimulated Raman emission. Later in the same year, Maker and Terhune[1] demonstrated CARS from several samples by using a 0.1J pulses from Ruby laser, as a pump and a stimulated Raman emission from benzene as a Stokes. The derivation of that Stokes generated second beam, justifies the adoption of the word *Stokes* for the second input beam in Coherent Raman terminology.

In CARS spectroscopy, typically ω_s is varied to sweep $\omega_p - \omega_s$ over a molecular vibrational resonance Ω. The intensity of the beam at ω_{as} changes as a function of $\omega_p - \omega_s$. This intensity spectrum constitutes a CARS spectrum. On the other hand, in CARS microscopy, $\omega_p - \omega_s$ is often kept fixed at a particular molecular vibrational resonance Ω, while the beams are scanned over the sample area and the CARS signal is registered from each point. Sample scanning can be achieved either through galvo-mirrors or by moving the sample transversely with respect to the input beams with the help of a piezo translator. This topographical intensity image is called *CARS image* of the sample.

2.1.1 The CARS process

As discussed in the last Chapter CARS belongs to four-wave mixing processes, since it involves two photons from the pump beam and one photon from the Stokes beam to generate a photon at anti-Stokes frequency. This CARS is also known as *degenerate CARS*, because it involves the two pump photons at the same frequency. On the other hand, CARS process can also be achieved by involving the three different photons called *pump*, *Stokes* and *probe* at optical frequencies ω_p, ω_s and ω_{pr} respectively and generating fourth photon at anti-Stokes frequency. This is known as *non-degenerate CARS*. The degenerate CARS (normally refer as CARS)is common in practice, because it requires simple two-beam configuration.

A quantitative description of CARS can be obtained by interpretation of the *four coupled equations* (1.47) derived in Section (1.4). By making the assignment :

$$\begin{aligned} \omega_1 \equiv \omega_p \quad \omega_2 \equiv \omega_s \\ \omega_3 \equiv \omega_p \quad \omega_4 \equiv \omega_{as} \end{aligned} \tag{2.1}$$

Equations (1.47) become:

$$\frac{\partial A_p(r,t)}{\partial z} = -i\alpha_p \chi^{(3)} A_s(r,t) A_p^*(r,t) A_{as}(r,t) e^{-i\Delta k z} \tag{2.2a}$$

$$\frac{\partial A_s(r,t)}{\partial z} = -i\alpha_s \chi^{(3)} A_p(r,t) A_p(r,t) A_{as}^*(r,t) e^{i\Delta k z} \tag{2.2b}$$

$$\frac{\partial A_p(r,t)}{\partial z} = -i\alpha_p \chi^{(3)} A_p^*(r,t) A_s(r,t) A_{as}(r,t) e^{-i\Delta k z} \tag{2.2c}$$

$$\frac{\partial A_{as}(r,t)}{\partial z} = -i\alpha_{as} \chi^{(3)} A_p(r,t) A_s^*(r,t) A_p(r,t) e^{i\Delta k z} \tag{2.2d}$$

where $\alpha_j \equiv \frac{3\mu_0\omega_0 c}{16.n_j}$; [$P_F = 3$ in equations (1.47)] and $\Delta k \equiv k_{as} + k_s - 2k_p$ is in the *phase-matching term*.

The first and the third equations refer to the pump field, the third equation is related to the Stokes field and the fourth, the most interesting one, is for CARS because it describes the behavior of the anti-Stokes beam. Such equations can be easily interpreted by making the assumption of small pump and Stokes depletion, which is typically encountered in most experiments.

By placing, $A_p(r,t) = A_p \backsimeq constt.$ and $A_s(r,t) = A_s \backsimeq constt.$,

integration of equation(2.2d) over a length L gives:

$$\begin{aligned}\int_0^L dA_{as}(r,t) &= \int_0^L \left[-i\alpha_{as}\chi^{(3)}A_pA_s^*A_pe^{i\Delta kz}\right]dz \\ &= -i\alpha_{as}\chi^{(3)}A_pA_s^*A_p\int_0^L e^{i\Delta kz}dz\end{aligned} \tag{2.3}$$

After simple algebra and with the initial condition $A_{as}(0,t)=0$, one obtains:

$$A_{as}(L,t) = -i\alpha_{as}\chi^{(3)}A_pA_s^*A_pL\left[e^{\frac{i\Delta kL}{2}}\right]sinc\left(\frac{\Delta kL}{2}\right), \tag{2.4}$$

which corresponds to an intensity:

$$\begin{aligned}I_{as}(L,t) &\propto |A_{as}(L,t)|^2 \\ &= \alpha_{as}^2|\chi^{(3)}|^2I_p^2I_sL^2sinc^2\left(\frac{\Delta kL}{2}\right)\end{aligned} \tag{2.5}$$

Equation(2.5) highlights the main CARS properties:

- CARS intensity is directly proportional to the Stokes intensity and to the square of the pump intensity.
- CARS intensity is directly proportional to the square of the interaction length L within the sample, provided phase-matching is satisfied ($\Delta k = 0$).
- *Phase-matching* term $sinc^2\left(\frac{\Delta kL}{2}\right)$ places a limitation to the interaction length L for a given wave vector mismatch Δk, the limit being given by the condition $\Delta k.L_c < (\pi \approxeq 3.14rad.)$, where L_c is called the *Coherence interaction Length*. The phase-matching condition makes the CARS signal to be generated coherently only in a defined direction, as shown by the wave vector diagram reported in Figure(2.2).

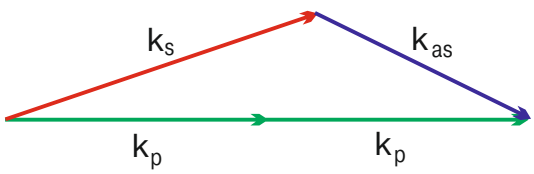


Figure 2.2: Wave vector diagram for phase-matching condition in CARS

In CARS microscopy, under tight focusing conditions, the large angular dispersion of the wave-vectors of pump and Stokes relaxes the phase-matching

condition, and makes the CARS signal to be generated in a well defined cone of wave vector[40].

- CARS intensity is directly proportional to $|\chi^{(3)}|^2$ where $\chi^{(3)}$ is proportional to the number of oscillators per unit volume. Hence CARS intensity is proportional to the square of the molecular density (N^2), while we should recall from Section (1.2) that the intensity of spontaneous Raman scattering is linearly proportional to the concentration of the sample. As deeply described in the next paragraph, the squared dependence of $\chi^{(3)}$ strongly affects the spectral CARS response, due to the interplay between non-resonant and resonant $\chi^{(3)}$ terms.

2.1.2 Presence of non-resonant background in CARS and its effect

Although CARS signal is spectrally isolated from the input beams and also from any type of fluorescence linear background generated by the input beams, yet CARS suffers from the presence of a nonlinear background.

The presence of non-resonant background (NRB) can be understood by recalling that $\chi^{(3)}$ can be written by equation(1.16) as:

$$\chi^{(3)}(-\omega_{as};\omega_p,-\omega_s,\omega_p) = \left(\chi_{Re}^{(3)R} + i\chi_{Im}^{(3)R}\right) + \chi_{Re}^{(3)NR} \tag{2.6}$$

As described in Chapter 1, NR part of $\chi^{(3)}$ is contributed by both, the investigated molecules through a non-resonant FWM mechanism reported in panel(b) of Figure(2.3), and the other molecules in the sample through the mechanism shown in panel(c) of Figure(2.3). The mechanism reported in panel(a) of Figure(2.3) contributes to resonant part of the $\chi^{(3)}$

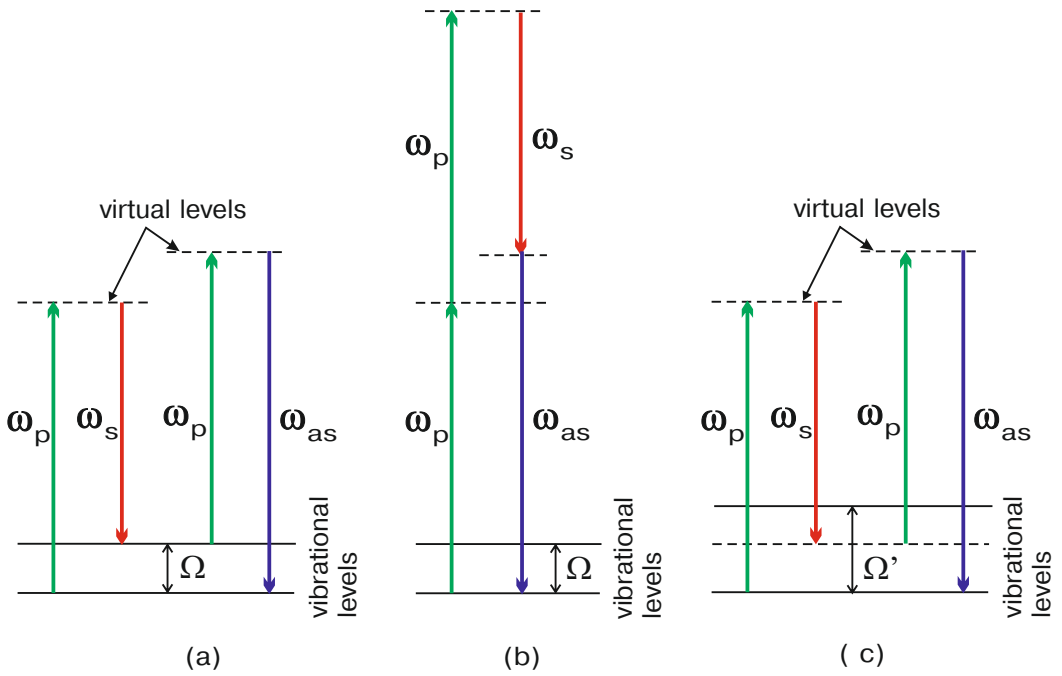


Figure 2.3: Energy diagram of Coherent anti-Stokes (a)Resonant Raman signal and (b)non-resonant signal with $\omega_p - \omega_s$ at vibrational resonance with the molecule and (c)non-resonant signal with $\omega_p - \omega_s$ not at vibrational resonance with other molecule.

Effect of NRB on CARS signal

The NR part of $\chi^{(3)}$, which is spectrally flat as described in Chapter 1, does not merely add a constant background to the CARS signal. If it were the case, background removal would be straight forward. Instead the resonant and non-resonant responses, both being coherent, interfere with each other and the overall CARS signal is spectrally distorted. This fact can be easily understood with the help of equation(2.5), which gives CARS intensity as:

$$I_{as} \propto |\chi^{(3)}|^2 \tag{2.7a}$$

$$\cong |\left(\chi_{Re}^{(3)R} + i\chi_{Im}^{(3)R}\right) + \chi_{Re}^{(3)NR}|^2 \tag{2.7b}$$

$$\cong |\chi_{Re}^{(3)R}|^2 + |\chi_{Im}^{(3)R}|^2 + |\chi_{Re}^{(3)NR}|^2 + 2|\chi_{Re}^{(3)R}||\chi_{Re}^{(3)NR}| \tag{2.7c}$$

Spectral shapes of individual $\chi^{(3)}$ squared terms, $|\chi_{Re}^{(3)R}|^2$, $|\chi_{Im}^{(3)R}|^2$ and $|\chi_{Re}^{(3)NR}|^2$, are plotted in panel(a) of the Figure(2.4) with $\Omega = 2945cm^{-1}$ and $\gamma = 1.5cm^{-1}$. In panels(b), (c) and (d), overall $|\chi^{(3)}|^2$ is plotted for different values of $|\chi^{(3)R}/\chi^{(3)NR}|$ values.

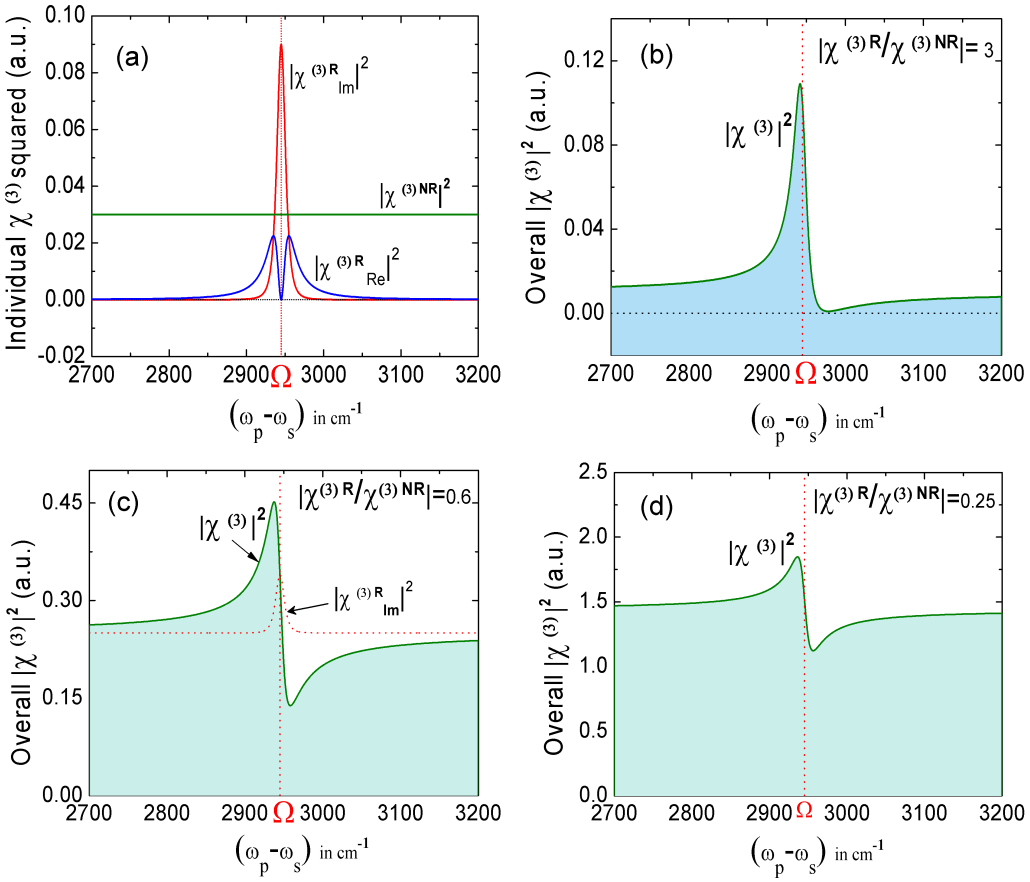


Figure 2.4: (a)The spectra of the squares of individual $\chi^{(3)}$ terms; and (b),(c),(d) are the spectra of overall $|\chi^{(3)}|^2$ for $|\chi^{(3)R}/\chi^{(3)NR}|$ values 3.0, 0.6 and 0.25 respectively; $\Omega = 2945cm^{-1}$ and $\gamma = 1.5cm^{-1}$.

These graphs highlight the following effects on CARS signal:

- Spectral shape of the CARS signal becomes asymmetric and differ from the Lorentzian spectral profile of the spontaneous Raman due to the presence of interference term [last term in equation2.7(c)]. This interference term is referred as non-resonant background(NRB).
- The CARS signal peaks at a slightly red-shifted frequency with respect to the resonance Ω.
- The CARS spectral response is sitting on a non-zero base-line.

These effects become more prominent upon increasing the non-resonant contribution. Panel(d) of Figure(2.4) reports such a case where $|\chi^{(3)R}/\chi^{(3)NR}| = 0.25$. It

is obvious that NRB is dominating over the CARS signal. It is worth noticeable that experimentally such a big $\chi^{(3)NR}$ contribution can come from molecules that surround the targeted ones (for example, water molecules in biological samples).

These all conclude that CARS technique faces a problem while probing a small concentration of molecules, because in that case, NRB will overwhelm the output and CARS features will be buried inside this. It can be difficult to recognize a given molecule in the presence of a non-resonant background that shifts its resonance by a quantity which is not a-priori known.

Hence there is a requirement of NRB suppression for CARS spectroscopy technique. In fact, many techniques has already been proposed to suppress or avoid the NRB contribution in CARS process.

2.2 NRB suppression techniques

Numerous NRB suppression methods for CARS has been developed. The most important ones being:

(1) Epi-detection CARS (E-CARS)[41; 42; 43; 44]

(2) Counter-propagating CARS (C-CARS)[45]

(3) Polarization-sensitive CARS (P-CARS)[3; 4; 5; 6; 7; 8; 9]

(4) Frequency modulation CARS (FM-CARS)([13; 14])

(5) Time-resolved CARS (TR-CARS)[15]

(6) Interferometric CARS (I-CARS)[10; 11; 12]

(7) Pulse-shaping femtosecond excitation

(8) Phase-retrieval CARS

(9) Focus-engineered CARS

A brief description of the important ones are hereafter reported:

2.2.1 Epi-detection CARS

Microscopy under tight focusing condition provides wave vectors for pump and Stokes in a cone with large angle, and hence relaxes the phase-matching condition. As a result, CARS signal is also generated in a wide cone. Even backward scattering of CARS signal is possible in a heterogeneous and complex sample

having small scatterer molecules with their sizes comparable or smaller than the generated CARS wavelength. Alternatively backward CARS can be generated from reflection at a $\chi^{(3)}$ discontinuity within the sample. Backward scattered off CARS signal is called *epi-CARS* (while homogeneous isotropic media in general gives CARS signal in forward direction following the phase-matching). Epi-CARS from a highly scattering tissue could be high enough to allow for in-vivo video-rate($\sim$ 30 frames per second) imaging[46]. This epi-detection CARS method can be utilized to isolate CARS signal, coming from tiny molecule, from signal generated by bulky substrate molecules. In this way we can cancel NRB coming from the substrate to some extent. But this method filters the signal based on particle size rather than using some vibrational contrast mechanism, the NRB from tiny particles will still distort the epi-CARS signal and spectral sensitivity is limited.

2.2.2 Counter-propagating CARS

In counter-propagating CARS scheme, the pump and Stokes beams are propagating collinearly but fall on the sample from opposite directions. In this case, in principle, their wave vectors are completely out of the phase-matching condition, and no CARS signal is generated. But in practice, the presence of smaller molecules with their sizes compared to or smaller than the pump and Stokes wavelengths or the presence of discontinuity interface for $\chi^{(3)}$ within the sample, can scatter pump and Stokes photons, and they can be brought into phase-matching condition to generate CARS signal from tiny target molecules. In this way, we can avoid signal generation from the rest of the bulk sample. Drawbacks of this method are very weak signal level, complex experimental configuration and filtering based on particle size as in epi-CARS. Many wide-field CARS imaging setups are using this method[47; 48; 49].

2.2.3 Polarization-sensitive CARS

To suppress the NRB, polarization sensitive CARS(P-CARS) utilizes the different polarization properties of electronic and Raman contributions to the third-order susceptibility $\chi^{(3)}$ of the molecule, which can be introduced by use of different

polarization directions of the pump and the Stokes beams. The polarization scheme of P-CARS can be outlined as shown in Figure(2.5). Pump beam is linearly polarized along the X-axis and the Stokes beam is linearly polarized along a direction at angle ϕ with respect to the X-axis. The X- and Y-components of the non-resonant part P^{NR} of the third-order polarization can be written with the help of equation(1.46d) as:

$$P_x^{NR} = 3.\chi_{1111}^{(3)}.{E_p}^2 E_s^*.\cos\phi \tag{2.8a}$$

$$P_y^{NR} = 3.\chi_{1221}^{(3)}.{E_p}^2 E_s^*.\sin\phi \tag{2.8b}$$

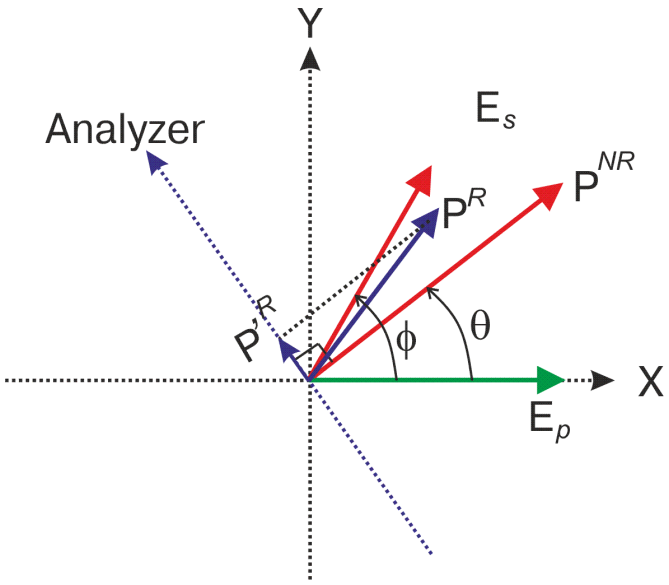


Figure 2.5: Polarization scheme in P-CARS

Far from any electronic resonance, P^{NR} will be linearly polarized with angle θ with respect to the X-axis and given as:

$$P^{NR} = 3.\chi_{1111}^{(3)}.{E_p}^2 E_s^*.\cos\phi/\cos\theta, \tag{2.9}$$

where θ is related to ϕ by the relation $\tan\theta = (\chi_{1221}^{(3)NR}/\chi_{1111}^{(3)NR})\tan\phi = \rho_{NR}.\tan\phi$. ρ_{NR} is the depolarization ratio for non-resonant third-order polarization and following the Kleinman's symmetry, $\rho_{NR} = 1/3$.

The X- and Y-components of the resonant part P^R of the third-order polar-

ization can be written in a similar way as:

$$P_x^R = 3.\chi_{1111}^{(3)}.{E_p}^2 E_s^*.\cos\phi \tag{2.10a}$$

$$P_y^R = 3.\chi_{1221}^{(3)}.{E_p}^2 E_s^*.\sin\phi \tag{2.10b}$$

As the resonant components of $\chi^{(3)}$ are different from the non-resonant components of it, P^R is linearly polarized in different direction from that of the non-resonant counterpart. Hence non-resonant part can be suppressed by using a polarization sensitive detection. For this a polarization analyzer is placed before the detector to cross the linearly polarized non-resonant signal. In this way, the detected part of the P^R through the polarization analyzer will be given as:

$$P'^R = 3.\chi_{1111}^{(3)}.{E_p}^2 E_s^*.(\cos\phi\sin\theta - \rho_R.\sin\phi\cos\theta) \tag{2.11a}$$

$$= 3.\chi_{1111}^{(3)}.{E_p}^2 E_s^*.\cos\phi\sin\theta(1-\rho_R/\rho_{NR}) \tag{2.11b}$$

where $\rho_R = \chi_{1221}^{(3)R}/\chi_{1111}^{(3)R}$ is the depolarization ratio for resonant third-order polarization and is equal to spontaneous Raman depolarization ration for the corresponding Raman line. The value $0 \leq \rho_R \leq 0.75$ is dependent on the symmetry of the vibrational mode.

It is found that vibrational contrast $P_R'^2/P_{NR}'^2$ is maximum with $\theta = 45^0$ which corresponds to $\phi = 71.6^0$ according to the relation $\tan\phi = 3.\tan\theta$.

P-CARS scheme has been applied for background-free CARS spectrum acquisition and resonant CARS imaging[3; 4; 5; 6; 7; 8; 9]. However equation(2.11) suggests that P-CARS signal is a fraction of the total resonant signal, thus P-CARS microscopy suffers from a reduction in resonant signal and it hinders the wide applications of the scheme in detecting weak signal in real biological samples.

2.2.4 Frequency modulation CARS

In frequency modulation CARS, Stokes (or pump) is rapidly switched between two frequencies ω_s and $\omega_{s'}$ with a frequency difference $\delta = \omega_s - \omega_{s'}$ which generates a periodic modulation of the difference frequency $\Omega = \omega_p - \omega_s$. This frequency modulation results in an amplitude modulation of CARS signal ($\Delta I_{CARS,\delta} =$

$I_{CARS,\omega_s} - I_{CARS,\omega_{s'}}$) that can be extracted by using a lock-in detection technique. This is presented in panels(a) and (b) of Figure(2.6) The spectral feature of the resonant CARS signal behaves as a frequency modulation(FM)-to-amplitude modulation converter (as shown in panel(c) of Figure(2.6)). Since the non-resonant contribution to the CARS signal is spectrally constant, it does not contribute to the detected modulation signal and hence is suppressed.

A delicate point is the choice of ω_s and $\omega_{s'}$, for a given spectral CARS feature, that most efficiently suppresses the non-resonant contribution while ensuring high amplitude modulation of the resonant CARS signal. For this, let us recall from equation (2.7) that:

$$I_{CARS} \propto |\chi^{(3)}|^2 \tag{2.12a}$$

$$\cong |\chi^{(3)R} + \chi^{(3)NR}_{Re}|^2 \tag{2.12b}$$

$$\cong |\chi^{(3)R}(\Omega)|^2 + (\chi^{(3)NR}_{Re})^2 + 2Re[\chi^{(3)R}(\Omega)]\chi^{(3)NR}_{Re} \tag{2.12c}$$

From equation(2.12c), at high concentration of resonant molecules, the quadratic term in $\chi^{(3)R}(\Omega)$ dominates, while at much lower concentration of the resonant molecules, the term linear in $\chi^{(3)R}(\Omega)$(that is third term)will dominate because in that case it will get multiplied by a relatively high non-resonant response of the substrate molecules. The overall FM-CARS signal enhancement due to this multiplication is dependent on the peak shift due to the dispersive shape of $Re[\chi^{(3)R}(\Omega)]$. This FM signal can be selected by properly choosing the modulation frequencies ω_s and $\omega_{s'}$. But as the value of non-resonant contribution can vary throughout the heterogeneous sample producing intensity artifacts, hence quantitative detection of the CARS signal becomes difficult. For reliable quantitative measurements, the best choice is to select the modulation frequencies to be $(\Omega \pm \Gamma/2)$. This is reported in panel(c) of Figure(2.6). In this way, it will suppress the linear term efficiently and second term being spectrally flat, already has no contribution to the FM-CARS.

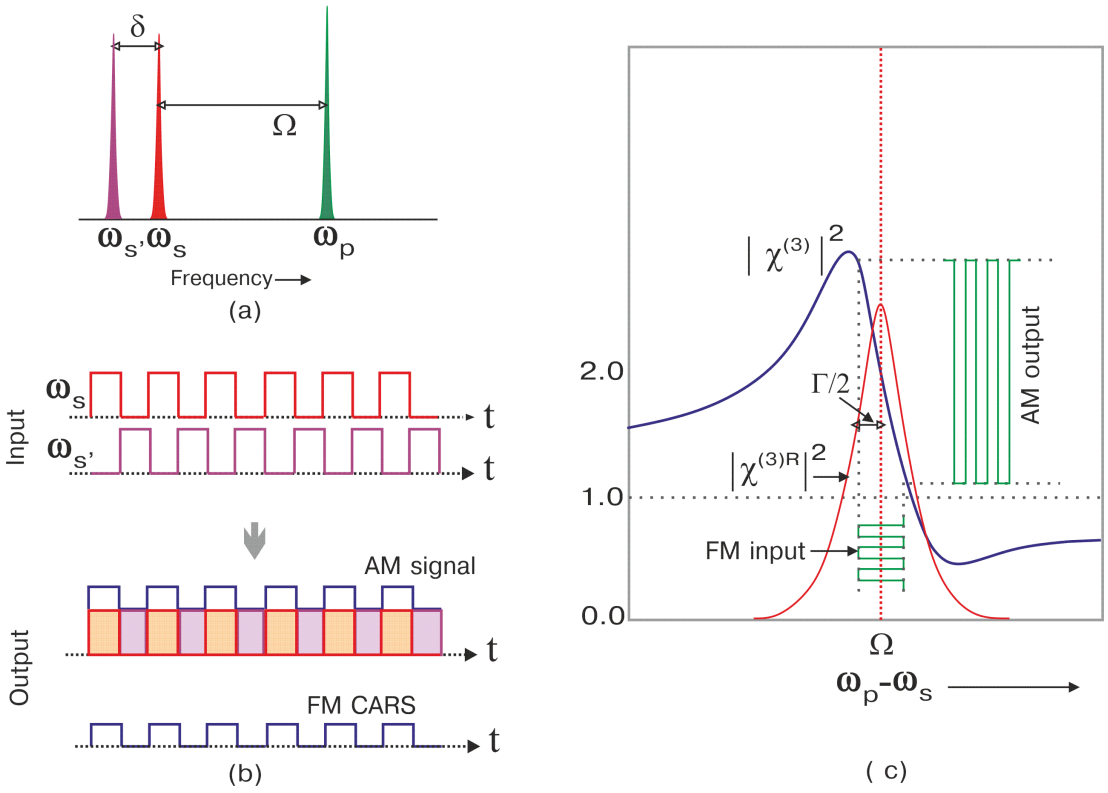


Figure 2.6: Frequency modulation CARS(a)Input frequencies ,(b) Fields in time scale, and (c)Schematic of the process

It is worth noting that in FM-CARS, frequency modulation needs to be done at a high repetition rate in order to separate the modulated signal from the lower frequency laser-noise. An important requirement on the laser side is that FM-CARS approach requires three synchronized pulses at frequencies ω_p, ω_s and $\omega_{s'}$.

2.2.5 Time-resolved CARS (TR-CARS)

Time-resolved CARS (TR-CARS) is a particularly powerful and elegant approach for NRB suppression. TR-CARS utilizes the fact that electronic dephasing is much faster than either the nuclear dynamics of the molecular system or the optical pulses. The non-resonant contribution given by $\chi^{(3)NR}$ and $\chi^{(3)R}_{Re}$ originate from the electronic interaction and hence dephase very fast, while resonant vibrational contribution $\chi^{(3)}_{Im}$ comes from the nuclear dynamics and decay slower. This fact is shown in panel(2b) of Figure(2.7).

TR-CARS is typically applied to non-degenerate CARS. A comparison be-

tween the degenerate CARS and the TR-CARS is reported in Figure(2.7). In TR-CARS, the probe pulse is delayed with respect to the pump/Stokes pair by a time Δt which is sufficiently high to avoid any temporal overlap, while being shorter than the dephasing time of the vibrational level. In such case, the NRB

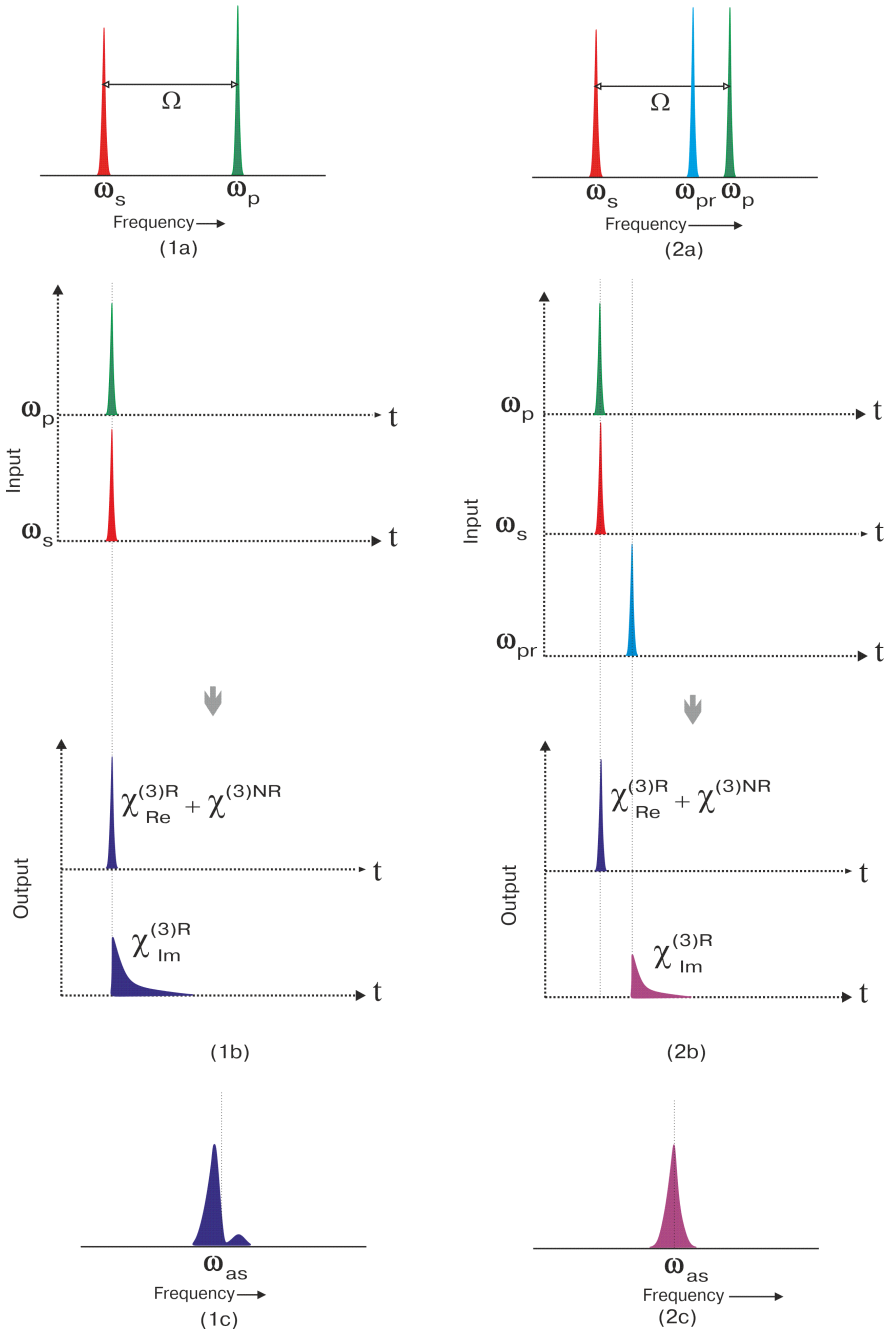


Figure 2.7: (1a)degenerate CARS ,(2a) non-degenerate CARS; (1b) the input pulses and the material response on time scale in degenerate CARS, (2b)the input pulses and the material response on time scale in TR-CARS; (1c) and (2c) are CARS spectral feature in degenerate CARS and TR-CARS respectively.

generated by the four-wave mixing process $\omega_{as} = \omega_p + \omega_{pr} - \omega_s$ is completely suppressed, because it relies on the instantaneous $\chi^{(3)}$ of the medium. The price to be payed is that the time-delayed probe pulse interacts with a vibrational coherence that has been decayed with a dephasing time $T_{2\nu}$, leading to a reduction of the useful CARS signal by $exp(-2t/T_{2\nu})$.

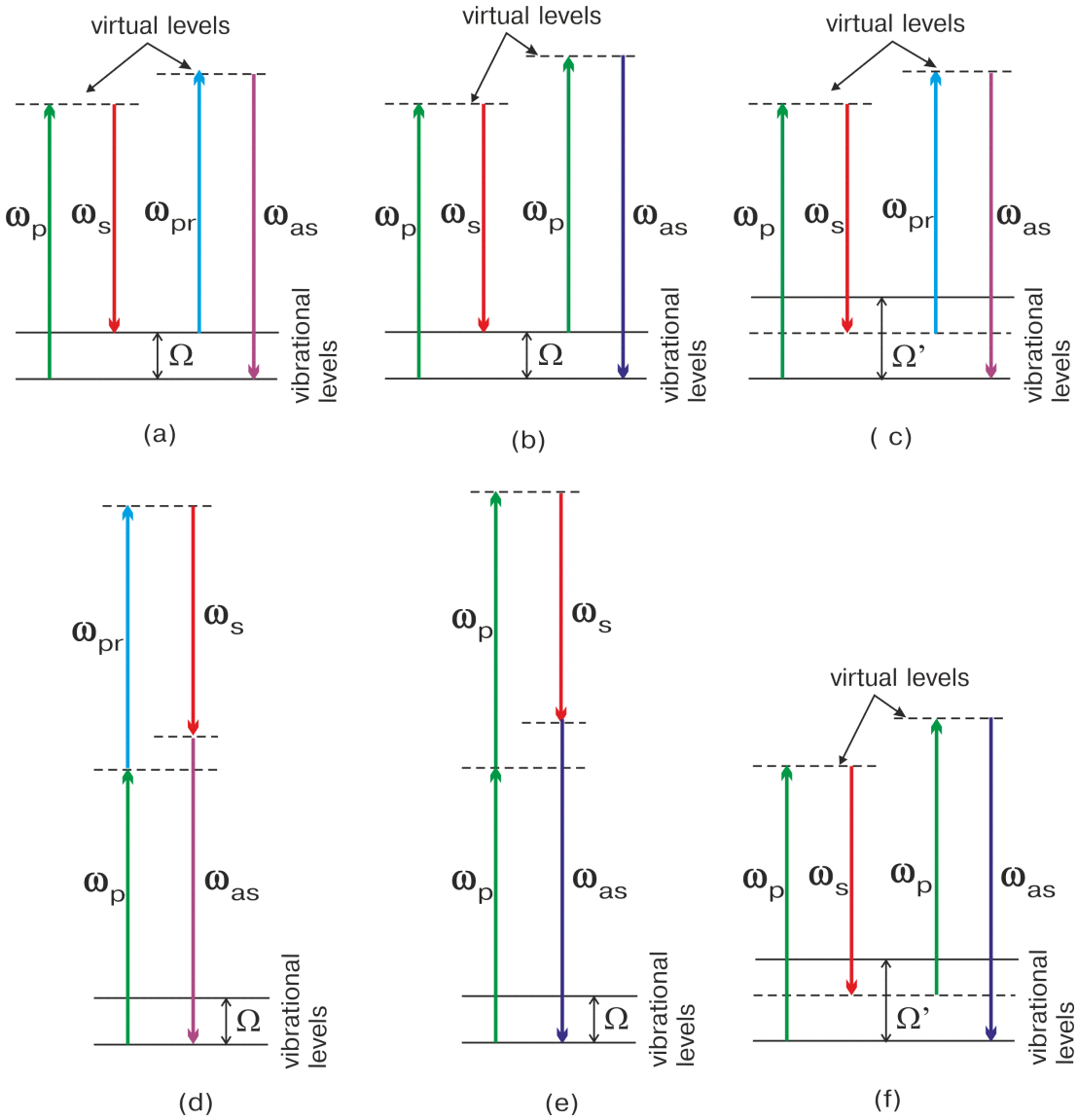


Figure 2.8: Energy-level diagram for:(a)TR-CARS signal,(b) degenerate CARS signal,(c)-(f)different possible mechanisms contributing to NRB, where Ω and Ω' represents the resonances of the investigated molecule and the surrounding molecules respectively.

The panels(a)-(f) in Figure(2.8) show energy-level diagrams of different possible mechanisms which can contribute in TR-CARS process, where mechanisms(b)-

(f) can contribute to NRB. Use of three synchronized pulses in TR-CARS is required in order to prevent spectral overlap with the NRB generated by the FWM process $\omega_{as} = 2\omega_p - \omega_s$ (the mechanisms in panels(e) and (f)), and with the process in panel(b). And the time-delayed probe suppresses the NRB contribution from mechanisms in panels(c)and (d).

The requirement of three synchronized input pulses for TR-CARS makes the excitation set-up a bit complicated.

2.2.6 Interferometric CARS (I-CARS)

Interferometric CARS is a unique background suppression technique which offers the possibility of detecting non-resonant background free CARS signal without any attenuation in the signal. I-CARS requires three phase-coherent laser beams as shown in Figure(2.9). In this approach, the CARS field A_{as} is superimposed with the phase-coherent reference field A_{LO} called *Local oscillator field* at the same optical frequency of the CARS. Then, the overall CARS intensity is given by:

$$I = |A_{as} + A_{LO}|^2 \tag{2.13a}$$

$$= |A_{as}|^2 + |A_{LO}|^2 + 2Re[A_{as}].Re[A_{LO}] + 2Im[A_{as}].Im[A_{LO}] \tag{2.13b}$$

The CARS field A_{as} is given by equation(2.5) as:

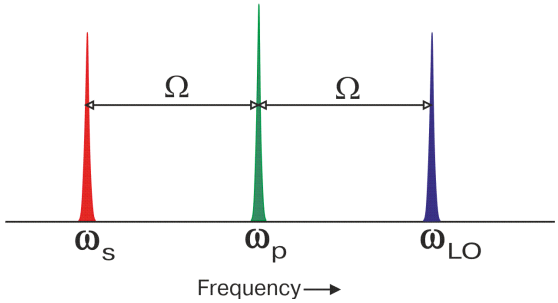


Figure 2.9: Input fields for Interferometric CARS

$$\begin{aligned} A_{as} &\propto A_p^2 A_s^* \chi^{(3)} \\ &\cong A_p^2 A_s^* (\chi_{Re}^{(3)R} + i\chi_{Im}^{(3)R} + \chi_{Re}^{(3)NR}) \end{aligned} \tag{2.14}$$

Introducing above expression, equation(2.13) takes the form:

$$I = |A_{as}|^2 + |A_{LO}|^2 + 2(A_p^2 A_s^*)A_{LO}[(\chi_{Re}^{(3)R} + \chi_{Re}^{(3)NR})\cos\phi + (\chi_{Im}^{(3)R})\sin\phi] \tag{2.15a}$$

$$= I_{as} + I_{LO} + 2\sqrt{I_{(p^2s)}.I_{LO}}[(\chi_{Re}^{(3)R} + \chi_{Re}^{(3)NR})\cos\phi + (\chi_{Im}^{(3)R})\sin\phi] \tag{2.15b}$$

where $A_p^2 A_s^* \cong \sqrt{I_{(p^2s)}}$ is written just for simplicity, and ϕ is the phase difference between the CARS field and the local oscillator field.

The equation (2.15) has the important consequence that the last two interferometric terms containing the real and the imaginary contributions to the signal show orthogonal dependency on ϕ. If ϕ is set to 90^0, the interferometric term containing non-resonant contribution is removed and a response proportional to the imaginary part of the $\chi^{(3)}$ is measured with modulation transfer technique combined with lock-in detection.

The I-CARS has two main advantages over normal CARS:

- Interferometric CARS signal is directly proportional to the concentration of the investigated molecules instead of being its square dependency as in normal CARS. Hence I-CARS can be implemented to quantitative measurement straightforward.

- Instead of attenuating the CARS signal as other background suppression techniques do, it amplifies it by a factor $\sqrt{I_{LO}/I_{(p^2s)}}$.

The strict requirement on laser side is that I-CARS requires three synchronized phase-coherent laser beams at pump, Stokes and anti-Stokes frequencies respectively and this phase relation needs to be maintained while scanning the sample which is hard due to presence of phase related artifacts inside the sample.

So far we have seen that all these NRB suppression techniques are either based on polarization sensitive detection scheme or required synchronized three beams configuration set-ups, and they suffer from a severe reduction in the total available resonant CARS signal. The Stimulated Raman Spectroscopy (SRS) developed in recent years, provides the solution over these difficulties and it directly probes the resonant response of the molecules.

2.3 Stimulated Raman Scattering

Stimulated Raman Scattering (SRS)[19] is another important Coherent Raman Spectroscopy technique which probes the excited vibrational population, to uniquely identify the molecule, instead of vibrational coherence which is detected in CARS [50; 51; 52; 53]. In SRS, the pump and the Stokes with their angular frequencies ω_p and ω_s respectively, are focused on the sample and their difference frequency $(\omega_p - \omega_s)$ is tuned to a Raman-active molecular vibrational resonance Ω. The simultaneous presence of both pump and Stokes beams stimulates the excitation and accelerates the rate of population transfer to the excited vibrational state as compared to that in spontaneous Raman process, by a factor given by [50; 53]:

$$\frac{R_{(stimulatedRaman)}}{R_{(spontaneousRaman)}} = n_{stokes} + 1, \tag{2.16}$$

where $R_{(stimulatedRaman)}$ and $R_{(spontaneousRaman)}$ are the excitation rates in stimulated Raman and spontaneous Raman processes respectively and n_{stokes} is the number of photons present in the optical mode of the Stokes beam. Only a laser beam can provide sufficiently large n_{stokes} to excite efficiently the molecular vibrational level for SRS to be significant over normal Raman. Each excited vibrational phonon is accompanied by absorption of one pump photon and simultaneous creation of one Stokes photon to conserve the energy and momentum during the process. This is reported in panel(a) of Figure(2.10). Overall amplification of the Stokes beam and simultaneous depletion of the pump beam occur. The amplification of the Stokes beam is called *Stimulated Raman Gain (SRG)* and depletion of pump beam is called *Stimulated Raman Loss (SRL)*.This is shown in panel(b) of Figure(2.10). Experimentally, either SRG or SRL is measured to identify the molecule.

Mathematical expression for SRG or SRL can be obtained from coupled equations(1.47)by making the assignment:

$$\begin{aligned} \omega_1 \equiv \omega_2 \equiv \omega_p \\ \omega_3 \equiv \omega_4 \equiv \omega_s \end{aligned} \tag{2.17}$$

and by realizing the fact that the phase-mismatch Δk goes to zero due to the identity:

$$\Delta k \equiv k_4 + k_3 - k_1 - k_2 \equiv k_s + k_p - k_p - k_s = 0$$

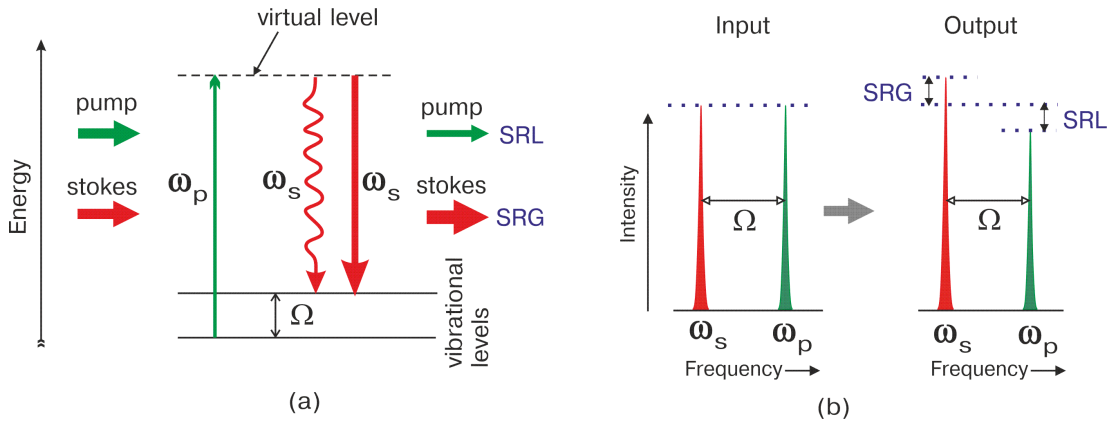


Figure 2.10: (a)Energy level scheme of Stimulated Raman Scattering ,(b) Demonstration of SRG and SRL

The coupled equations(1.47) reduce to:

$$\frac{\partial A_s(r,t)}{\partial z} = -i\alpha_s\chi^{(3)}A_p(r,t)A_p^*(r,t)A_s(r,t) \tag{2.18a}$$

$$\frac{\partial A_p(r,t)}{\partial z} = -i\alpha_p\chi^{(3)}A_p(r,t)A_s^*(r,t)A_s(r,t) \tag{2.18b}$$

With the small depletion assumption $A_p(r,t) = A_p \backsimeq constt.$, we can solve equation(2.18a) for SRG in the case of an interaction length L:

$$\begin{aligned} \int_0^L dA_s(r,t) &= \int_0^L \left[-i\alpha_s\chi^{(3)}A_pA_p^*A_s(r,t)\right]dz \\ &= -i\alpha_s\chi^{(3)}|A_p|^2\int_0^L A_s(r,t)\,dz \\ \Rightarrow A_s(L,t) &= A_s(0,t)e^{-i\alpha_s\chi^{(3)}|A_p|^2L} \end{aligned} \tag{2.19}$$

The exponential term in the above equation(2.19) can be expanded in a Taylor series and neglecting terms of second and higher orders, equation(2.19) takes the form:

$$\begin{aligned} A_s(L,t) &= A_s(0,t)\big(1 - i\alpha_s\chi^{(3)}|A_p|^2L\big) \\ \Rightarrow A_s(L,t) - A_s(0,t) &= -i\alpha_s\chi^{(3)}|A_p|^2A_s(0,t)L \\ \Rightarrow \Delta A_s \equiv A_s(L,t) - A_s(0,t) &= -i\alpha_s\chi^{(3)}|A_p|^2A_s(0,t)L \end{aligned} \tag{2.20}$$

where ΔA_s gives the change in the Stokes field. ΔA_s interferes constructively to the incident Stokes field producing an intensity change at the sample output

given by:

$$S = |A_s + \Delta A_s|^2 \tag{2.21a}$$

$$S = |A_s|^2 + |\Delta A_s|^2 + 2Re(A_s^*.\Delta A_s) \tag{2.21b}$$

$$\Rightarrow S = I_s + \Delta I_s + 2Re(A_s^*.\Delta A_s) \tag{2.21c}$$

In equation(2.21c), first term is the incident Stokes beam intensity, second term represents in general a negligible relative intensity change in Stokes beam as compared to the third term, where in third term heterodyne amplification of ΔA_s occurs by incident Stokes field A_s^*.

The third term can be measured by modulating the pump beam and probing its modulation transfer to the Stokes beam through lock-in detection. This allows the first term to be rejected and SRG signal to be retrieved as. Thus detected SRG signal is:

$$SRG = 2Re(A_s^*.\Delta A_s)/I_s \tag{2.22a}$$

$$= 2Re[A_s^*.\big(-i\alpha_s\chi^{(3)}|A_p|^2 A_s L\big)]/I_s \tag{2.22b}$$

$$= 2Re[-i\alpha_s\chi^{(3)}|A_p|^2|A_s|^2 L]/I_s \tag{2.22c}$$

$$= 2Re[-i\alpha_s\big(\chi_{Re}^{(3)R} + i\chi_{Im}^{(3)R} + \chi_{Re}^{(3)NR}\big)|A_p|^2|A_s|^2 L]/I_s \tag{2.22d}$$

$$\Rightarrow SRG = 2\alpha_s[\chi_{Im}^{(3)R}]I_p L \tag{2.22e}$$

Equation(2.22) shows following remarkable properties of the Stimulated Raman Spectroscopy technique :

- SRS signal is directly proportional to the pump beam intensity.
- SRS is proportional to the interaction length L within the sample, without any phase-matching constraints.
- SRS signal is linearly proportional to the imaginary part of the $\chi^{(3)}$, hence it is inherently *free from non-resonant background* and also linearly proportional to the number density of the target molecules present in the focal volume. It is symmetric and has perfact Lorentzian spectral profile.

2.4 SRS vs CARS

CARS is known from decades and is widely developed. It has been successfully implemented in many fields as a spectroscopic and a microscopic tool. SRS made debut in recent years, yet SRS seems to offer some indispensable advantages over CARS.

In SRS, for example in SRG energy transfer from pump beam to the Stokes beam takes place, while CARS is a scattering process. CARS signal comes from the parametric generation process. In other words, to some extent, SRS can be considered as the nonlinear Raman analog of linear absorption and CARS can be viewed as the nonlinear Raman analog of Rayleigh scattering. The presence of background molecules cannot contribute in SRS signal because they do not have real levels at $(\omega_p - \omega_s)$ to mediate in energy-transfer process, while in CARS any molecule can give a scattering contribution to generate non-resonant background[53].

Some advantages of SRS process over CARS process are listed below:

- The SRS process is inherently free from the non-resonant background while in CARS process, NRB makes the CARS response to be different from that obtained in spontaneous Raman. Hence SRS directly mimics the response given by spontaneous Raman spectroscopy. Already exist spontaneous Raman knowledge can be used straight-forward to interpret the SRS spectra or images.

- The SRS signal has linear dependence on the concentration of target molecules, irrespective of the presence of the solvent molecules. Therefore a quantitative analysis is reliable and straightforward. CARS has quadratic dependence on the concentration of target molecules at high concentration levels, and it switches to a nearly linear dependence at a very low concentration of target molecules with a huge plateau of NRB. Hence CARS is not reliable for quantitative analysis.

- SRS does not require any phase-matching, thus it has a well-defined point-

spread function which can be used directly for image deconvolution. CARS requires phase-matching and hence point-spread function depends on to which extent phase-matching is achieved. In other words, CARS is influenced by spatial coherence artifacts.

- Two-photon fluorescence can contaminate the CARS signal, while SRS process is totally immune to any type of contaminations.

- By use of high-frequency modulation and lock-in detection at high frequency, laser-intensity noise of the Stokes beam can be easily removed in the SRS. Detection sensitivity in SRS can be reached shot-noise limit(from the Stokes beam) in practice. While in CARS (shot-noise comes from the non-resonant background), it is hard to reach this ideal situation, because high-frequency modulation techniques are hard to implement in CARS, when it is done NRB always leaves some spurious intensity noise.

On the other hand, CARS approach still presents some advantages over SRS:

- In SRS, a very tiny signal needs to be detected on top of a huge background and sensitivity levels of nearly 10^{-7} are required over time of about one second to perform quick imaging. Hence availability of high sensitivity detection systems is essential. For the CARS, there is no such strict demand on detector side.

- CARS can be easily implemented in multi-color imaging to detect more than one species simultaneously. Multiplex CARS has been developed to acquire whole vibrational spectra at once of a sample. These are far from being experimentally demonstrated in SRS technique.

Multiplex CARS (*M-CARS*, sometimes also referred as *broadband CARS*)is a well-known technique now. We will discuss it in brief in the next Section.

2.5 Broad-band CARS

In narrow band CARS scheme, both picosecond pump and picosecond Stokes pulses are focused onto the sample, and usually the Stokes optical frequency ω_s is

varied continuously to sweep frequency difference $(\omega_p - \omega_s)$ across a Raman-active molecular mode $\Omega = \omega_p - \omega_s$, to obtain the full CARS spectrum of the sample. But it is time-consuming to record a CARS spectrum by tuning this way the Stokes frequency point by point. Also this makes it difficult to follow dynamical changes in a CARS spectrum. It would be better to obtain full CARS spectrum at once.

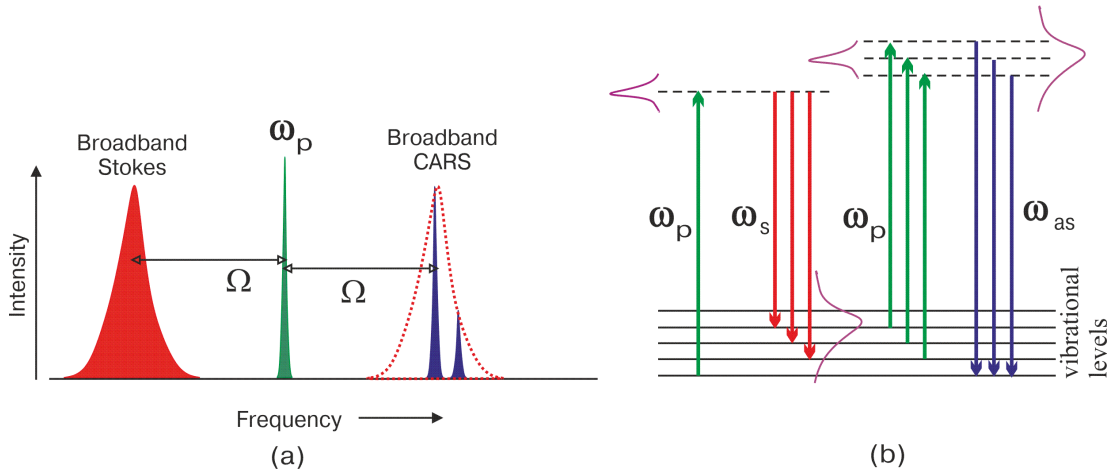


Figure 2.11: Multiplex CARS (a) Scheme (b) Energy level diagram.

This can be done in multiplex CARS(also known as *broadband CARS*) by applying a picosecond pump beam and a femtosecond Stokes beam focused onto the sample[54]. The femtosecond Stokes pulse owing to a broad spectral width, allows simultaneous detection over a wide range of Raman shifts. The energy level diagram of M-CARS with a picosecond pump and a femtosecond Stokes is shown in Figure (2.11).

As in the case of narrowband CARS spectroscopy, the major shortcoming in broadband CARS spectroscopy is the existence of a non-resonant background having no chemical specificity that limits the detection sensitivity and also distort the M-CARS spectral features. Many NRB suppression techniques, mainly Polarization-sensitive CARS and time-resolved CARS etc, have been successfully applied to the M-CARS to get rid of this difficulty. We will demonstrate an experiment in Chapter 4, in which time-resolved NRB suppression scheme is implemented to broadband CARS spectroscopy performed with a single laser oscillator.

2.6 State of the art for CARS and SRS

2.6.1 Laser optimal parameters for CRS

CRS requires two synchronized input beams (optionally, a third input beam also synchronized with the previous two, for example, in non-degenerate CARS and CARS incorporated with a NRB suppression technique) at different frequencies with the possibility to tune their frequency difference to match a molecular vibrational frequency of the investigated molecule. Being a nonlinear process, CRS requires high input intensities to significantly induce third-order polarization. Pulsed lasers are usually employed to provide these high intensity input pulses. Another advantage of using pulsed lasers is that subsequent on and off of the pulses reduces excessive heat dissipation inside the material while ensuring high conversion efficiency.

When performing CRS spectroscopy/microscopy, first constraint comes from the spectral region. This region should comply on the one hand with the material transparency range and on the other hand, on the need to avoid TPA, whose onset significantly lowers the damage threshold of the material. It has been reported that laser wavelength shorter than 800nm can cause a huge amount of multiphoton absorption by ultraviolet electronic resonances[55]. Multiphoton absorption especially two-photon absorption(TPA) is always a main cause of sample damage. Typically, wavelengths between 780nm and 1300nm, as reported in Table(**2.1**), are used which comply with the above constraint, and offer at the same time a high penetration depth due to reduced scattering at these wavelengths by turbid samples (for example highly scattering tissue samples),and hence allowing for deeper CRS imaging inside the sample. Upper limit for laser wavelength comes from the surrounding of the sample. Mostly all the biological samples have $80-90\%$ of water in it, and water has a strong absorption band starting from 1300 nm. The entire chemically important vibrational frequency tunability range falls within $200-3600\ cm^{-1}$. Thus optimal wavelength range for both pump and Stokes pulses is from 780 to $1300nm$. Exceptional more suitable ranges may differ depending upon the properties of investigating material.

Table 2.1: Laser optimal parameters for CRS microscopy/spectroscopy[55].

Parameter	Optimal Range
Pump wavelength	$780 - 980$ nm
Stokes wavelength	$1000 - 1300nm$
Pulse duration	$2 - 7\ ps$
Spectral bandwidth	$3 - 5\ cm^{-1}$
Pulse energy	0.1-1nJ
Pulse repetition rate	$50 - 100$ MHz

Typical linewidths of molecular vibrational transitions are on the order of $10-20cm^{-1}$, which corresponds to the bandwidth of nearly an $1ps$-long transform-limited Gaussian pulses in near IR range. Thus a laser system providing femtosecond pump and Stokes pulses, even if a frequency-difference centered at a vibrational resonance, will contribute an exceedingly high NRB in CARS and a poor SRG/SRL in SRS, because of the small acceptance bandwidth of the resonance band. The highest conversion efficiency for CRS signal can be achieved by using laser pulses with duration comparable to the linewidth of the molecular vibrational transition. The use of longer duration pulses will lead to a poor spectral resolution. A good compromise between conversion efficiency and spectral resolution is nearly $2 - 7$ picosecond pulses for both pump and Stokes [41]. In case of multiplex CARS, pump is generally in picosecond regime providing spectral resolution while femtosecond Stokes covers the full vibrational range. Since CRS signal scales with the intensities of the pump and the Stokes beams, the pulsed lasers with high pulse energy is preferable, but their is a trade-off between pulse energy and optical damage threshold power for the sample. The optimal pulse energy for most biological samples for the picosecond pulse ranges between $0.1 - 1$ nJ. The high pulse repetition rate($50 - 100MHz$) reported in the Table, is needed for high acquisition speed for imaging.

2.6.2 Laser sources for CRS

The central challenge is to generate tunable synchronized pump, Stokes and the optional probe pulses from a given laser source. The two laser pulse trains coming out from two different oscillators are generally not synchronized because this requires their cavity lengths to be carefully matched and thus locking electronics to be developed.

In the initial development of CARS spectroscopy, dye laser has been used as a tunable high power laser sources, providing very narrow linewidth pulses good for investigating diatomic gas molecules. One arrangement used by several groups[56; 57; 58; 59; 60], is reported in Figure(2.12a). It utilizes two dye lasers pumped by a single nitrogen laser, generating two high power individually tunable pulse trains. The dye laser cavities are electronically locked to synchronize the two pulse trains. Although nitrogen laser can be operated at high repetition rates to allow for high acquisition speed, yet, because of transverse pumping, the spatial quality of beams from nitrogen laser-pumped dye lasers is poor. Another CARS apparatus, reported in panel(C) of Figure(2.12), utilizes pump pulses from a frequency-doubled Nd:YAG laser and the tunable Stokes pulses from a dye laser pumped by the same frequency-doubled Nd:YAG laser[61; 62]. This configuration has two advantages over the previous one: firstly, Nd:YAG laser provides longitudinal pumping of the dye laser which implies better beam quality, secondly, it requires only one dye laser. Dye laser based apparatus has less tunable range and their wavelength range is away from optimal requirement for the most of the biological samples. They are not the versatile source suitable for imaging bulk materials due to their narrow linewidth pulses.

Very soon, the availability of broadly tunable laser sources, like Ti:sapphire lasers and optical parametric oscillators(OPO), led to improve the CARS apparatus for biological imaging. One such arrangement offering broad tunability range is shown in panel(b) of Figure(2.12), where pump and Stokes pulses are provided by a pair of Ti:sapphire lasers tunable from 700 to 1100nm, both pumped by a frequency doubled CW Nd:Vanadate laser[63; 64; 65; 66]. In another apparatus, a combination of a femtosecond Ti:sapphire laser,tunable from 700 to 1000nm, and

an OPO is used [panel(d) of Figure(2.12)]. One part of Ti:sappire laser pulses works as pump, and the other part is used to pump the OPO to derive tunable (from 1100 to 1600nm) Stokes pulses[41].

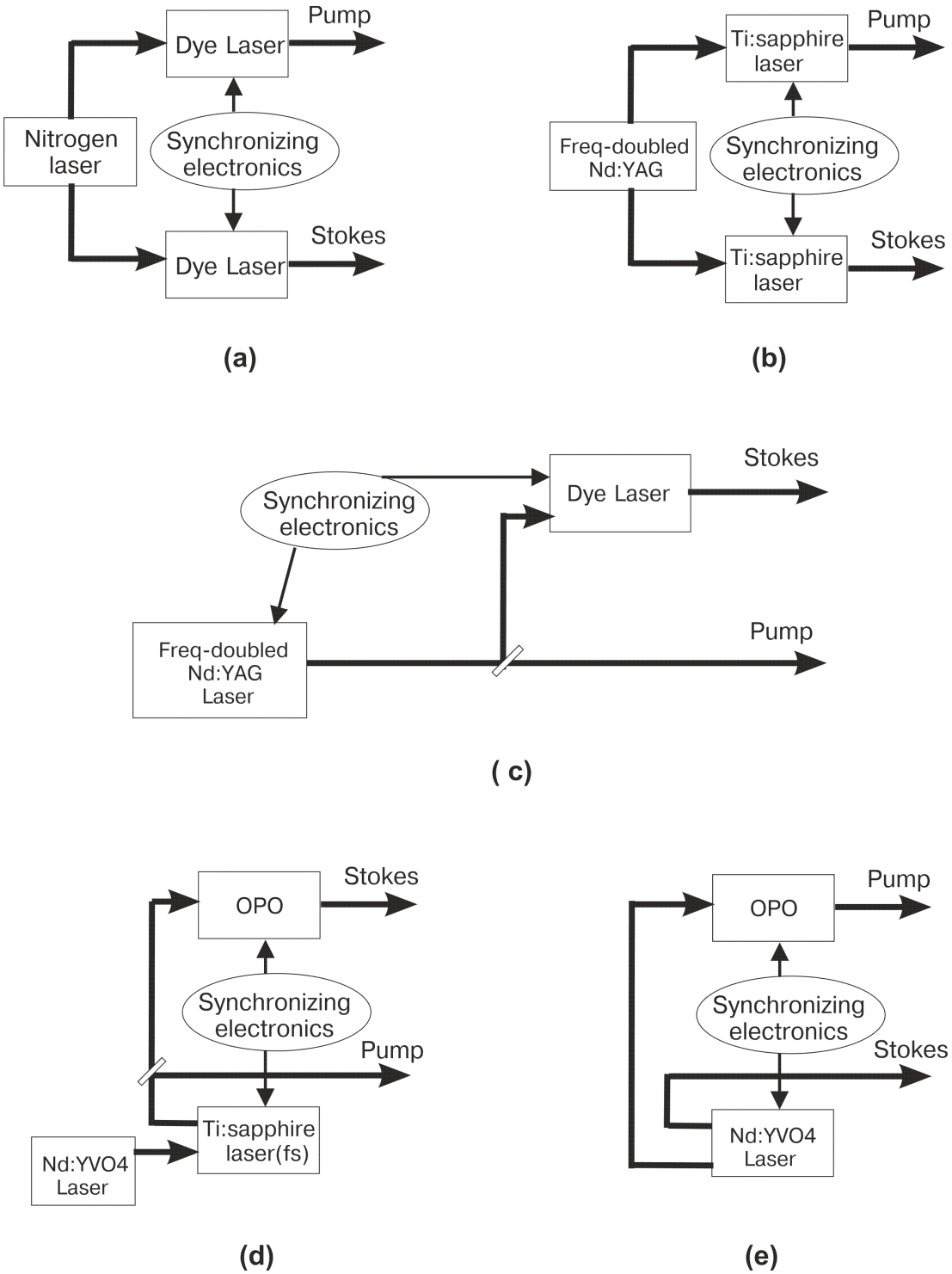


Figure 2.12: Traditional setups for CRS using two synchronized laser oscillators.

In a slightly different arrangement from the previous one, reported in panel(e) of Figure(2.12), a small part of a picosecond 1064nm pulses of a high power Nd:YVO_4 laser is utilized as Stokes, and the rest of the part is frequency-doubled to pump an OPO to get tunable pump pulses[19]. In OPO, the tunability is achieved by temperature-tuning of a non-critically phase-matched LBO crystal. Noticeable that above mentioned all apparatus utilizes two different laser oscillators to provide pump and Stokes pulses, hence synchronizing electronics are involved to carefully match their cavity lengths.

An elegant way is to derive inherently synchronized pump and Stokes pulses from a single laser oscillator. In fact, the pioneering work of CARS by Maker and Terhune[1] has made use of one oscillator [panel(a) in Figure(2.13)]. That system utilized two fixed wavelength beams: one, directly a part from a ruby laser, acted as pump, and the second, generated by Stimulated Raman scattering in Benzene shined by the same ruby laser and separated by $992cm^{-1}$ from pump, acted as Stokes. These fixed beams were useful only for probing resonant CARS signal from Benzene or non-resonant cross-sections of other materials. For recording CRS spectra, tunable beams are required. Light sources for CRS based on a single laser oscillator face a basic difficulty that although the easiest way of creating frequency-shifted Stokes pulses by a nonlinear effect requires a femtosecond input pulse because of its high peak power, yet a picosecond pump pulse is required to assure satisfactory spectral resolution. This implies that the single oscillator should work in both fs and ps pulse regime at the same time which is impossible. But a fs pulsed output of the oscillator can be spectrally compressed to derive nearly transform-limited ps pulses. Based on this idea, in the recent years, many groups have proposed different strategies for light source for CRS microscopy starting from a single laser oscillator.

A light source where both pump and the Stokes pulses are derived from a single oscillator i.e. OPO which itself is pumped by another oscillator, is used by Xie et. al.[67]. Sketch of the source is shown in panel(b) of Figure(2.13), where a frequency-doubled Nd:Vanadate laser pumps a commercially available dual wavelength OPO. This broadly tunable OPO is based on a noncritically

phase-matched crystal for parametric down conversion. The signal and idler frequencies are continuously temperature tunable about the degeneracy point(signal and idler wavelengths at 1064 nm) to 670nm for its signal beam and to 2300nm for its idler beam, making it possible to cover entire chemically important vibrational frequency range. Another light source employing a single un-amplified fs

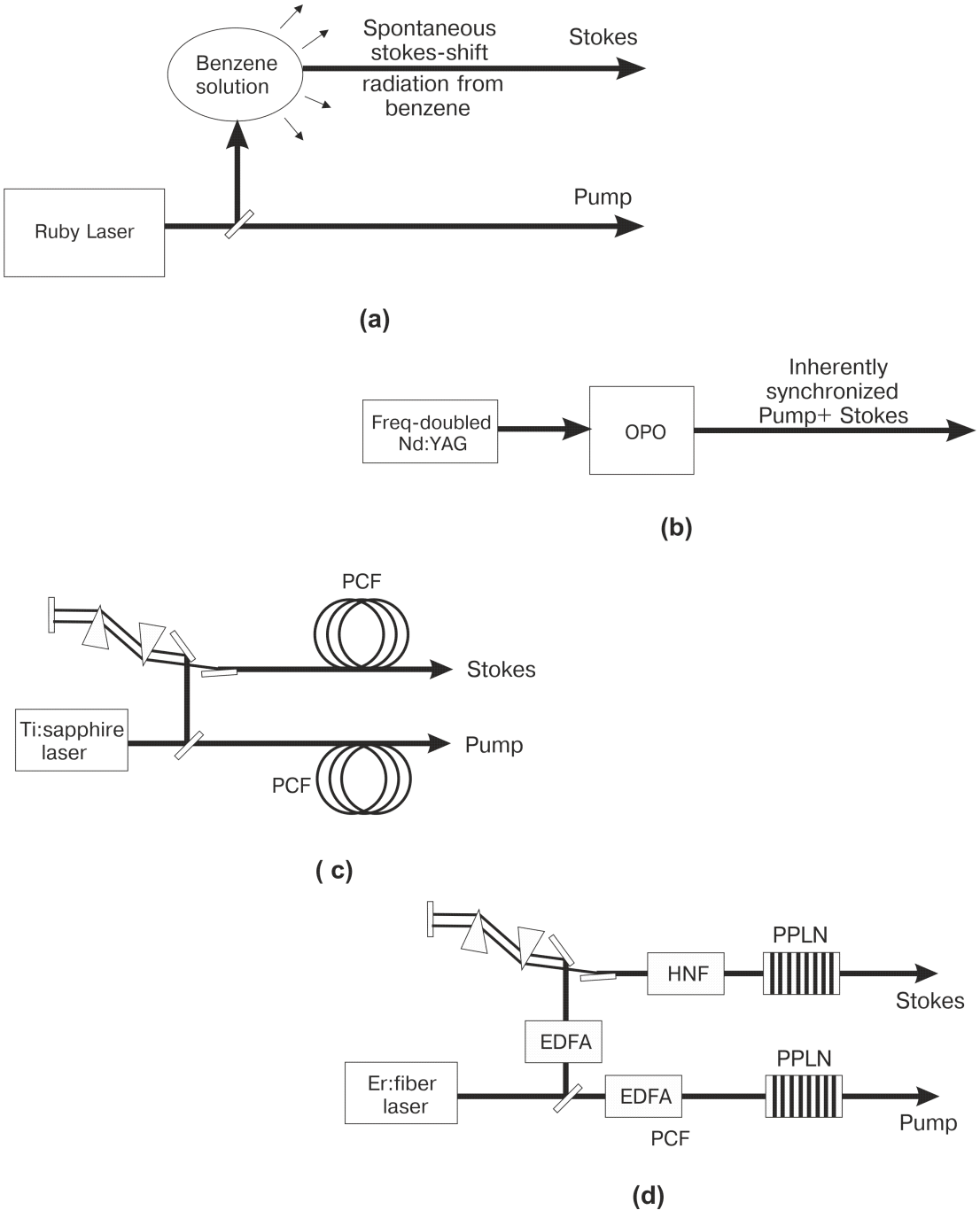


Figure 2.13: Traditional setups for CRS imaging using single laser oscillator.

Ti:sapphire laser oscillator is shown in panel(c) of Figure(2.13). It is a photonic crystal fiber(PCF)-based source generating tunable pump and Stokes pulses. The pump pulse is derived by spectral compression of a part of the laser output in a PCF. The Stokes pulse is generated by red-shifting the rest part of laser output in a PCF through the soliton self-frequency shift[68]. Tunability of Stokes pulses is achieved by a graded neutral density filter providing control over the input power and hence over the red-shift.

All aforementioned light sources are incorporated with free-space lasers. The free-space lasers, in general, are bulky. Simpler robust set-ups can be formed by replacing them by fiber-lasers. A novel fiber-format configuration proposed by our group is shown in panel(d) of Figure(2.13). It utilizes a commercially available, amplified mode-locked Erbium-fiber laser. To derive ps pump pulses, one part of the amplified fs pulses from laser is negatively chirped by using a prism-pair and then is fed to a periodically poled Lithium niobate (PPLN)crystal to synthesize spectrally compressed second harmonic ps pulses with very high conversion efficiency. And to derive tunable Stokes pulses, the rest part of the amplified laser output is also spectrally chirped by silicon prism-pair and then fed to the highly nonlinear fiber (HNF) to generate the octave spanning supercontinuum. And finally this supercontinuum is fed to a fan-out PPLN crystal to obtain tunable ps Stokes pulses.

Laser sources for multiplex CARS:

In multiplex CARS, at least one of the pulse shining the sample should be broadband. One novel configuration for multiplex CARS is recently reported by our group[69]. A sketch of set-up is presented in panel(a) of Figure(2.14), where a fs 1040nm output of an amplified Yb:laser is used to derive both pump and Stokes pulses for multiplex CARS. A small fraction of the output is frequency-doubled (by SHG process) in a long LBO crystal to derive ps pump pulses. The rest part of the output is focused in a thick YAG plate to generate a white light continuum (WLC) spanning approximately two octaves. A portion, 520-630 nm, of it is used as broadband Stokes pulses.

The set-up in panel(d) of Figure(2.13)can easily be transformed to multiplex

CARS set-up by removing the PPLN after the HNF (as shown in panel(b) of Figure(2.14)). Another light source for multiplex CARS is presented in panel(c) of Figure(2.14). It utilizes a Yb-fiber laser at 1033.5 nm. A part of the output of the laser is just amplified in a single mode fiber(SMF) to serve as ps pump and the rest part of the output is amplified and spectrally broadened in a long SMF, then it is temporally compressed by a pair of gratings and sent to PCF to generate fs Stokes pulses by soliton self-frequency sift (SSFS)[70].

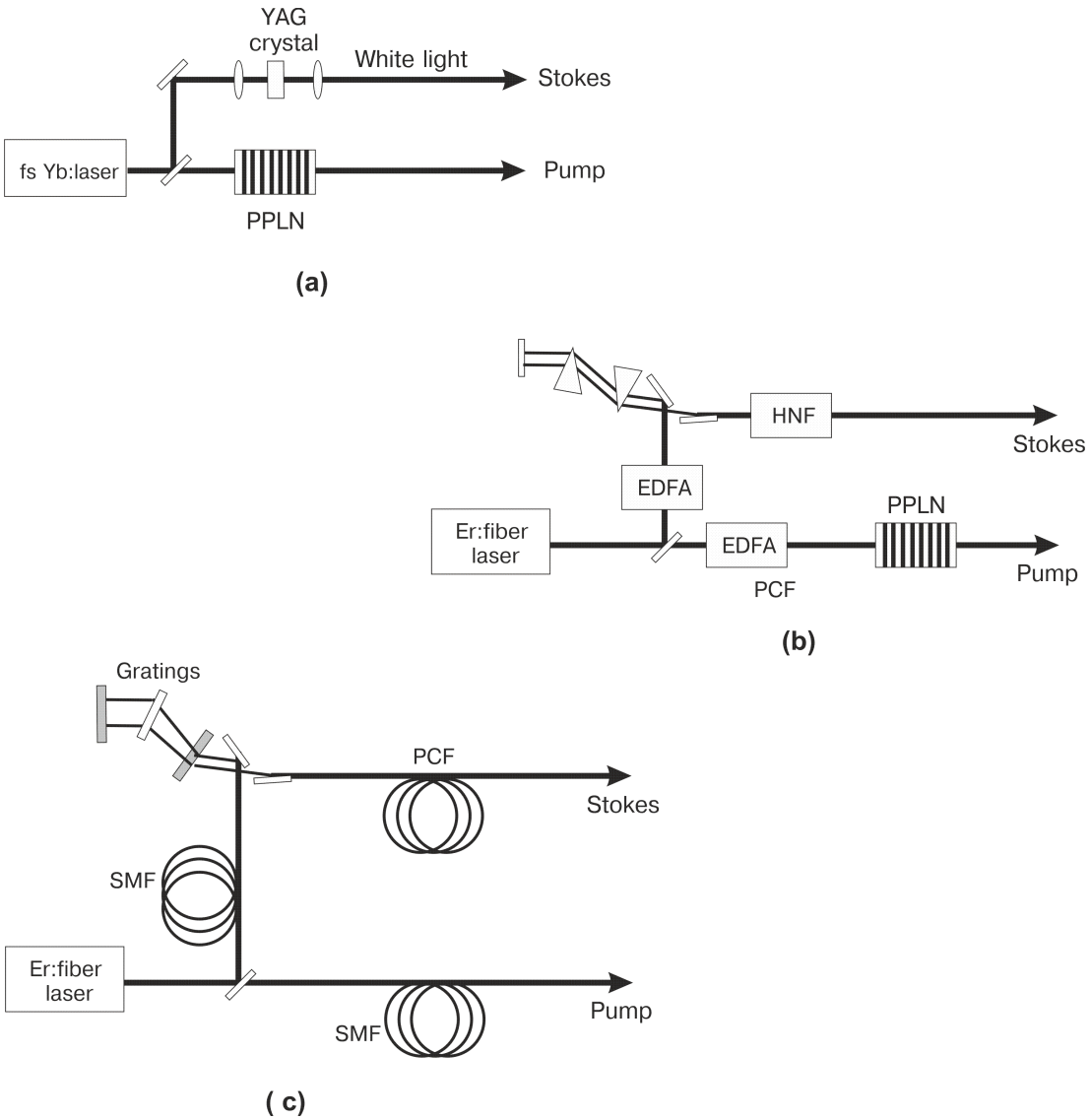


Figure 2.14: Setups for Multiplex CRS imaging using single laser oscillator.

In conclusion, the use of single fiber laser oscillator to derive both the pump and the Stokes pulses, has simplified the set-up. Fiber-format CRS set-ups are

scaled down dramatically from the bulky free-space laser based CRS set-ups. Fiber-laser based systems are reliable and cost-effective in comparison with free-space laser based systems, while their performances are close to the state-of-the-art as the free-space laser based system do.

Chapter 3

Fiber-format CRS microscopy

In this Chapter, we demonstrate a new approach to CRS spectroscopy/microscopy based on spectral compression of femtosecond pulses emitted by a "single" compact Er-fiber oscillator. Spectral compression is achieved by group-velocity mismatched second harmonic generation in periodically-poled nonlinear crystals, and it allows efficient synthesis of synchronized narrow-bandwidth (less than $10cm^{-1}$*) pump and Stokes pulses with frequency difference continuously tunable up to* $3000cm^{-1}$*. Experimental results both on CARS and SRS configurations attest the system performance to be close to the current state-of-the-art. The setup lends itself to the generation of a third synchronized pulse train to implement NRB suppression approaches. Efficient NRB suppression and CARS signal enhancement by up to three orders of magnitude is in particular obtained by interferometric superposition with a phase-coherent local oscillator field, also synthesized by spectral compression. The last Section of the Chapter presents the technical layout and the performances of an upgraded versatile fiber-format CRS setup, which presents the advantage of a higher power level, a lower repetition rate and also an availability of third independent pulse train providing additional degree of flexibility for quick reconfiguration among various kind of CRS microscopy including broadband CARS, FM-CARS, TR-CARS etc.*

3.1 Introduction

The mainstream biomedical applications of CRS are currently hampered by a complex and bulky excitation setup. The required two synchronized trains of

pulses with narrow bandwidth (a few cm^{-1}, corresponding to a few picoseconds pulse duration) and independent tunability over a wide spectral range ($800 - 3300cm^{-1}$), are, as discussed in previous Chapter, typically achieved either by a pair of electronically locked picosecond Ti:sapphire oscillators[64] or by an optical parametric oscillator[71] pumped by a Nd:YVO4 laser. Such solutions do not offer a sufficiently high level of versatility to implement NRB suppression techniques as well as to quickly reconfigure the system on single color to multiple colors for TR-CARS, FM-CARS or for probing multiple lines.

We demonstrate here a new approach for CARS spectroscopy/microscopy, which utilizes femtosecond pulses emitted by a *single* highly compact fiber laser. The required multiple continuously tunable narrowband phase-coherent pulses for CRS spectroscopy/microscopy, are synthesized by spectral compression of these femtosecond pulses. Spectral compression of the broadband femtosecond pulses is achieved by generating narrowband second harmonic (SH) pulses in crystals with large group-delay mismatch between the fundamental frequency (FF) and the SH pulses. Such technique was recently demonstrated by our group to lead to conversion efficiencies in excess of 30% together with compression factors as high as 100[72; 73]. When applied to CRS in combination with fiber-format source, it allows a dramatic improvement of the set-up in terms of compactness, simplicity and, most of all, versatility. Additional possibility of easily synthesizing a third phase-coherent colour to be applied either for FM-CARS or for I-CARS techniques makes the system more interesting for applications.

3.2 Experimental setup

The experimental setup is shown in Figure(3.1). The laser source is a commercial 100 MHz Er-doped fiber oscillator with two fiber amplified branches (Toptica FFS model), each one delivering nearly 70 fs long pulses at 1550 nm with 2.5 nJ energy, resulting in a 250 mW average power. Amplification is done through Erbium-doped fiber amplifiers [EDFA] pumped by diode array from both sides. One of the amplified outputs is spectrally chirped by silicon prism-pair and then is coupled to a highly nonlinear fiber [HNF] producing an octave-spanning supercontinuum

(SC) from 1000 to 2200 nm[74] (the simplified layout of amplified fiber laser is shown within dotted square in Figure(3.1)). The silicon prism-pair provides control over the spectral power density of the supercontinuum.

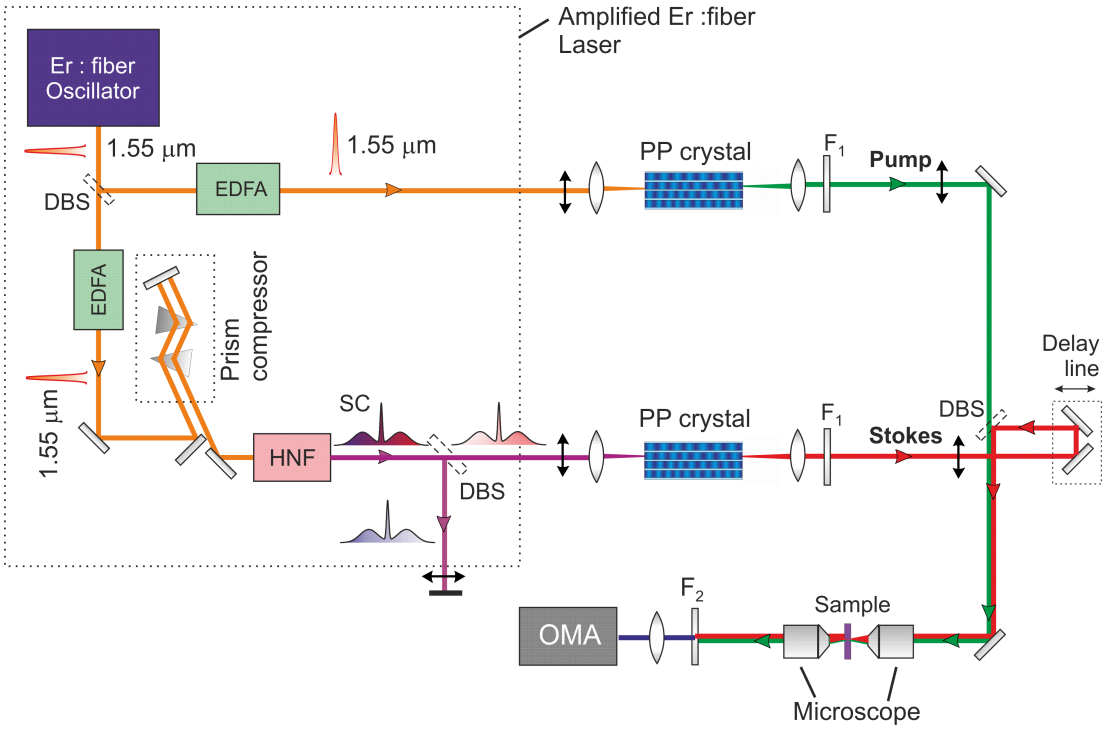


Figure 3.1: Setup for CARS based on multi-color fiber-format amplified Er:Laser (in the dotted rectangle);DBS: dichroic beam splitter; F1: band-pass filter; F2: short/bandpass filters; PP: periodically-poled crystals; SC: supercontinuum; PD: photodetector .

The SC consists of two well distinct bands at opposite positions with respect to the 1550 nm wavelength, each one exhibiting a main spectral peak whose position can be easily tuned by changing the chirp of the pulses entering the nonlinear fiber by silicon prism-pair. Figure(3.2) shows, as dashed lines, the spectrum of the 1550 nm output and a sequence of spectra of the long-wavelength peak of the SC, tunable from 1700 to 2000 nm. The 1550 nm output and the SC, since derived from the same laser oscillator, are phase-coherent. Thus the laser has two inherent phase-coherent outputs, the 1550 nm output and the SC.

Derivation of pump and Stokes pulses

The 1550 nm pulse train is spectrally compressed by tight focusing in a 18-mm long periodically poled lithium niobate (PPLN) crystal to produce narrowband

($< 10cm^{-1}$) **pump** pulses at 775 nm with up to 40 mW average power (solid black line in the Figure(3.2)).

The long-wavelength peak of the SC (red-shifted part) is compressed in a 20-mm PPLN crystal equipped with multiple poling periods, so as to generate narrowband ($< 15cm^{-1}$) **Stokes** pulses with 1-4 mW power and tunability from 800 to 1050 nm, corresponding to a frequency difference between pump and Stokes pulses ranging between 1000 and 3300 cm^{-1} (see solid colored lines in Figure 3.2).

Both PPLN crystals are mounted in ovens to allow for fine frequency tuning (approximately 15 cm^{-1} for a temperature change of 10^0C). The use of periodically-poled crystals for spectral compression is crucial because of:

- the large nonlinear coefficient, allowing for high SHG efficiency.
- the large group-velocity mismatch between FF and SH, allowing for high spectral compression ratios.
- the absence of spatial walk-off between the interacting beams, enabling the

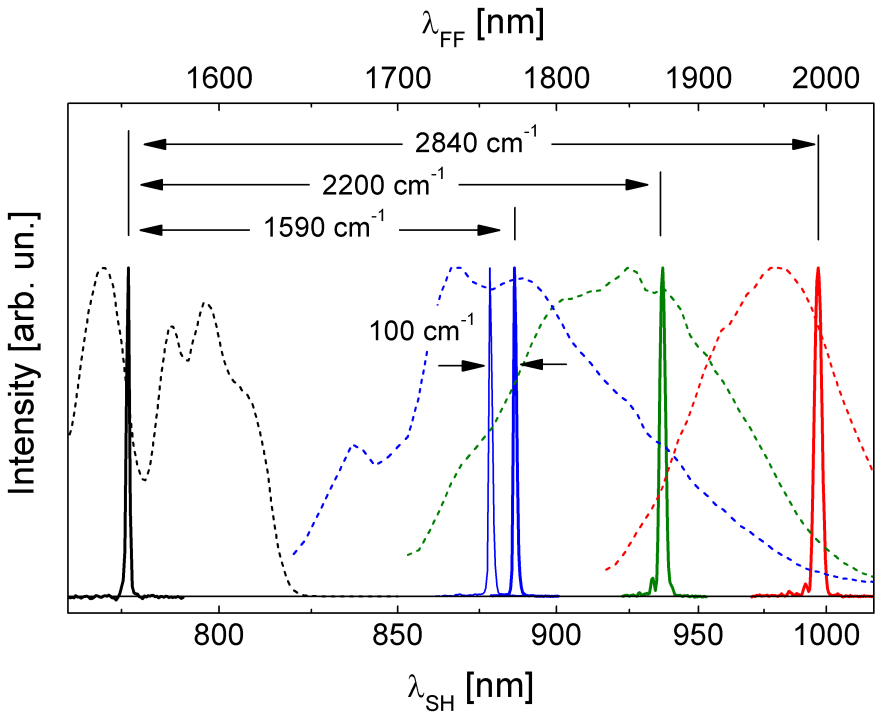


Figure 3.2: Compressed SH spectra (solid lines, bottom scale) and corresponding FF spectra (dashed lines, top scale). The Stokes pulses separated by $100cm^{-1}$ are simultaneously synthesized by splitting the SC in two parts, for application to FM-CARS.

combination of long crystals with tight focusing.

Spectral compression technique: rationale

Several linear and nonlinear techniques have been proposed for the synthesis of tunable picosecond pulses starting from femtosecond pulses. Linear approaches, relying on spectral filtering of the femtosecond pulse with either a bandpass filter[75] or the combination of a slit with a 4f pulse shaper[76], introduce a strong power penalty, by an amount equal at least to the ratio between input and filtered bandwidth. Higher efficiency can be obtained with nonlinear methods. Self-phase-modulation processes in photonic crystal fibers with negatively chirped input pulses allow for compression ratios as high as 10, at the price, however, of poor power scalability and stability[77]. Second order nonlinear processes driven by chirped pulses have also been exploited, such as sum-frequency-generation (SFG) between pulses with opposite chirp[78] or difference-frequency-generation between pulses with the same chirp[79]. These techniques are however experimentally challenging, since they require the use of a pair of carefully balanced gratings (or prisms) pulse stretchers/compressors.

Recent papers[80; 72; 73] showed that a SHG process in the presence of high group-velocity-mismatch between the FF and the SH pulse can lead to the efficient generation of narrowband SH pulses starting from broadband FF ones. This result can be understood by considering that, in addition to the SHG process, there is also an efficient SFG process between spectral components of the FF that are symmetric with respect to the SHG phase-matching frequency, allowing efficient energy transfer from the broadband FF pulse to the narrowband SH one. The process is explained in more detail in Appendix B. To discuss the choice of the spectral compression crystal it is worth reminding that the FWHM bandwidth of the SH pulse, $\Delta\nu_{SH}$, is approximately given by $\Delta\nu_{SH} = 0.886\frac{1}{|\delta|L}$,where L is the crystal length and $\delta = \frac{1}{\nu_{gFF}} - \frac{1}{\nu_{gSH}}$ is the temporal walk-off per unit length[81], ν_{gFF} andν_{gSH} being the group velocities at the two frequencies. To achieve large compression ratios one thus requires long crystals and large values of $|\delta|$. Periodically poled crystals are the best choice possessing these properties.

3.3 CARS Experiments

Pump and Stokes are synchronized by a delay line, combined by a dichroic beam splitter [DBS] and focused on the sample by a microscope objective. Then, a set of short-pass and band-pass filters selects the forward CARS signal, with a rejection of 10^{13} on the pump and the Stokes beams.

We tested our system on a solution of dimethyl sulfoxide (DMSO). Figure(3.3) shows the CARS intensity as a function of the frequency difference $\omega_p - \omega_s$ when varied from 2800 to 3000 cm^{-1} by temperature and poling-period tuning. We observe the typical asymmetric dispersive shape of the CARS response, with a strong peak at 2890 cm^{-1} and a less intense one at 2972 cm^{-1}. The narrow width of the main peak (15.5 cm^{-1}) gives proof of the high spectral resolution of the apparatus. The solid line in Figure(3.3) shows a fit to the measured CARS signal using the response $I_{cars} \propto |\chi^{(3)R} + \chi^{(3)NR}_{Re}|^2$ (discussed in equation 2.7b) where $\chi^{(3)R}$ is the resonant CARS signal, consisting of two Lorentzian resonances, and $\chi^{(3)NR}_{Re}$ is the non-resonant part.

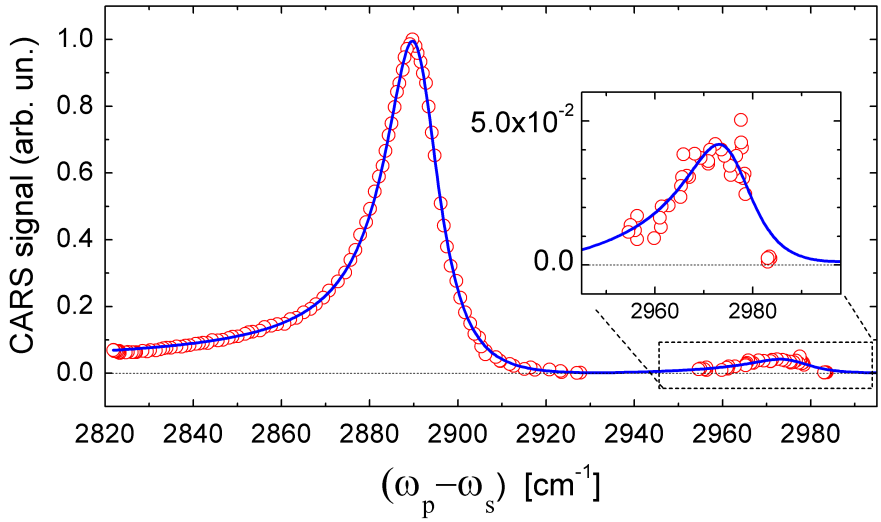


Figure 3.3: CARS signal as a function of the frequency detuning between pump and Stokes for a solution of DMSO..

Figure (3.4) shows the dependence of the CARS signal on the average pump and Stokes powers: by using a bilogarithmic scale: the experimental data are well fitted by linear fitting curves with 2.02 and 1.11 slopes for pump and Stokes respectively, which is consistent with the expected quadratic and linear depen-

dencies from theoretical arguments discussed in Chapter 2.

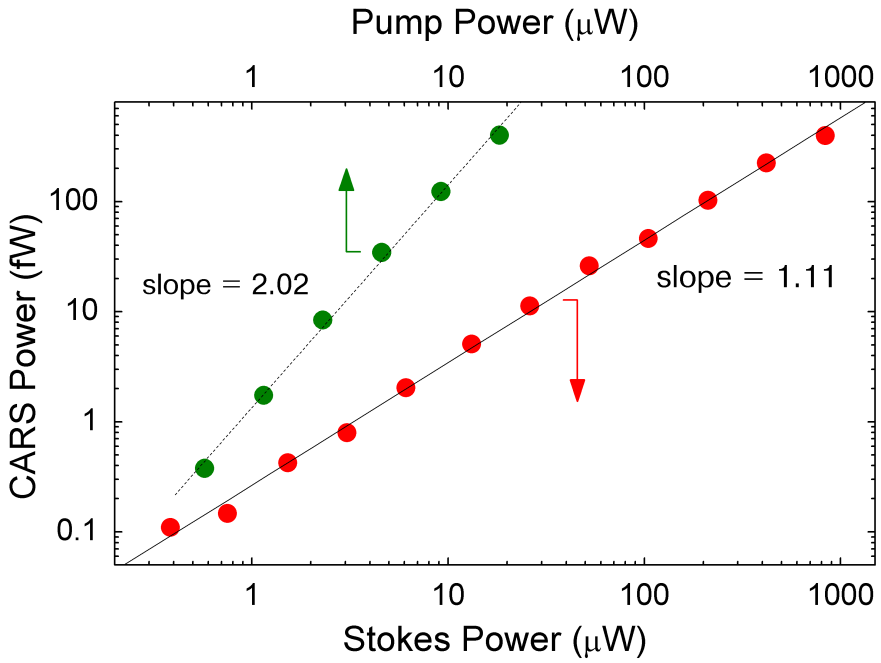


Figure 3.4: CARS power at the peak of the DMSO response as a function of pump and Stokes powers: experimental points (dots) and power law fitting curves (lines).

The above results demonstrate the feasibility of a fiber-format laser system for CARS spectroscopy. The next paragraph illustrates how one can take advantage of this laser source in implementing a NRB suppression technique for CARS.

3.4 Experiment on Interferometric-CARS

The laser system offers a unique flexibility to split straightforward the SC beam and generate two Stokes pulses with frequency offset of 100 cm^{-1} (the two blue solid line spectra in Figure3.2) to be focused alternatively on the sample for FM-CARS, or a third narrowband phase-coherent pulse at the anti-Stokes frequency to be used as a local oscillator for I-CARS.

We tested Interferometric-CARS configuration by introducing in the Stokes branch a dichroic beam-splitter reflecting the short-wavelength part of the SC and sending it to a third PPLN crystal for the synthesis of the narrowband pulse at ω_{as} The entire setup for I-CARS is reported in Figure(3.5). Since the SC generation process was optimized to maximize the Stokes pulse generation,

a fairly low power of few μWs was achieved by frequency doubling the short-wavelength part of the SC. A much higher power level could be obtained by using an oscillator with three amplified branches and a pair of nonlinear fibers giving optimized SC spectra both for the Stokes and for the pulses at anti-Stokes frequency. Thanks to the phase-coherence between pump, Stokes and the pulses at anti-Stokes frequency, which is ensured by the common driving laser oscillator. The anti-Stokes field, when temporally and spatially overlapped with the other two fields, can be used as local oscillator [LO] for homodyne amplification of the CARS signal, according to the well known interference formula

$$S = P_{CARS} + P_{LO} + 2\sqrt{P_{CARS}P_{LO}}\cos\phi \tag{3.1}$$

where P_{CARS} is the CARS signal and ϕ is the phase difference between LO and CARS signals.

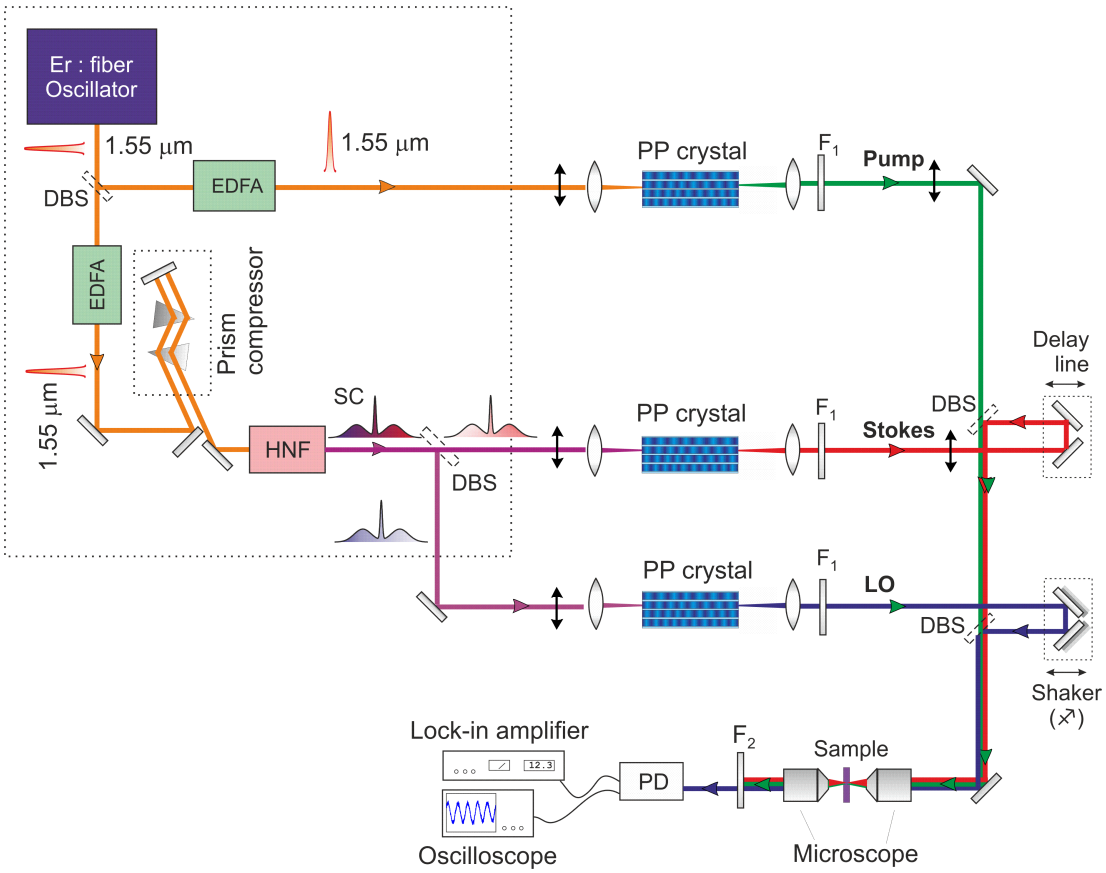
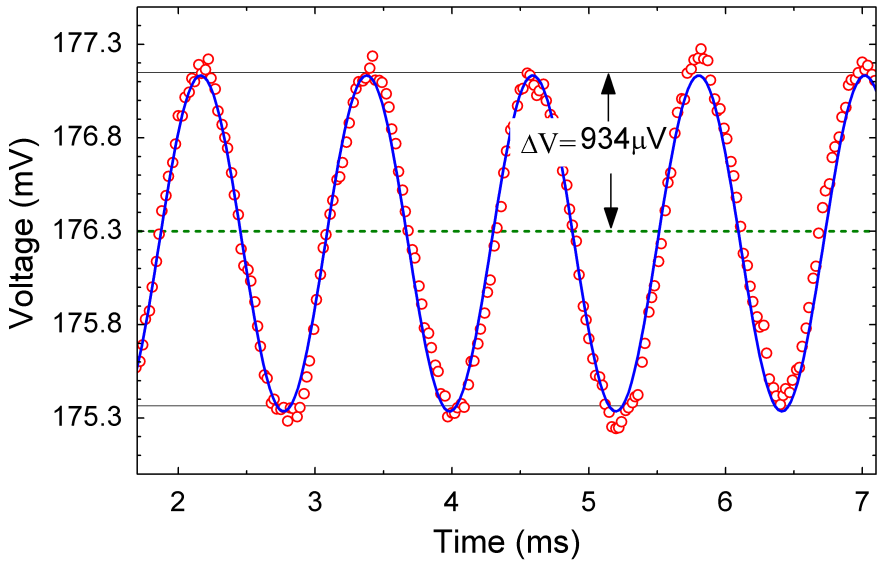


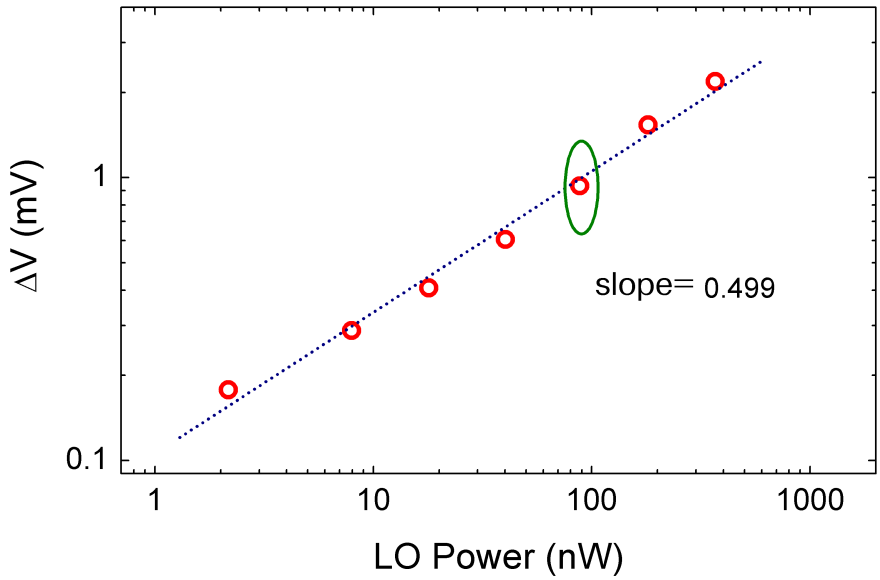
Figure 3.5: Experimental setup for Interferometric-CARS.

As a first phase-coherence test, we have tuned pump-Stokes frequency differ-

ence to the peak of the DMSO response,and attenuated the LO beam by ≈six orders of magnitude to bring it to the same power level of the CARS signal (≈ 1pW), and sent both signals to a spectrometer. According to the value of ϕ a constructive interference up to 3.7 P_{CARS} (and destructive down to 0.3 P_{CARS}) was observed. This gives experimental evidence of the phase coherence between CARS and LO beams, the only limitation coming from imperfect temporal and spatial matching.



(a) *Interference pattern between CARS and LO as a function of their delay.*



(b) *Modulation amplitude (ΔV) as a function of LO power: experimental points (dots) and power law fitting curve (lines).*

Figure 3.6: Interferometric CARS from DMSO.

As a second step we increased the LO power to the μW level and detected with a photodiode the beating signal resulting from periodic modulation of ϕ, as achieved using a shaker on the LO beam path. This allows to visualize the interference term in Equation (3.1) and obtain an amplification of the CARS signal by a factor of $2\sqrt{P_{LO}/P_{CARS}}$, as high as 2000 for a LO power of 1 μW. Figure(3.6a) shows the interference pattern acquired with an oscilloscope for a LO power of $50nW$: the modulation depth with respect to the continuous level given by the LO is of $\pm 0.5\%$, which is consistent with the expected optical power ratio ($\pm 250pW$ over $50nW$) given by Equation(3.1). Figure (3.6b) shows as dots the amplitude of the homodyne interference term as a function of the LO power; a power law fit (dashed line) yields a slope of 0.49, in agreement with the expected square root dependence.

Writing equation (3.1) in terms of corresponding intensities:

$$S = I_{CARS} + I_{LO} + 2\sqrt{I_{CARS} I_{LO}} \cos\phi \tag{3.2}$$

And introducing expression of intensity of CARS I_{CARS} from equation(2.14), above equation will transform as:

$$S = I_{CARS} + I_{LO} + 2\sqrt{I_{(p^2s)} I_{LO}}(\chi_{Re}^{(3)R} + i\chi_{Im}^{(3)R} + \chi_{Re}^{(3)NR}) \cos\phi \tag{3.3a}$$

$$= I_{CARS} + I_{LO} + 2\sqrt{I_{(p^2s)} I_{LO}}[(\chi_{Re}^{(3)R} + \chi_{Re}^{(3)NR}) \cos\phi + \chi_{Im}^{(3)R} \sin\phi \tag{3.3b}$$

The equation(3.3b) derived from equation(3.1) is identical to equation(2.15c) for I-CARS. In the experiment, by justifying the consistency with equation(3.1), we have proven that the system is able to provide a phase-coherent LO for I-CARS. We have experimentally verified that amplification of the CARS signal is possible by taking advantage of this phase-coherent LO.

3.5 SRS Experiments

For SRS experiments, the same pump and Stokes pulses, those are used in normal CARS experiment, are temporally overlapped through a delay-line, combined on a dichroic beam splitter for spatial overlap and focused on a sample through a microscope objective (60X, NA=0.7). The transmitted Stokes beam after being

collimated by a long-working-distance condenser (100X, NA=0.75) is being filtered from the pump by a sequence of long-pass and band-pass filters and send to a balanced silicon photodiode (Nirvana 2007,New Focus). The experimental layout is shown in Figure(3.7).

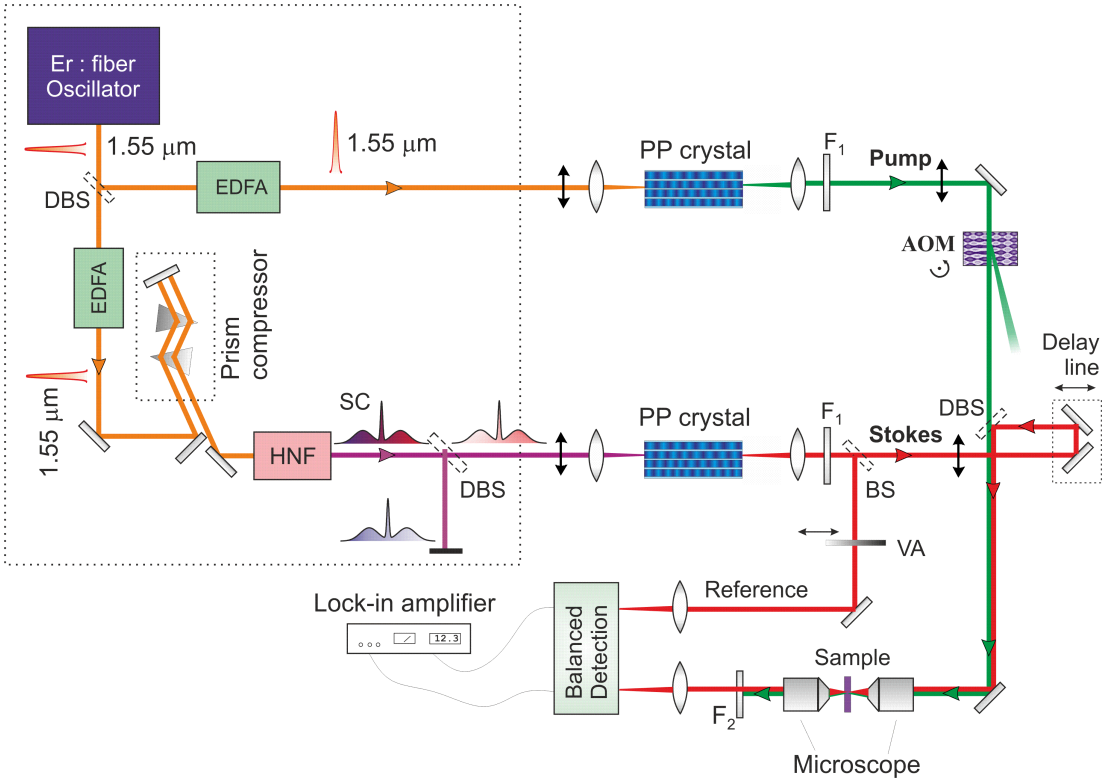


Figure 3.7: Experimental setup for fiber-format SRS microscope. DBS: dichroic beam splitter; BS: beam splitter; F1: band-pass filter; F2: short/bandpass filters; PP: periodically-poled crystals; SC: supercontinuum; VA: variable attenuator.

A fraction of the Stokes beam is spit off before the dichroic beam splitter and focused on the second photodiode of the balanced silicon detector to serve as a reference. The pump beam is modulated acousto-optically at a 40 kHz frequency, corresponding to a relative minimum of the noise spectral density of the Er-fiber oscillator [-118 dBc/Hz](Figure3.8), and the SRG of the Stokes is measured by a lock-in amplifier.

Balanced detection largely cancels the Stokes intensity fluctuations and allows one to achieve a sensitivity down to 2×10^{-7} over 500 ms integration time. The samples are mounted on a three-dimensional linearized piezoelectric stage that is raster scanned for imaging in the focal plane. Difference frequency $\omega_p - \omega_s$ is

tuned for a particular molecule in the sample and SRG signal (lock-in reading) is recorded pixel-by-pixel to obtain the SRS image of the sample.

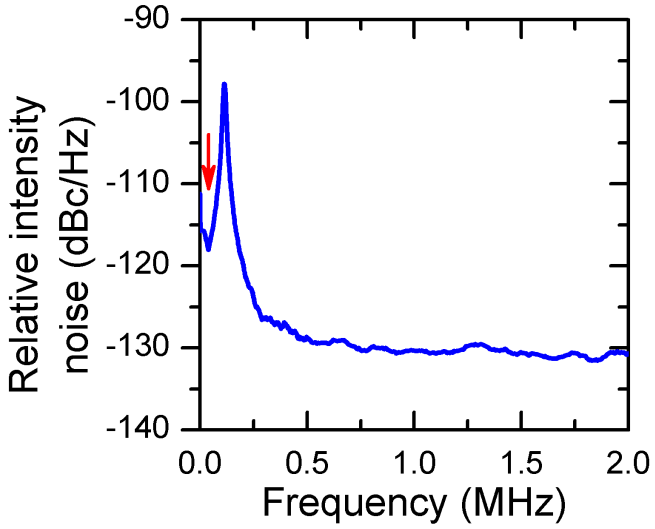


Figure 3.8: Intensity noise spectrum of the laser.

To compare the CARS and SRS spectra from the system, we took the SRG spectra of dimethyl sulfoxide (DMSO) solution through lock-in detection by modulating the pump beam and varying the Stokes frequency by temperature tuning of the PPLN crystal in the Stokes arm. Figure (3.9) shows the SRG spectra of DMSO as a function of the frequency difference $\omega_p - \omega_s$ obtained in this way. The time required for a 200 cm^{-1} scan was about 1 minute, but much higher speed would be obtainable with dedicated PPLN crystals with fanout structure. We observe two well-resolved peaks at 2910 cm^{-1} and 2990 cm^{-1}, in very good agreement with the spontaneous Raman spectrum of DMSO, with a signal-to-noise ratio as high as 300. This measurement demonstrates the high sensitivity and spectral resolution of the setup.

We have also checked for the pump intensity dependence on the SRG signal from DMSO solution. For this purpose, pump power is varied though a variable attenuator and corresponding SRG signal is recorded. The inset of Figure (3.9) shows in a bilogarithmic scale the pump intensity dependence of the SRG signal together with a linear fitting curve: its slope is very close to 1, thus confirming the expected linear behavior discussed in equation (2.22e).

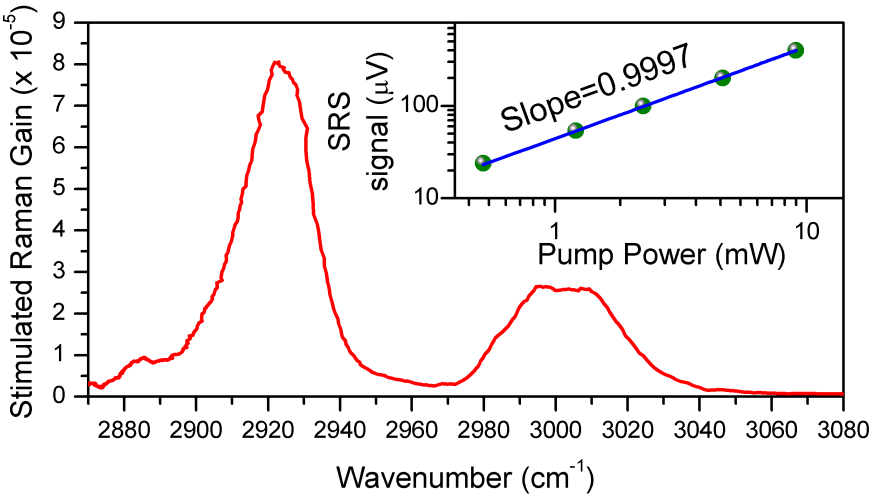


Figure 3.9: SRS spectrum of DMSO. Inset: pump-power dependence of the SRS signal.

We tested the imaging capabilities of this SRS microscope on thin films of poly(9,9-dioctylfluorene)(PFO), blended with polymethylmethacrylate (PMMA, 10% wt. PFO in PMMA). As it is commonly the case in polymer blends, a phase segregation occurs between PFO and the host matrix, with a large distribution of domain sizes ranging from submicrometers to hundreds of micrometers. PFO and PMMA present their strongest Raman resonances at very different frequencies, 1590 and 2950 cm^{-1}, respectively, with negligible overlap between them. This makes it possible to distinguish the two compounds by probing either the PFO resonance or the PMMA one. We experimentally verified this fact by acquiring two images of the same sample area with the two frequency detuning values. With a pixel dwell time of 10 ms, limited by the speed of the piezoelectric scanner stage, the results are shown in Figures(3.10(a) and (b)).

The images clearly give the same information content, the former one being the positive version of the latter one: PFO organizes itself in nearly circular spots with diameters of a few micrometers in the scanned region. The spatial resolution is better than 600 nm, which is a satisfactory result in view of biological applications, and it could be improved by using oil immersion objectives. Figure (3.10c) shows the SRS spectrum of PFO as acquired by tuning the Stokes frequency around resonance with power levels of 10 mW for the pump and 1 mW for the Stokes. The peak is remarkably narrow, $\sim 20\ cm^{-1}$, thus confirming high spectral resolution.

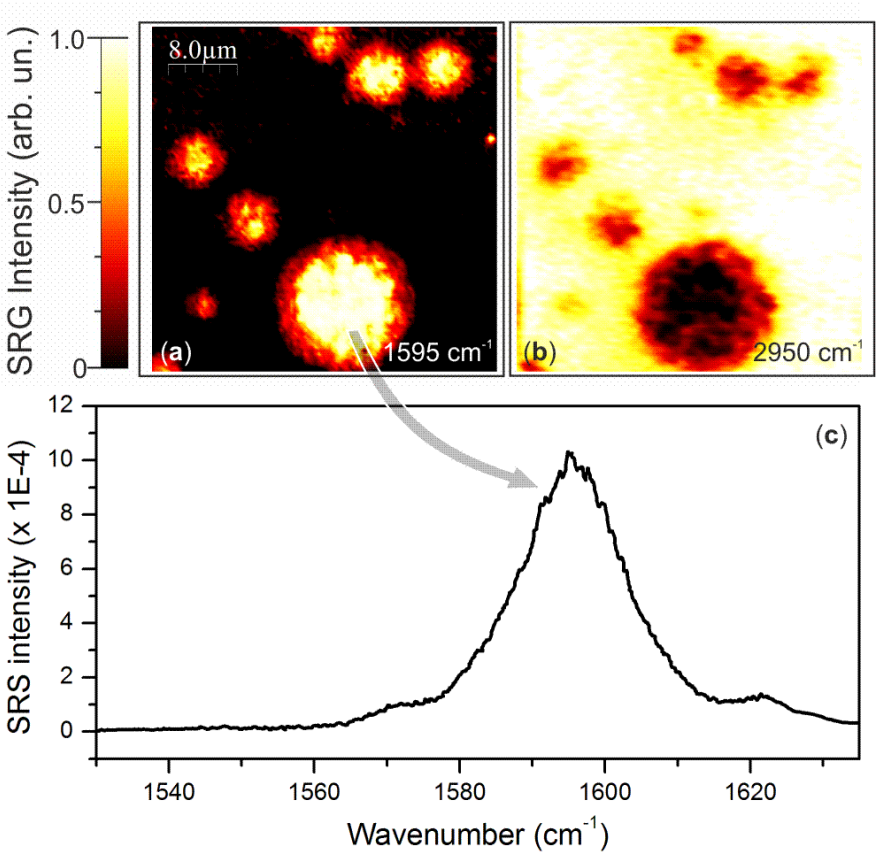


Figure 3.10: SRS image of a blend of PFO in PMMA at (a) 1590 cm^{-1} ,(b) 2950 cm^{-1}, (c) SRS spectrum acquired on a PFO domain.

In conclusion, with results from this system we have presented a new concept for the generation of tunable, synchronized narrowband pulses starting from a single fiber-format femtosecond oscillator, which promises a dramatic simplification of the architecture of the driving laser for coherent vibrational microscopy. Several improvements of the system are possible: higher pump and Stokes peak powers can be generated by decreasing the repetition rate of the oscillator; higher Stokes pulse energies can be obtained using Raman self-frequency shifted solitons in suitably designed nonlinear fibers giving efficient red-shift to the 1550 nm pulses; rapid continuous frequency tuning can be achieved by using fan-out designs of the PP crystals. Finally, the capability of synthesizing additional phase-coherent multicolour pulses opens a host of opportunities for enhancing the CARS response, by coherent amplification and/or by non-resonant background suppression.

With implementation of these improvements, an upgraded version of fiber-format CRS microscopy setup is developed. In the following Section, the experi-

ments done on this upgraded setup will be presented.

3.6 Upgraded version of the fiber-format CRS microscopy setup

An upgraded version of the previously discussed fiber-format CRS system was developed possessing added advantages of having three independent amplified branches, a higher power level and a lower repetition rate. The upgraded version is, thus, equipped with the flexibility that the third beam can be employed either for the simultaneous detection of multiple molecular species, and/or for the implementation of NRB suppression techniques in CARS. This makes the system a versatile compact tool which can be easily reconfigured for various CRS microscopy techniques. Provided the microscope objectives with near-infrared antireflection-coating are used, the power levels, i.e. $\sim 100mW$ for the pump and $\sim 10mW$ for the Stokes at 40 MHz repetition frequency, are available. Optionally, by exploiting the inherently broad bandwidth of the laser pulses and supercontinuum generation processes in a highly nonlinear fiber (HNF), broadband Stokes pulses can be synthesized, giving access to a multiplex CRS regime in which a wealth of molecular signatures can be addressed at once.

3.6.1 Experimental setup

The architecture of the femtosecond laser system (FemtoFiber pro, from Toptica Photonics) driving our CARS/SRS setup is shown in Figure(3.11).

It starts with a mode-locked Er:fiber oscillator, with linear cavity and semiconductor saturable absorber mirror, working at 40 MHz repetition rate. The oscillator output is used to feed three independent Er-doped fiber amplifiers (EDFAs), each producing 350 mW average power, corresponding to $\sim 9nJ$ per pulse, at a 1560 nm central wavelength. All three EDFA outputs, which are synchronized and phase-coherent, are compressed to nearly transform-limited sub-100-fs duration by a silicon prism pair. Two of the EDFA outputs are coupled to a highly nonlinear fiber (HNF) for spectral broadening. The HNF (3.7 μm core diameter, $\sim$ 7 cm length) has a zero dispersion wavelength which is close to,

but slightly shorter than, the input laser wavelength. The pulses propagating in the anomalous dispersion regime undergo considerable spectral broadening, with the spectral energy density concentrating in two peaks on opposite sides of the input wavelength. At longer wavelengths, the pulse gives rise to a soliton, which experiences self-frequency shift due to intrapulse Raman scattering. The soliton is accompanied by a phase-matched dispersive wave at shorter wavelengths, propagating in the normal dispersion regime. The exact positions of the peaks of soliton and dispersive wave sensitively depend on the overall dispersion of the input pulse, which can be controlled by acting on the silicon prism pair insertion. It is thus possible to continuously tune the soliton peak between 1700 and 2100 nm and to push the dispersive wave to wavelengths as short as 1000 nm.

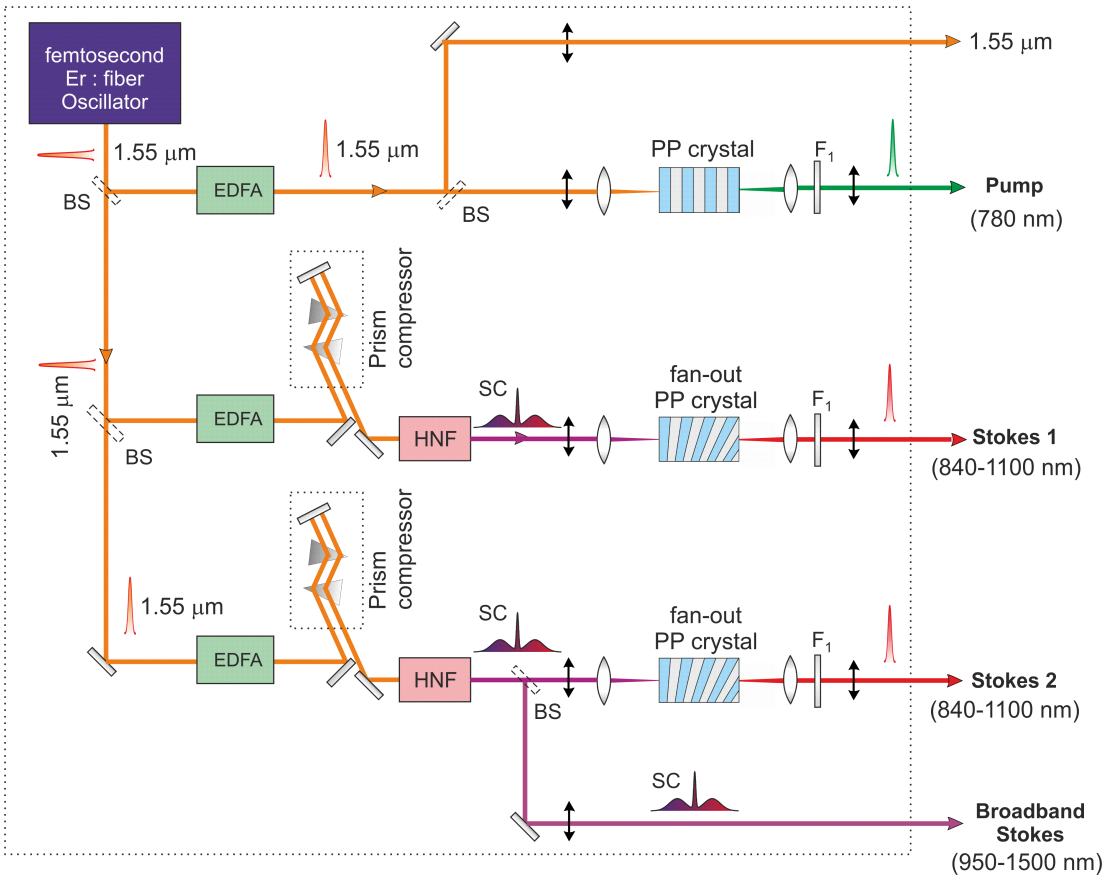


Figure 3.11: Architecture of the adopted laser system, driven by an Er:fiber oscillator. BS: beam-splitter; EDFA: Er-doped fiber amplifier; HNF: highly nonlinear fiber, PP: periodically-poled.

Synthesis of pump and Stokes fields

The system makes use of two distinct MgO-doped periodically poled lithium niobate (PPLN) crystals to generate the pump and the Stokes pulses according to the spectral compression technique described before. The 1560-nm output of the EDFA is compressed by a 10-mm long PPLN with a poling period of 19.3 m and generates the pump pulses at a fixed wavelength of 780 nm, with a 120 mW average power and a 15 cm^{-1} linewidth (see spectrum in the Fig(3.12)). The red-shifted soliton is frequency doubled with a 10-mm long PPLN crystal

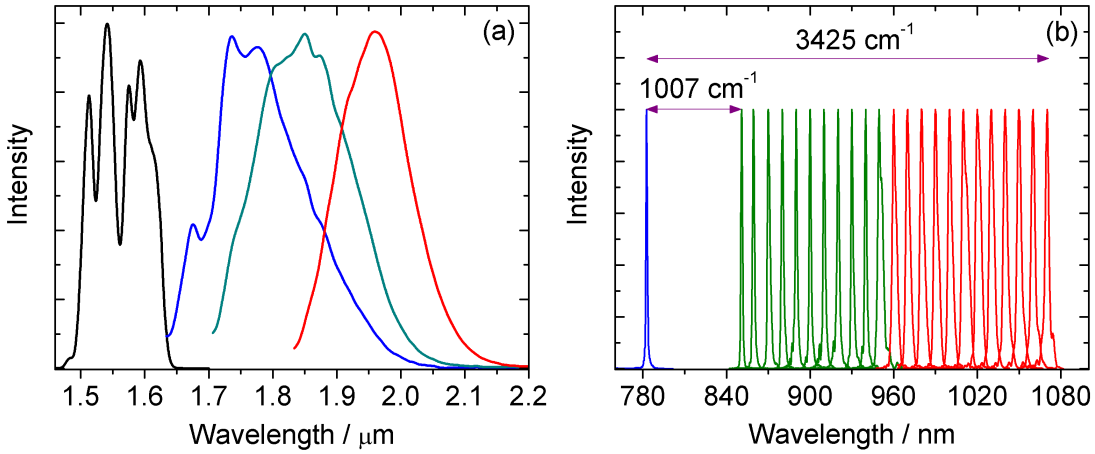


Figure 3.12: (a) Spectrum of the main laser output at 1560 nm (black line) and examples of spectra of the long-wavelength part of the supercontinuum (blue, cyan and red), tunable by acting on the input pulse chirp. (b) Spectra of the pump (green line) and of the tunable Stokes pulse (red lines), as obtained by spectral compression of the spectra reported in panel (a).

having a fan-out grating spanning the 22-33 μm range and it produces Stokes pulses tunable from 840 to 1100 nm with power up to 10 mW, as shown in Figure (3.12(a) and (b)). In this way it is possible to cover a wide range (1000-3500 cm-1) of biologically relevant frequencies with the Stokes pulse. Rapid tuning of the Stokes is achieved by transversely translating the fan-out crystal. Translation is currently performed manually, but the use of a motorized stage could give automatic wavelength selection and reproducibility. The linewidth of the generated Stokes pulses ranges between 18 and 30 cm^{-1}, which is somewhat higher than the data obtained with previous setup. This is due to the use of a shorter crystal and to a slight frequency smearing effect induced by the fan-out

pattern.

3.6.2 CARS and SRS experiments

Pump and Stokes pulses for CARS/ SRS are routed and temporally matched by a delay line, collinearly combined by a dichroic beam splitter (LP02-785RS-25, from Semrock) and focused by a microscope objective (Nikon 60× , NA = 0.80, working distance WD = 3mm) on the sample; the transmitted light is collimated by a long-working-distance objective (Zeiss 100× , NA = 0.75, WD = 3 mm).

For CARS detection, a notch filter (Thorlabs NF785/33) and a band-pass filter (custom-made from CVI) select the forward signal, with an overall rejection of 10^{13} on the pump and Stokes beams.

For SRS detection, the Stokes pulse, filtered from the pump by a sequence of notch filter (Thorlabs NF785/33) and a long-pass filter (Semrock 834/LP), is sent to a balanced InGaAs photodiode (New Focus Nirvana 2017). A fraction of the Stokes beam is split off before the beam splitter and focused on the detector to serve as a reference. The pump beam is modulated acousto-optically at a 70 kHz frequency (APE GmbH AOM-80-D), and a lock-in amplifier (Stanford Research System SR830DSP) measures the SRG of the Stokes. Balanced detection largely cancels probe fluctuations and allows one to achieve a sensitivity down to 5×10^{-7}.

3.6.3 Results and discussion

The spectra of several solvents were acquired in order to test the performances of the system and to compare them with those obtained with a previous dual-branch fiber system, operating at 100 MHz with power levels lower by a factor of ~ 3 for the pump (40 mW) and up to 5 for the Stokes (1 mW at 1000 nm).

Figure (3.13(a) and (b)) shows the spectra both in the CARS and SRS regime when varying the frequency detuning between pump and Stokes by translation of the fan-out PPLN crystal. As expected, the CARS signatures are narrower due to the quadratic dependence on the nonlinear susceptibility, and they are also asymmetrically-shaped due to the NRB contribution. The spectral resolution is currently limited to $\sim 40 cm^{-1}$, but it could be improved with a better design of

the fan-out crystal. On the other hand the new set-up allowed for much higher CARS and SRS signals, due to the combination of a lower repetition rate, higher power level and slightly shorter pulses, resulting in higher peak power.

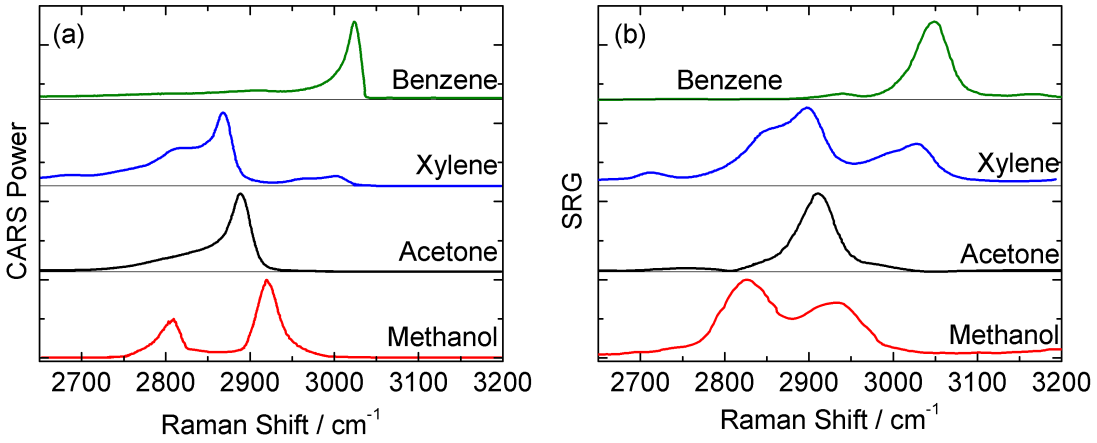


Figure 3.13: (a) CARS and (b) SRS spectra of different solvents.

Simple calculations show in fact that, given the same interaction geometry and sample, the CARS average optical power scales proportionally to $P_p^2 P_s / f_{rep}^2$, while the SRG signal proportionally to P_p / f_{rep} , P_p and P_s being the average power of pump and Stokes, respectively, and f_{rep} the laser repetition rate. The expected signal enhancement is thus as high as 500 for CARS and $\sim$ 10 for SRS, which are values confirmed in the experiments: for methanol, e.g., the CARS average power was in excess of 400 pW and the SRG of the order of 10^{-3}. Concerning SRS, it is worth noting that the advantage given by the signal enhancement was somehow traded off by a higher level of noise, limiting the sensitivity to 5×10^{-7} over 500 ms integration time (2×10^{-7} with the previous system): this was due to increased intensity fluctuations in the supercontinuum, which were not perfectly canceled by the balanced detection system.

Figure (3.14) shows the results of a dilution test of acetone in water down to a 0.1% volume concentration value, both in the CARS and SRS configuration. As expected the CARS signal decreases quadratically, but it quite quickly reaches a constant value due to the strong NRB contribution given from water, limiting the sensitivity to 10 % volume concentration.

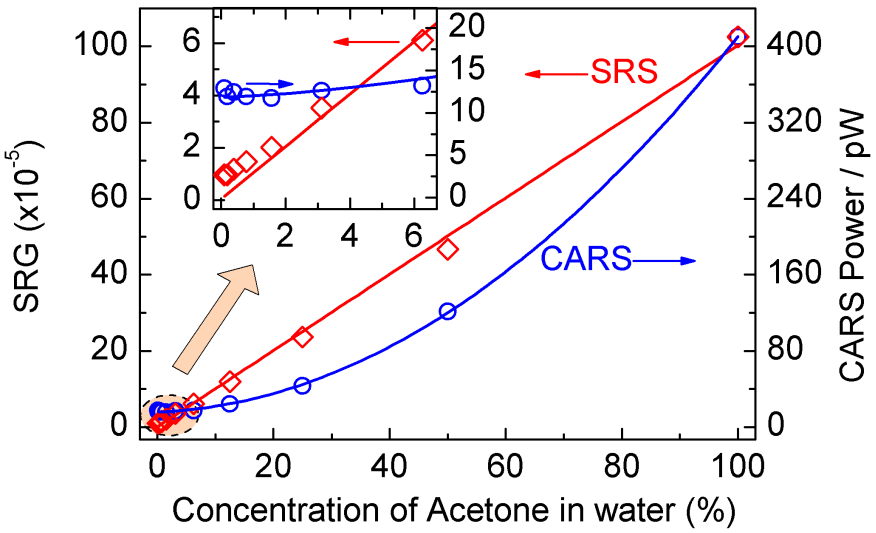
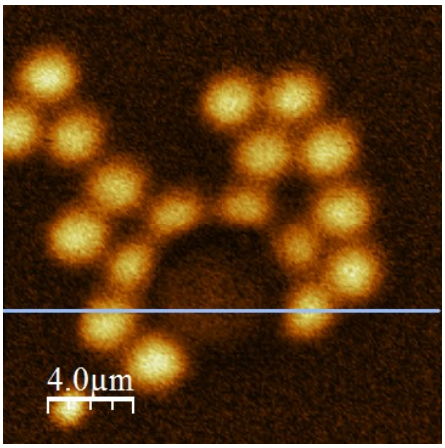
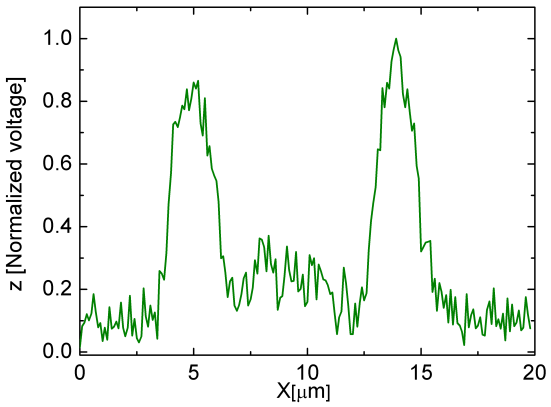


Figure 3.14: Dilution curves of acetone in water measured with CARS (blue circles) and SRS (red diamonds) when tuned to the peak of the aliphatic CH stretching vibration, together with quadratic and linear fitting curves, respectively. Inset shows a zoom for low acetone concentration. Pump power was $\sim 50mW$, Stokes power was $\sim 5mW$.

Differently, as evidenced in the inset of Figure (3.14), the linear SRS response allows the detection of lower concentrations, down to 0.5%, as limited by the undesired resonant response of water, which extends down to the 2910 cm^{-1} pump-Stokes detuning adopted in the experiments.



(a) *SRS image a sample containing 3 micron polystyrene beads and 6 micron PMMA beads, where pump-Stokes frequency detuning is set for Polystyrene vibrational resonance frequency.*



(b) *Intensity profile across a line on image.*

Figure 3.15: SRS image of a sample containing 3-micron polystyrene beads and 6-micron PMMA beads.

The upgraded version of CRS microscope was tested for SRS imaging of a sample containing both the 3-micron polystyrene(PS) beads and the 6-micron PMMA beads where pump-Stokes frequency detuning was set for polystyrene vibrational resonance. Figure(3.15a) shows the acquired SRS image of PS beads. In the image there is no SRS signal from the position of the PMMA bead which demonstrates the chemical selectivity of the microscope. Figure(3.15b) plots the intensity profile across a line on SRS image which is in good agreement with respect to 3 micron size of the PS beads considering SRS signal originating from their spherical shapes.

3.6.4 Key features offered by the third amplified branch

Besides higher average power and energy levels, the new system presents another advantage with respect to the previously adopted dual-branch system at 100 MHz, which is the presence of a third amplified arm whose architecture and performance essentially replicate those of the second arm. The only difference concerns the possibility of easily reconfiguring its output either as a broadband Stokes beam spanning the 950-1050 nm range, or as a second narrowband Stokes beam with tunability from 840 to 1100 nm (Figure (3.16)), or as a phase-coherent beam at the anti-Stokes frequency for I-CARS. Such arm adds considerable flexibility to the system as it provides an additional pulse, synchronized with the first two, which can be employed to implement different CRS configurations.

In the most straightforward setup the third arm is used to generate by spectral compression a second, independently tunable Stokes pulse, which can be applied to two-colour CARS/SRS microscopy. This is shown in panel(a) of Figure(3.16), in which the second arm generates a Stokes pulse at $\sim$ 890 nm, while the third arm, equipped with a PPLN crystal, generates a second Stokes pulse at $\sim$ 1020 nm. With this setup it becomes possible to have simultaneous imaging in the fingerprint and the C-H stretching regions, in a much simpler fashion with respect to previous attempts using a pair of synchronized OPOs.

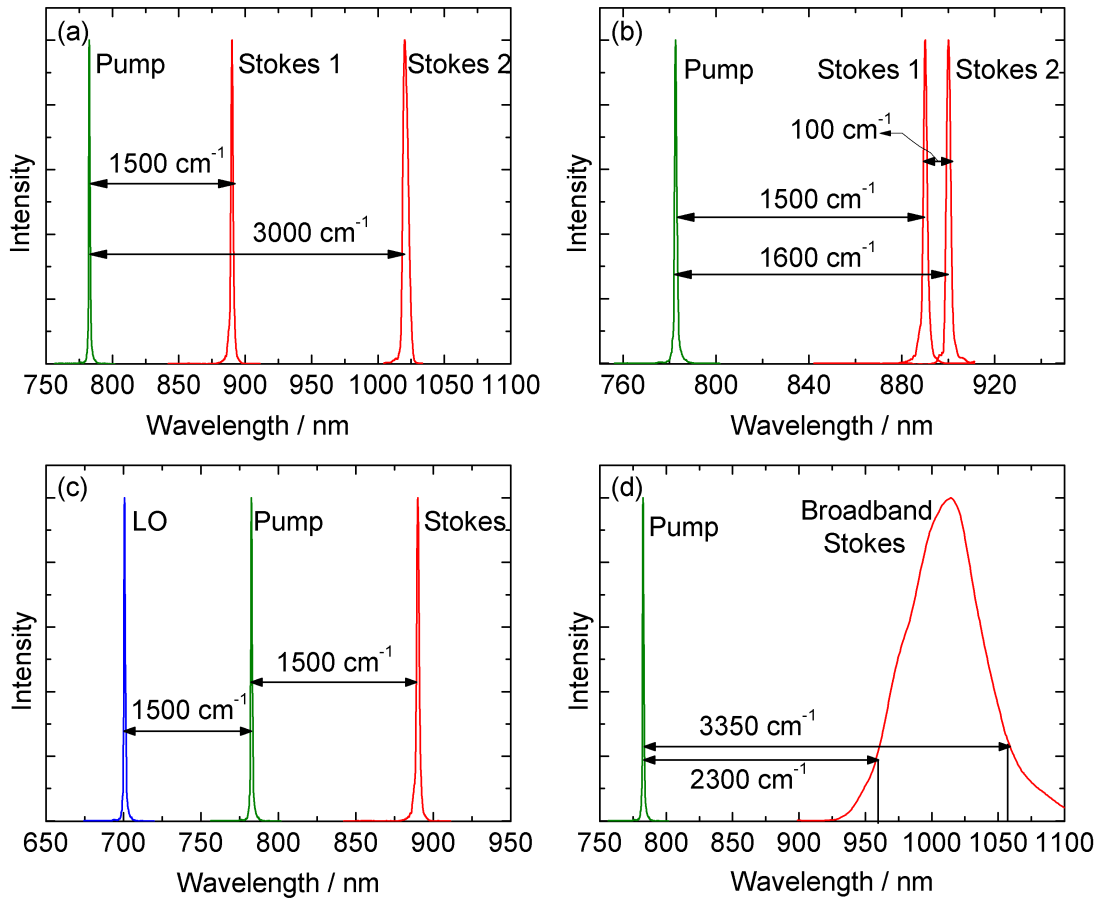


Figure 3.16: Applications of the third arm: (a) synthesis of two Stokes pulses for two-color imaging; (b) synthesis of two frequency separated Stokes pulses for FM-CARS; (c) synthesis of a local oscillator for I-CARS; (d) synthesis of a broadband Stokes pulse for multiplex CARS.

The third arm also enables the straightforward implementation of NRB suppression approaches, such as FM-CARS and I-CARS. For FM-CARS the third arm can be used to generate a second, slightly detuned (by $\sim 100 cm^{-1}$) Stokes pulse [panel(b) of Figure(3.16)], which is alternated with the on-resonance Stokes pulse.

For I-CARS the third arm can be employed to generate a local oscillator (LO) pulse at the anti-Stokes frequency [panel(c) of Figure(3.16)] by SHG of the blue-shifted dispersive wave. The phase coherence between LO and CARS signal is ensured by the fact that pump, Stokes and LO pulses are all derived from the same laser oscillator.

Finally, the third arm can also be used to implement multiplex CARS schemes by taking advantage of the inherently broadband pulses generated by the HNF.

Multiplex CARS uses two synchronized pulses, a narrowband (typically 10 cm^{-1}) pump, providing spectral resolution, and a broadband Stokes pulse, enabling the detection of a complete vibrational spectrum without wavelength tuning. Current state-of-the-art systems for broadband CARS start from a Ti:sapphire oscillator, with the pump pulse generated by spectral filtering and the Stokes obtained by supercontinuum generation in a photonic crystal fiber. In our setup the broadband Stokes is provided by the dispersive wave centered at 1000 nm [panel(d) of Figure(3.16)], which is sufficiently broad to cover all vibrational signatures lying in the C-H stretching region and carries a considerable power spectral density of 0.2 mW/nm. As a preliminary demonstration of this scheme we first acquired a broadband CARS spectrum of cyclohexane [Figure(3.17)].

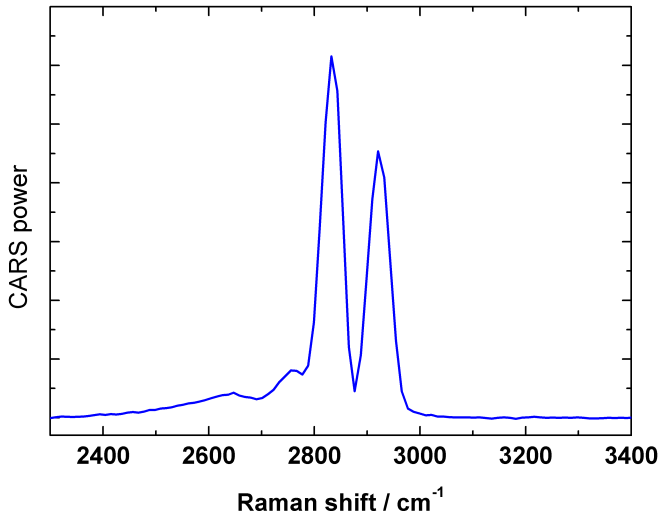


Figure 3.17: Multiplex CARS spectrum of cyclohexane acquired with the broadband Stokes pulse shown in Figure[3.16(d)]. Pump power was 50 mW, Stokes power was 10 mW, and the integration time was 3 ms..

Then we collected broadband spectra of several other solutions[Figure(3.18)]. We are able to resolve even congested peaks of Isopropanol and Toluene. An input pump power of 50 mW, a Stokes power level of 10 mW, and an integration time of 3 ms were sufficient to saturate a standard optical multichannel analyzer (Ocean Optics HR 2000). The system, when coupled to more sophisticated spectrometers, holds a great potential for quick acquisition of CARS images with a broad spectral coverage.

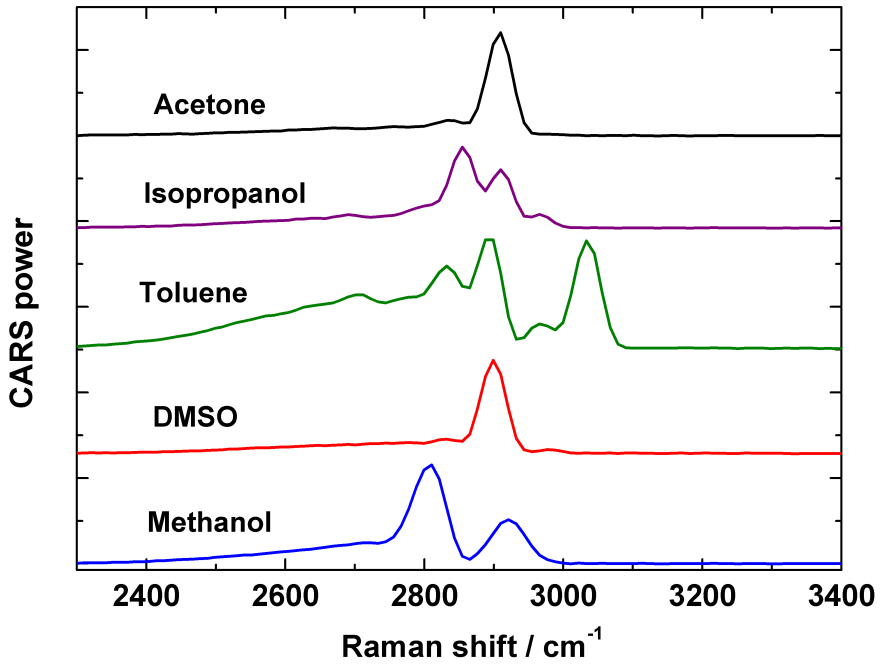


Figure 3.18: Multiplex CARS spectra of several solutions acquired with the broadband Stokes pulse shown in Figure[3.16(d)]. Pump power was 50 mW, Stokes power was 10 mW, and the integration time was 3 ms..

3.6.5 Conclusions

The new fiber laser system for coherent Raman imaging, both in the CARS and SRS configuration, relies on an Er:fiber femtosecond oscillator driving three amplified branches, two of which are coupled to nonlinear fibers giving highly controllable supercontinua tunable over more than one octave. Such broadband femtosecond pulses are converted with high efficiency into narrowband, tunable, picosecond pulses by spectral compression in second-order nonlinear crystals. The system generates pump and Stokes pulses with performances comparable to those of state-of-the-art systems for CARS/SRS, but with advantages in terms of compactness, cost and versatility. In fact the third arm can be quickly configured to provide either a second narrowband Stokes pulse to be used for NRB suppression or two-color imaging, or a broadband Stokes pulse for multiplex CARS. Experimental results, so far limited to spectroscopic tests, are quite promising in view of applications of this new source to mainstream biomedical imaging.

Chapter 4

NRB-free broadband CARS from a powerful ytterbium laser

In this Chapter, we introduce a novel configuration for broadband, time-resolved CARS spectroscopy/microscopy in which pump, Stokes and probe pulses are all derived from a single femtosecond Yb:KYW laser. The 1-MHz repetition rate of the system allows very intense CARS signals to be obtained over short acquisition times, while a delayed probe pulse ensures an efficient non-resonant background suppression.

4.1 Introduction

As we have already discussed in Chapter 1, CARS process can be viewed as the excitation of a sample with two pulses at frequencies ω_p (pump) and ω_s (Stokes), whose difference matches the frequency Ω of a Raman active molecular vibration. The interaction of a third pulse at frequency ω_{pr} (probe) with the vibrational coherence generated by pump and Stokes produces a strong coherent signal at the anti-Stokes frequency, $\omega_{as} = \omega_p - \omega_s + \omega_{pr}$. When probe frequency is same as pump frequency, we call it *degenerate CARS* (which is the normally used CARS configuration) and when probe frequency is different with respect to pump frequency, we call it *non-degenerate CARS*.

We should also recall the fact we have discussed before that in single-frequency CARS all the interacting pulses are narrowband (a few cm^{-1} spectral width) so that the extracted information refers to a specific vibrational frequency. Although

single-frequency CARS allows a very high acquisition speed, enabling imaging up to the video rate, yet it gives only limited information on the molecular system under study. In many cases, the ability to distinguish between the different components within a complex heterogeneous system requires the recording of a full Raman spectrum. Broadband CARS(also called multiplex CARS) uses a narrowband probe pulse, providing spectral resolution, and a broadband Stokes pulse, enabling the detection of a complete vibrational spectrum.

Among the various NRB suppression techniques in the case of broadband CARS, a particularly powerful and elegant approach is time-resolved CARS (TR-CARS), in which the probe pulse is delayed with respect to the pump/Stokes pair by a time Δt which is sufficiently high to avoid any temporal overlap. In such case the NRB generated by the $\omega_{as} = \omega_p - \omega_s + \omega_p$ process, which relies on the instantaneous $\chi^{(3)}_{Re}$ of the medium, is completely suppressed. The price to be payed is that the time-delayed probe pulse interacts with a vibrational coherence that has decayed with dephasing time $T_{2\nu}$, leading to a reduction of the useful CARS signal by $exp(-2t/T_{2\nu})$. As we have already discussed in the previous Chapter that TR-CARS requires a three-colour configuration, to prevent spectral overlap with the NRB generated by the $\omega_{as} = 2\omega_p - \omega_s$ process. The generation of three independent synchronized pulses makes TR-CARS quite complicated; for this reason, the technique has been initially implemented using amplified Ti:sapphire laser systems[82], providing enough pulse energy to generate multiple colours through optical parametric amplification. An alternative TR-CARS scheme has been recently demonstrated starting from a simpler two-colour configuration, where the frequency components of an ultrashort continuum pulse, typically generated by spectral broadening in an optical fiber, provide simultaneous pump/Stokes colours, impulsively exciting the ground state vibrational coherence, and a time-delayed narrowband probe generates the NRB-free CARS signal[83; 84].

The laser sources typically used for TR-CARS have been either oscillators, with high repetition rate ($\approx$ 100 MHz) and low pulse energy (a few nJs) or amplified Ti:sapphire systems, with low repetition rate ($\approx$ 1 kHz) and high pulse energy (a few mJs). The recent development of all-solid state femtosecond Yb-

based systems, either in the bulk or in the fiber format, has allowed accessing an intermediate parameter range, with repetition rate up to ≈ 1 MHz and energy of several Js. This regime has not been deeply explored so far for nonlinear spectroscopy/microscopy, but it offers an interesting compromise between high pulse energy, enhancing the non-linear effects, and high repetition rate, enabling fast acquisition times. Besides, diode pumping makes these sources particularly compact and reliable, and thus amenable to in-field operation.

In this Chapter, we are going to combine broadband, time-resolved and non-degenerate CARS configurations in a simple setup based on a single free space femtosecond Yb:KYW laser. The system allows generating the three synchronized colours - pump, broadband Stokes and narrowband probe- in a straightforward fashion, enabling the acquisition of broadband, NRB-free CARS spectra with very high signal-to-noise ratios and short acquisition times.

4.2 Experimental Setup

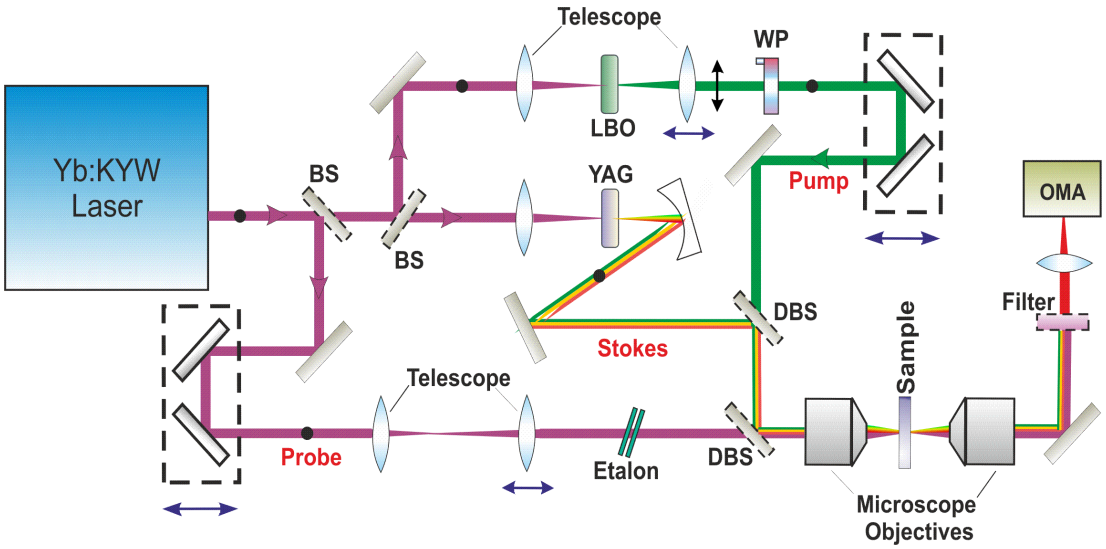


Figure 4.1: Schematic diagram of the experimental setup for TR-CARS. BS: beam splitter; DBS: dichroic beam splitter; LBO: lithium triborate; WP: half-wave plate; OMA: optical multichannel analyzer.

The experimental setup used for the broadband TR-CARS is sketched in Figure(4.1). It starts with a regeneratively amplified Yb:KYW laser (femtoREGEN, HighQLaser) based on a dual-head cavity and producing 1040-nm, 350-fs

pulses with an average power up to 8 W and a repetition rate selectable between 300 kHz and 1 MHz. The laser output is split into three beams and is used to generate in a straightforward fashion the three required colours: pump, broadband Stokes and narrowband probe. The pump is produced by second-harmonic generation in a 10-mm-long lithium triborate [LBO] crystal, resulting in 520-nm pulses with $\sim 60 cm^{-1}$ bandwidth (500-fs duration). The Stokes is obtained by white-light continuum (WLC) generation in a bulk medium, focusing a $\sim 4-5\mu J$ fraction of the available energy in a 4-mm-thick YAG plate (it has been shown that low-bandgap materials such as YAG enable the generation of a stable WLC even with relatively long pulses, such as the ones used here). The blue portion of the WLC from 500 to 630 nm is selected by a short-pass filter, to avoid spectral superposition with the non-degenerate CARS signal: it is spectrally quite flat and displays a remarkable shot-to-shot stability. In combination with the Raman pump at 520 nm, it enables the simultaneous excitation of all vibrational modes of interest, from low frequencies up to $\approx 3300 cm^{-1}$. After spectral filtering the average power of the Stokes beam amounts to nearly 1 mW. The third beam is finally used to produce a narrowband probe at 1040 nm. Spectral narrowing is passively achieved by means of a properly designed etalon (SLS Optics Ltd.) providing a finesse of 12 and a free-spectral-range of $85 cm^{-1}$, which results in an overall spectral resolution of 7.5 cm^{-1}. Figure (4.2) reports in a normalized scale the spectra of pump, Stokes, and probe beams. The probe spectrum is better resolved in the inset of Figure (4.2): it exhibits the expected Lorentzian shape, with a FWHM of 13 cm^{-1}, without any side lobe given by adjacent resonances of the etalon. It is worth noting that the Lorentzian transmission spectrum of the etalon, which corresponds to a pulse temporal profile consisting of a sharp rise followed by an exponential decay, is very much suited to the purpose of an efficient TR-CARS interaction. On one hand the sharp rise, since it gives minimum temporal overlap with the pump and Stokes pulses, allows for an efficient suppression of the NRB; on the other hand the exponential decay can be chosen to match the typical dephasing time of the vibrational coherence, thus maximizing the interaction with the sample. The non-degenerate CARS falls in the spectral

region between 1040 nm (corresponding to zero frequency detuning) and 775 nm (3300 cm^{-1}), and can thus be efficiently detected by a silicon spectrometer.

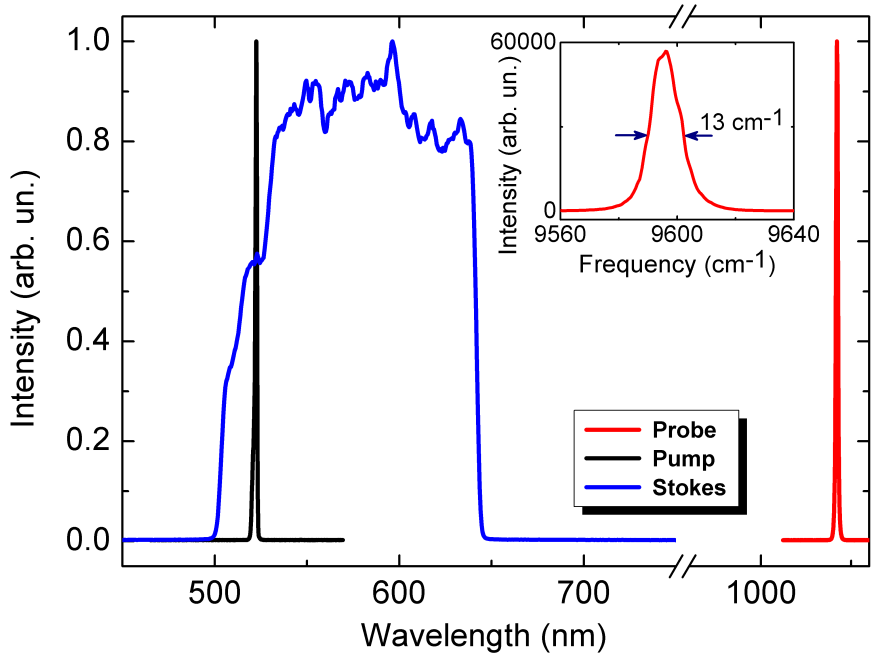


Figure 4.2: spectra of the pump (black), Stokes (blue) and probe (red) pulses. Inset: zoom of the probe spectrum indicating a 13 cm^{-1} FWHM (after deconvolution with the spectrometer response).

Pump, Stokes and probe pulses are collinearly superimposed with dichroic beam splitters and focused on the sample by a 0.7 NA microscope objective. Telescopes on the pump and probe arms are adjusted to match the focal planes of the three beams. A computer-controlled delay line ensures reproducible delay of the probe pulse with respect to the pump/Stokes pair. The CARS signal, selected by a suitable combination of long- and short-pass filters, is sent to a commercial optical-multi-channel-analyzer (OMA, model) with 4 cm^{-1} spectral resolution and a maximum acquisition speed of 1 kHz.

4.2.1 Repetition-rate advantage

It is interesting to compare the performance of our 1-MHz system with those of standard broadband CARS systems based on femtosecond Ti:sapphire oscillators.

We start by recalling that the instantaneous CARS intensity is proportional to the product of the intensities of the three interacting beams, according to the formula $I_{CARS} \propto I_p I_s I_{pr}$. By relating the intensities to the corresponding average power levels P and to the laser repetition-frequency f_{rep} through the approximated relationships $I = \frac{U}{\tau A}$ and $P = U f_{rep}$,where U, τ and A being the pulse energy, the pulse-width and an effective area for the beam cross-section, respectively - one readily finds $P_{CARS} \propto \frac{P_p P_s P_{pr}}{\tau A f_{rep}}$, where the same τ and A have been considered, for the sake of simplicity, for all beams. One can thus see that the CARS power scales as $\frac{1}{f_{rep}^2}$, with the consequence that for comparable average-power values of the three beams, moving from an oscillator (f_{rep} = 50 to 100 MHz) to an Yb-based amplifier ($f_{rep} \approx$ 1 MHz) increases the CARS signal by 3 to 4 orders of magnitude.

4.2.2 Degenerate-CARS configuration

To assess the potential of our system for broadband CARS spectroscopy/ microscopy, we performed preliminary experiments with a simplified degenerate configuration [Figure 4.3], using the 520-nm pump and the WLC Stokes.

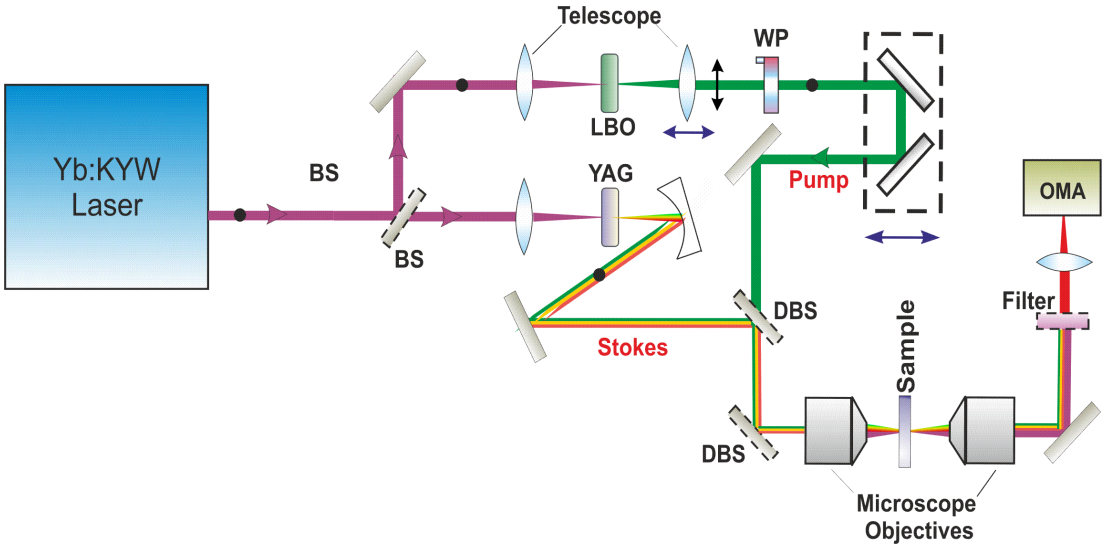


Figure 4.3: The experimental setup for degenerate CARS. BS: beam splitter; DBS: dichroic beam splitter; LBO: lithium triborate; WP: half-wave plate; OMA: optical multichannel analyzer.

Although the Stokes pulse is broadband enough to enable covering of all vibra-

tional frequencies from 0 to 3300 cm^{-1}, the dispersion introduced by the refractive optics on its path (in particular the microscope objective) must be carefully compensated to ensure temporal overlap of all its colours with the relatively short ($\approx 300fs$) pump pulse. For these experiments, we concentrated on the 2400-3200 cm^{-1} spectral region, covering the C-H bonds, which is of interest for many applications. Figure (4.4(a)) reports the broadband degenerate CARS spectra of several solvents. Due to the high peak intensities provided by our system, the degenerate CARS signal (which falls in the 445-460 nm wavelength range) was very intense, amounting to $\approx 200nW$ for methanol when using a 10 mW level of pump/probe power. This signal heavily saturates our OMA even for the shortest acquisition times (1 ms), thus in principle enabling acquisition of spectra at much higher speeds. Even if qualitatively in agreement with the corresponding Raman spectra, these degenerate CARS spectra are affected by two main problems: a rather poor frequency resolution, which results from the 60 cm^{-1} spectral width of the pump beam, and the asymmetrical dispersive shape of the main peaks, which is due to the coherent superposition with a strong NRB.

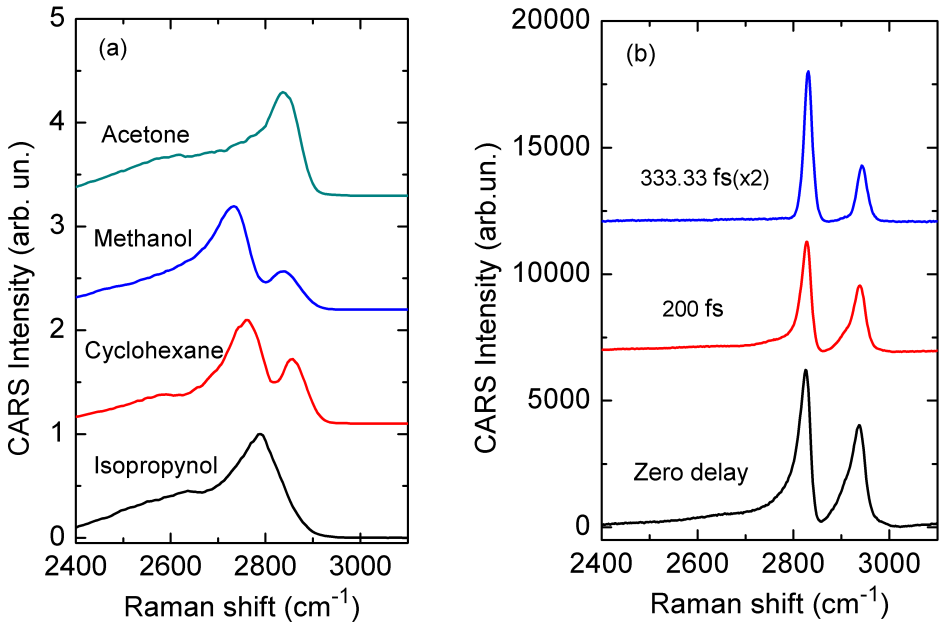


Figure 4.4: (a) Degenerate CARS spectra of different solvents; (b)TR-CARS spectra of methanol as a function of the delay of the probe pulse with respect to the pump/ Stokes pair.

4.2.3 The TR-CARS configuration

Figure (4.4(b)) shows TR-CARS spectra of methanol, for different delays between the probe pulse and the pump/Stokes pair. At time zero, the spectrum still displays the characteristic dispersive shape due to interference with the NRB and closely resembles the degenerate CARS, although with higher spectral resolution due to the narrower width of the probe. A delay of $\Delta t = 330 fs$ is already sufficient to completely suppress the NRB, making the shapes of the two main resonances much more symmetrical and shifting their maxima to the 2830 and 2945 cm^{-1} values that are expected from the spontaneous Raman spectra of the molecule. It should be noted that the peculiar probe pulse temporal profile produced by the etalon, consisting of a sharp rise followed by an exponential decay, enables NRB suppression with small Δt values, roughly corresponding to the pump pulse duration. For this reason. the signal penalty in the time-delayed CARS spectrum is rather limited, of the order of 3 to 4.

Figure (4.5(a)) reports TR-CARS spectra of various solvents. Even the rather congested spectrum of isopropynol is now perfectly resolved. Due to imperfect mode-matching between the three beams, the overall CARS signal is reduced with respect to the two-colour case, but it is still sufficient to nearly saturate the OMA with 1-ms acquisition time. Given the very high signal-to-noise of the spectra, it is reasonable to foresee that a dedicated and faster spectrometer could acquire CARS spectra within significantly shorter times, enabling high-speed, background-free, broadband vibrational imaging.

To assess the sensitivity of our system, we studied solutions of methanol diluted in water. Figure (4.5(b)) reports a TR-CARS spectrum for a 6.25% methanol concentration. Even at such a strong dilution factor, the spectral features of methanol are clearly resolved with respect to the huge water resonance. By software analysis the water response could even be subtracted, allowing for full chemical identification of the sample even at significantly higher dilutions. This example shows how the broadband capability can be successful in the identification of molecular compounds with more or less congested spectral features even within environments giving strong non-resonant and also resonant contributions.

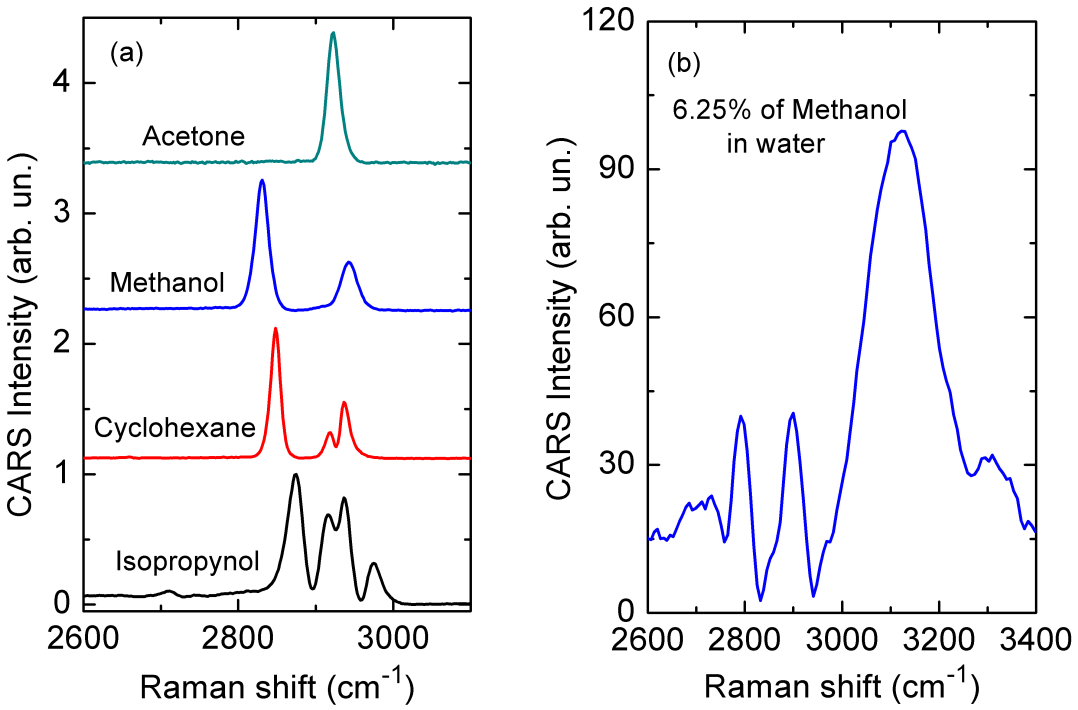


Figure 4.5: ((a) TR-CARS spectra of different solvents at $\Delta t = 330fs$; (b) TR-CARS spectrum of a 6.25% diluted solution of methanol in water.

4.3 Conclusions

We have presented a setup for broadband non-degenerate TR-CARS spectroscopy based on a single femtosecond Yb:KYW laser system. Pump, broadband Stokes and narrowband probe are generated in a straightforward fashion by direct non-linear and linear manipulation of the Yb:KYW pulses. Shaping of the probe pulse by an etalon gives the optimum temporal profile for efficient NRB suppression. The combination of high repetition rate (1 MHz) and pulse energy ($\mu J-$level) guarantees intense CARS signals, enabling short acquisition times for the spectra.

The rapid technological development of Yb-based femtosecond lasers, which become increasingly powerful, compact and reliable, makes our solution of interest for high-speed vibrational spectroscopy/imaging. The use of a pump pulse in the visible (520 nm) limits the applicability of the system to the imaging of biological compounds, due to the damage induced by two-photon absorption. On the other hand, in other applications such as pharmaceutics and micro-fluidics, for which

photodamage is a lesser concern, it could become a work-horse for vibrational detection and identification of molecules. It is also likely to give a strong impact in the field of biological imaging provided the same scheme is extended to longer wavelengths.

Chapter 5

Balanced-detection Raman Induced Kerr Effect spectroscopy

In this Chapter, Raman Induced Kerr Effect (RIKE)spectroscopy/microscopy[85] is introduced, which allows mapping of different components of $\chi^{(3)}$. Two types of traditional detection schemes, Crossed Polarizers detection and Optical heterodyne detection (OHD-RIKE), commonly employed in RIKE spectroscopy are presented. Then a novel approach called balanced-detection Raman-induced Kerr effect (BD-RIKE) microscopy, as a new powerful coherent Raman imaging technique, is discussed, It combines the advantage, the linear-background-free detection typical of CARS with the main advantages of SRS i.e. the linear concentration dependence and non-linear background-free detection.

5.1 Raman Induced Kerr Effect(RIKE)

Like other CRS processes, RIKE can be understood as a four-wave mixing process, where emitted signal comes from a third-order material response to the incident light fields. Central in the RIKE process is the *Optical Kerr Effect(OKE)[86]* induced by the Raman process inside the medium. The OKE is presented in more detail in Appendix C. The RIKE changes the polarization of one of the excitation beams due to Raman induced birefringence in the sample. Like SRS, in RIKE, the generated emission is thus at the excitation frequency, but in contrast to SRS, the emitted radiation is polarized perpendicular to the excitation field. In this aspect, RIKE is similar to the CARS, as the emitted radiation does not interfere

with the excitation field, while in SRS, the interference of the emitted radiation generates the intensity gain(SRG) or loss(SRL) in the excitation field.

The RIKE response of the material can be understood as generated by the third-order induced polarization $P^{(3)}$ given by equation(1.19) as::

$$P_i^{(3)}(\omega_4) \propto \chi_{ijkl}^{(3)} E_j(\omega_1) E_k(\omega_2) E_l(\omega_3), \tag{5.1}$$

where $\chi_{ijkl}^{(3)}$ is the component of third-order susceptibility tensor involved in the RIKE, and $E_j(\omega_1)$, $E_k(\omega_2)$, $E_l(\omega_3)$ are the electric fields of the excitation beams.

Traditionally, two different type of beam polarization geometries have been employed for the RIKE spectroscopy:

1. Linearly polarized pump beam at an angle of 45^0 with respect to linearly polarized Stokes beam. This geometry is known as **linear RIKE**.

2. Circularly polarized pump beam and linearly polarized Stokes beam. This geometry is known as **circular RIKE**.

It can be recalled from Section (1.3) that in an isotopic medium, $\chi_{1111}^{(3)}$, $\chi_{1221}^{(3)}$, $\chi_{1212}^{(3)}$, $\chi_{1122}^{(3)}$ and their permutations are the only non-vanishing elements of the third-order susceptibility tensor. Above mentioned polarization geometries of the excitation beams can induce different combination of $\chi_{1212}^{(3)}$ and $\chi_{1122}^{(3)}$ components[17].

Far from any electronic resonance, both $\chi_{1212}^{(3)}$ and $\chi_{1122}^{(3)}$ have resonant and non-resonant contributions, for the CRS processes, given by equation(1.16)as:

$$\chi_{1212}^{(3)} \propto (\chi_{1212}^{(3)R,Re} + i\chi_{1212}^{(3)R,Im}) + \chi_{1212}^{(3)NR,Re} \tag{5.2a}$$

$$\chi_{1122}^{(3)} \propto (\chi_{1122}^{(3)R,Re} + i\chi_{1122}^{(3)R,Im}) + \chi_{1122}^{(3)NR,Re}, \tag{5.2b}$$

with the property: $\chi_{1212}^{(3)NR,Re} = \chi_{1122}^{(3)NR,Re}$.

We will now derive separate expressions for the effective third-order nonlinear susceptibilities $\chi_{eff}^{(3)}$ induced in linear and circular RIKE respectively, as well as for the corresponding signal amplitudes.

5.1.1 Linear RIKE

The linear RIKE polarization scheme is shown in Figure(5.1). In linear RIKE, the linearly polarized input field amplitudes of pump and Stokes can be represented

in Cartesian coordinates as:

$$A_p = A_p^x + A_p^y \tag{5.3a}$$

$$A_s = A_s^x \tag{5.3b}$$

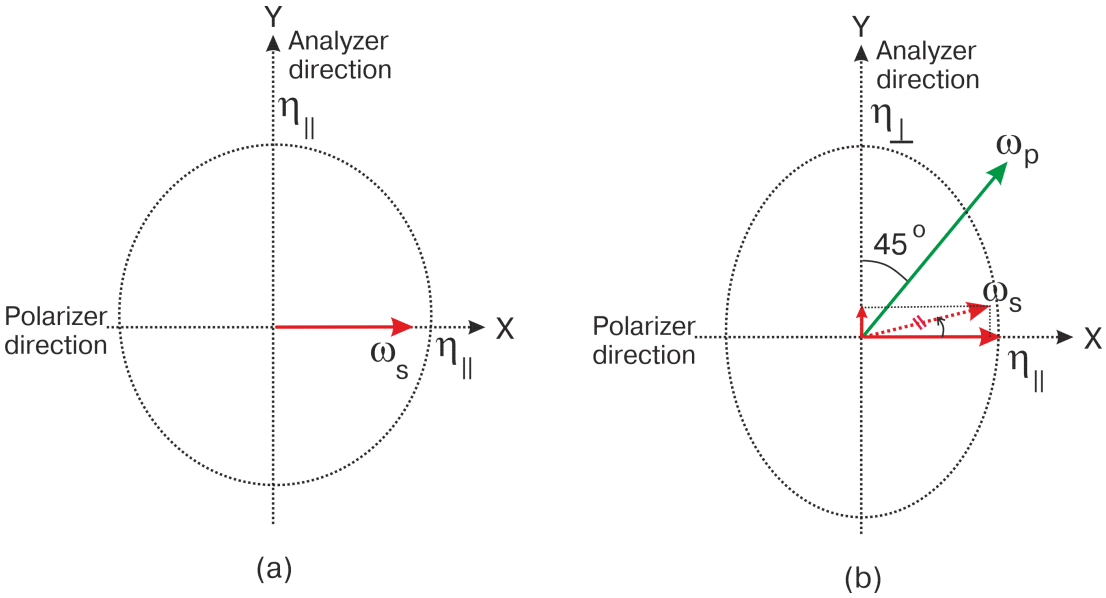


Figure 5.1: Polarization scheme for linear RIKE .

By introducing the assignments:

$$\begin{aligned} \omega_1 &\equiv \omega_p^x \quad \omega_2 \equiv \omega_p^y \\ \omega_3 &\equiv \omega_s^x \quad \omega_4 \equiv \omega_s^y \end{aligned} \tag{5.4}$$

which correspond to:

$$\begin{aligned} A_1 &\equiv A_p^x \quad A_2 \equiv A_p^y \\ A_3 &\equiv A_s^x \quad A_4 \equiv A_s^y, \end{aligned} \tag{5.5}$$

the third-order induced polarization at ω_s^y giving RIKE signal, is provided by the equation(1.46d) as:

$$p_{NL}^{(\omega_s^y)} = \frac{3}{8}[\chi_{1212}^{(3)} A_p^x (A_p^y)^* A_s^x + \chi_{1122}^{(3)} (A_p^y) A_p^{x*} A_s^x] \tag{5.6a}$$

$$= \frac{3}{8}[\chi_{1212}^{(3)} + \chi_{1122}^{(3)}] A_p^x (A_p^y)^* A_s^x \tag{5.6b}$$

$$= \frac{3}{8}[\chi_{eff}^{(3)linear}] A_p^x (A_p^y)^* A_s^x \tag{5.6c}$$

where effective third-order nonlinear susceptibility induced in linear RIKE is given as:

$$\chi_{eff}^{(3)linear} = \chi_{1212}^{(3)} + \chi_{1122}^{(3)} \tag{5.7a}$$

$$= [\chi_{1212}^{(3)R,Re} + \chi_{1122}^{(3)R,Re} + \chi_{1212}^{(3)NR,Re} + \chi_{1122}^{(3)NR,Re}] \tag{5.7b}$$

$$+ i[\chi_{1212}^{(3)R,Im} + \chi_{1122}^{(3)R,Im}] \tag{5.7c}$$

Here numbers 1 and 2 are assigned to Y- and X-directions respectively.

The corresponding equation for the field propagation is given by equation(1.47d) as:

$$\frac{\partial A_s^y}{\partial z} = -i\alpha_s \chi_{eff}^{(3)linear} A_p^x (A_p^y)^* A_s^x, \tag{5.8}$$

where *phase-matching condition*($\Delta k \equiv k_s + k_p - k_p - k_s = 0$) is automatically satisfied.

Considering the un-depleted pump and Stokes during the interaction (i.e.$A_p^x \backsimeq$ *constt.* and $A_p^y \backsimeq$ *constt.* and $A_s^x \backsimeq$ *constt.*), the equation(5.8) can be solved for orthogonally polarized Stokes field component, which is the signal in RIKE experiments, for interaction length L with initial condition $A_s^y(0,t) = 0$, as:

$$\int_0^L dA_s^y(r,t) = -i\alpha_s \chi_{eff}^{(3)linear} A_p^x (A_p^y)^* A_s^x \int_0^L dz \tag{5.9}$$

$$\Rightarrow \Delta A_s \equiv A_s^y(L,t) = -i\alpha_s \chi_{eff}^{(3)linear} A_p^x (A_p^y)^* A_s^x . L \tag{5.10}$$

Such an expression mimics the expression for SRS except the differences in polarization directions of the fields, and we will see in the following sections that this field expression translates into different responses depending on the detection schemes employed.

5.1.2 Circular RIKE

In the Circular RIKE configuration [shown in Figure(5.2)], the pump beam is circularly polarized while the Stokes beam is linearly polarized. The input field amplitudes of circularly polarized pump and linearly polarized Stokes can be represented in Cartesian coordinates as:

$$A_p = A_p^x + iA_p^y \tag{5.11a}$$

$$A_s = A_s^y \tag{5.11b}$$

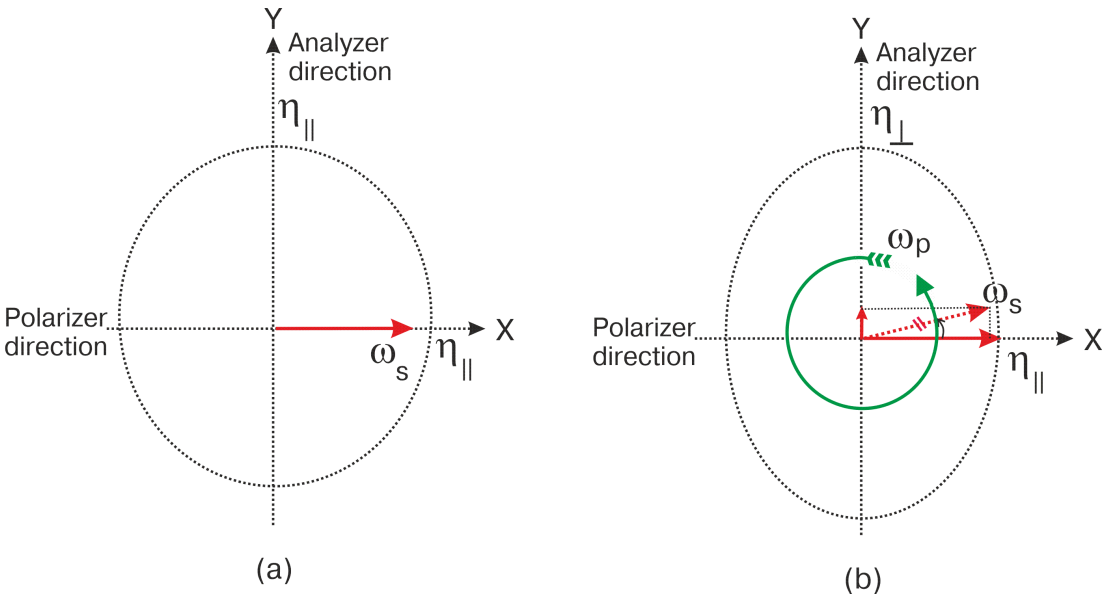


Figure 5.2: Circular RIKE polarization scheme.

In equations (1.46d), after the assignments:

$$\begin{aligned} \omega_1 \equiv \omega_p^x \quad \omega_2 \equiv \omega_p^y \\ \omega_3 \equiv \omega_s^x \quad \omega_4 \equiv \omega_s^y \end{aligned} \tag{5.12}$$

which implies:

$$\begin{aligned} A_1 \equiv A_p^x \quad A_2 \equiv iA_p^y \\ A_3 \equiv A_s^x \quad A_4 \equiv A_s^y, \end{aligned} \tag{5.13}$$

the third-order induced polarization at ω_s^y giving RIKE signal, is provided as:

$$p_{NL}^{(\omega_s^y)} = \frac{3}{8}[\chi_{1212}^{(3)} A_p^x (iA_p^y)^* A_s^x + \chi_{1122}^{(3)} (iA_p^y)(A_p^x)^* A_s^x] \tag{5.14a}$$

$$= \frac{3}{8}[i.(\chi_{1122}^{(3)} - \chi_{1212}^{(3)})] A_p^x (A_p^y)^* A_s^x \tag{5.14b}$$

$$= \frac{3}{8}[\chi_{eff}^{(3)circ}] A_p^x (A_p^y)^* A_s^x \tag{5.14c}$$

where effective third-order nonlinear susceptibility induced in circular RIKE is given as:

$$\chi_{eff}^{(3)circ} = i.(\chi_{1122}^{(3)} - \chi_{1212}^{(3)}) \tag{5.15a}$$

$$= [\chi_{1122}^{(3)R,Im} - \chi_{1212}^{(3)R,Im}] + i[\chi_{1122}^{(3)R,Re} - \chi_{1212}^{(3)R,Re}] \tag{5.15b}$$

The noticeable point here is that $\chi_{eff}^{(3)circ}$ is free from any non-resonant contribution[87] because of the property $\chi_{1212}^{(3)NR,Re} = \chi_{1122}^{(3)NR,Re}$.

And the corresponding equation for the field propagation is given with the help of equation(1.47d) as:

$$\frac{\partial A_s^x}{\partial z} = -i\alpha_s \chi_{eff}^{(3)circ} A_p^x (A_p^y)^* A_s^x, \tag{5.16}$$

where exponential term is absent because *phase-matching condition*($\Delta k \equiv k_s + k_p - k_p - k_s = 0$) is automatically satisfied.

Considering the un-depleted pump and Stokes during the interaction (i.e. $A_p^x \backsimeq$ *constt.* and $A_p^y \backsimeq$ *constt.* and $A_s^x \backsimeq$ *constt.*), the equation(5.8) can be solved for the orthogonally polarized Stokes field component(i.e. the RIKE signal) for interaction length L with initial condition $A_s^y(0,t) = 0$, as:

$$\int_0^L dA_s^y(r,t) = -i\alpha_s \chi_{eff}^{(3)circ} A_p^x (A_p^y)^* A_s^x \int_0^L dz \tag{5.17}$$

$$\Rightarrow \Delta A_s \equiv A_s^y(L,t) = -i\alpha_s \chi_{eff}^{(3)circ} A_p^x (A_p^y)^* A_s^x . L \tag{5.18}$$

So far we have discussed the excitation schemes for RIKE. To detect the generated RIKE signal, the polarization sensitive detection schemes are needed.

5.2 The polarization sensitive detection schemes for RIKE

The two routinely employed polarization sensitive detection schemes in RIKES experiments are the crossed polarizers scheme and the optically heterodyned detection(OHD) scheme. A novel balanced detection scheme is recently developed by us, which has several advantages over the previous two schemes. Altogether the three schemes can be listed as follows:

1. Crossed polarizers RIKE
2. OHD-RIKE
3. Balanced detection RIKE (BD-RIKE)

In the following two sub-sections, we will go through the configurations (1) and (2) respectively and observe the kind of material responses they are able to probe, while an entire section(5.3) will be dedicated to BD-RIKE scheme.

5.2.1 Crossed polarizers RIKE

This is the simplest experimental way to detect RIKE signal using two crossed polarizers. The schematic of the detection setup is reported in Figure(5.3).

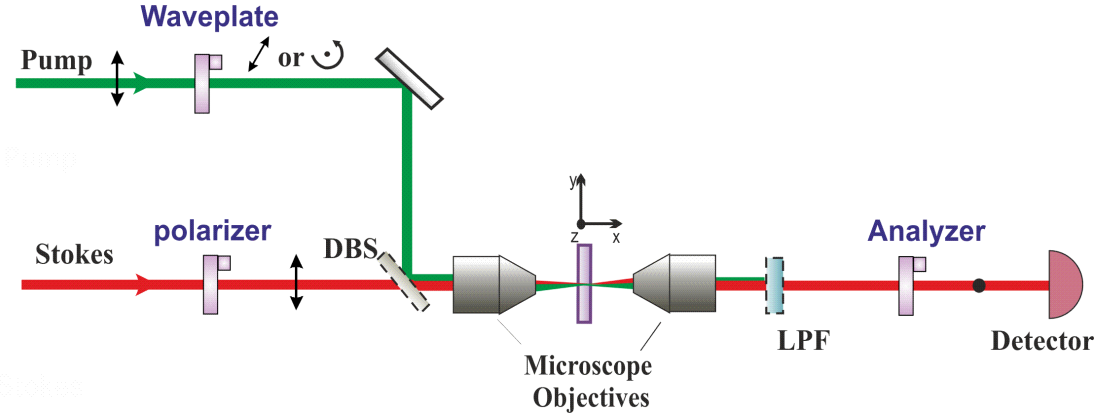


Figure 5.3: The schematic of setup for crossed polarizers RIKE; DBS: Dielectric beam splitter, LPF: Long wave pass filter.

The first polarizer is inserted before the sample in the Stokes path and is oriented in such a way to let the horizontally polarized Stokes (let say it along X-axis) pass through it. Another polarizer is put after the sample, rotated by 90^0 (that is along Y-axis), in order to detect only the signal orthogonal to the incoming one. In this way, we will be able to extract only A_s^y field which is our RIKE signal.

Detection of linear RIKE

After the second polarizer, we detect the intensity of depolarized field $A_s^y(L,t)$ given by equation(5.10), therefore:

$$I_{LinearRIKE} \propto |A_s^y(L,t)|^2 \tag{5.19a}$$

$$\propto \alpha_s^2 |\chi_{eff}^{(3)linear}|^2 I_p^x I_p^y I_s^x .L^2 \tag{5.19b}$$

$$\propto \alpha_s^2 |\chi_{eff}^{(3)linear}|^2 I_p^2 I_s .L^2, \tag{5.19c}$$

where $I_p^y = I_p^x \backsimeq I_p/2$

Thus, $I_{LinearRIKES} \propto |\chi_{eff}^{(3)linear}|^2 = |\chi_{1212}^{(3)} + \chi_{1122}^{(3)}|^2$, which gives rise to several spurious contributions that prevent this scheme to be non-resonant background-free.

Detection of circular RIKE

In this case, after the second polarizer, we detect the intensity of depolarized field $A_s^y(L,t)$ given by equation(5.18), therefore:

$$I_{CircularRIKES} \propto |A_s^y(L,t)|^2 \tag{5.20a}$$

$$\propto \alpha_s^2 |\chi_{eff}^{(3)circ}|^2 I_p^x I_p^y I_s^x . L^2 \tag{5.20b}$$

$$\propto \alpha_s^2 |\chi_{eff}^{(3)circ}|^2 I_p^2 I_s . L^2, \tag{5.20c}$$

where pump is circularly polarized, hence $I_p^y = I_p^x \backsimeq I_p$

Thus, we detect circular RIKES signal as, $I_{CircularRIKES} \propto |\chi_{eff}^{(3)circ}|^2 = |i(\chi_{1122}^{(3)} - \chi_{1212}^{(3)})|^2 = (\chi_{1212}^{(3)R,Real} - \chi_{1122}^{(3)R,Real})^2 + (\chi_{1212}^{(3)R,Imaginary} - \chi_{1122}^{(3)R,Imaginary})^2$. The resonant-real and the resonant-imaginary parts being orthogonal to each other do not interfere, hence we observe RIKES signal proportional to combination of squares of their difference, but without the capability to separate the real parts from the imaginary ones and vice versa. However circular RIKE is NRB-free.

5.2.2 Optically Heterodyne Detection RIKE (OHD-RIKE)

Optical heterodyne detection is a standard technique in spectroscopy to amplify small signal field. For this purpose, the signal field is made to interfere with a coherent field, called *local oscillator(LO)*, at the same frequency and polarization of the signal field. In both linear and circular RIKE, the generated field in the sample has the same frequency as of the Stokes field, but polarization direction is perpendicular to the input Stokes field.

The polarization schemes for linear and circular OHD-RIKES are shown in Figure(5.4).

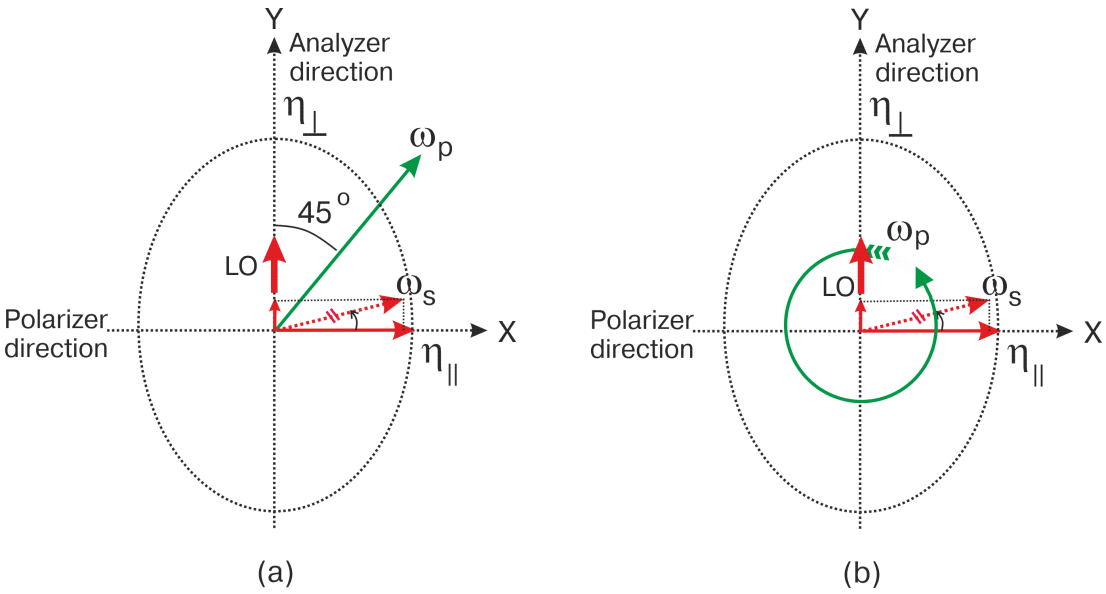


Figure 5.4: The polarization schemes for (a)Linear and (b)circular OHD-RIKE.

In OHD-RIKES[17; 18], the LO field can be obtained in two ways: first, by purposefully rotating slightly the polarization direction of the input linearly polarized Stokes beam in the Y-direction used for detection with the help of input polarizer (of the crossed polarizers RIKES)in order to transmit some Stokes field in the polarization direction of the generated RIKE field, second, by supplying a phase-coherent external field at the Stokes frequency in the polarization direction of the generated RIKE field. This LO field (we will denote it by A_s^x and in order to differentiate it with RIKES field, from now we will denote RIKE field by ΔA_s^x), transmitted through the second polarizer, interferes with the RIKE field, and generates the following intensity:

$$I = |\Delta A_s + A_{LO}|^2 \tag{5.21a}$$

$$= |\Delta A_s|^2 + |A_{LO}|^2 + 2Re[\Delta A_s].Re[A_{LO}] + 2Im[\Delta A_s].Im[A_{LO}] \tag{5.21b}$$

If $|A_{LO}| \ggg |\Delta A_s|$, the first term in equation (5.21b) will be negligible as compared to rest of three terms. Adopting a modulation transfer detection scheme in combination with a lock-in amplifier, and keeping into mind that all CRS signal fields are at 90^0 phase with respect to the excitation fields (the fact is derived from equation(1.43)), we arrive at the following equation[the proof of this equation is

reported in Appendix (D)]:

$$I \propto (2Im[\chi^{(3)}_{eff}]Re[A_{LO}] - 2Re[\chi^{(3)}_{eff}]Im[A_{LO}]).A^x_p(A^y_p)^*A^x_s.L, \tag{5.22}$$

where $Re[A_{LO}] \equiv Re(A^y_s)$ and $Im[A_{LO}]) \equiv Im(A^y_s)$ are the real and imaginary components of the LO field. By making the phase of A_{LO} to match that of the signal A_s, i.e. $Im[A_{LO}] = 0$, only first term survives in equation(5.22), and differently, by making the phase of A_{LO} to be 90^0 with respect to that of the signal A_s, i.e. $Re[A_{LO}] = 0$, only second term survives in equation(5.22).

Linear OHD-RIKE

In this case, $\chi^{(3)}_{eff} \equiv \chi^{(3)linear}_{eff}$ and given by equation(5.15). Introducing it in equation(5.22), we have:

$$\begin{aligned} I = 2\alpha_s[(\chi^{(3)R,Im}_{1212} + \chi^{(3)R,Im}_{1122}).Re(A^y_s) - (\chi^{(3)R,Re}_{1212} + \chi^{(3)R,Re}_{1122} + \chi^{(3)NR,Re}_{1212} \\ +\chi^{(3)NR,Re}_{1122}).Im(A^y_s)]A^x_p(A^y_p)^*A^x_sL \end{aligned} \tag{5.23}$$

By observing equation (5.23), it is clear that either first or second term in the bracket can be selected by making $Im(A^y_s) = 0$ or $Re(A^y_s) = 0$ respectively by the same arguments as discussed before. In normal linear OHD-RIKE conditions, LO is in phase with the OHD-RIKE signal hence $Im(A^y_s) = 0$. Therefore, first term will be detected as:

$$I = 2\alpha_s[(\chi^{(3)R,Im}_{1212} + \chi^{(3)R,Im}_{1122})(A^y_s)]A^x_p(A^y_p)^*A^x_sL \tag{5.24a}$$

$$= 2\alpha_s[(\chi^{(3)R,Im}_{1212} + \chi^{(3)R,Im}_{1122})]I_p\sqrt{I^x_s}\sqrt{I_{LO}}.L \tag{5.24b}$$

where $A^x_p = A^y_p$ in amplitude by geometry.

In this way, OHD-RIKE signal probes pure imaginary part of $\chi^{(3)}$. In addition, OHD-RIKES signal is linearly proportional to the pump intensity and the interaction length (L), and also the number density of molecules ($N \propto \chi^{(3)}$).

In the same way, second term in equation (5.23) can be detected. For this LO has to be phase-shifted by 90^0 in order to make $Re(A^y_s) = 0$. This can be done by using some phase compensator element (for example a Babinet Soleil compensator) aligned along the polarization of the LO after the sample. In this

condition, we observe the following intensity on the photodetector:

$$I = 2\alpha_s[(\chi^{(3)R,Re}_{1212} + \chi^{(3)R,Re}_{1122} + \chi^{(3)NR,Re}_{1212} + \chi^{(3)NR,Re}_{1122}).(A^y_s)]A^x_p(A^y_p)^* A^x_s L \quad (5.25a)$$

$$= 2\alpha_s[(\chi^{(3)R,Re}_{1212} + \chi^{(3)R,Re}_{1122} + \chi^{(3)NR,Re}_{1212} + \chi^{(3)NR,Re}_{1122})]I_p\sqrt{I^x_s}\sqrt{I_{LO}}.L \quad (5.25b)$$

This OHD-RIKES signal is proportional to the real components of $\chi^{(3)}$, but is not free from NRB.

Circular OHD-RIKE [88]

In this case, $\chi^{(3)}_{eff} \equiv \chi^{(3)circ}_{eff}$ and given by equation(5.15). Noticeable point is that here non-resonant terms being equal ($\chi^{(3)NR,Re}_{1122} = \chi^{(3)NR,Re}_{1212}$) and opposite in sign, cancel each other. $\chi^{(3)circ}_{eff}$ contains only resonant terms. Introducing it in equation(5.22), we have:

$$I = 2\alpha_s[(\chi^{(3)R,Re}_{1122} - \chi^{(3)R,Re}_{1212}).Re(A^y_s) + (\chi^{(3)R,Im}_{1122} \quad (5.26a)$$

$$- \chi^{(3)R,Im}_{1212}).Im(A^y_s)]A^x_p(A^y_p)^* A^x_s.L \quad (5.26b)$$

In normal circular OHD-RIKE conditions, LO is in phase with the OHD-RIKE signal hence LO has only real component i.e. $Im(A^y_s) = 0$. Hence in equation(5.26) only first term in the bracket is detected on photodetector as :

$$I = 2\alpha_s[(\chi^{(3)R,Re}_{1122} - \chi^{(3)R,Re}_{1212}).(A^y_s)]A^x_p(A^y_p)^* A^x_s.L \quad (5.27a)$$

$$= 2\alpha_s[(\chi^{(3)R,Re}_{1122} - \chi^{(3)R,Re}_{1212})]I_p\sqrt{I^x_s}\sqrt{I_{LO}}.L \quad (5.27b)$$

Thus difference of pure real resonant components of $\chi^{(3)}$ can be probed as OHD-RIKES signal.

In the same way, second term in equation (5.26e) can be detected. For this LO has to be phase-shifted by 90^0 in order to make $Re(A^y_s) = 0$. This can be done by using some phase compensator element (for example a Babinet Soleil compensator) aligned along the polarization of the LO after the sample. In this condition, we observe the following intensity on the photodetector:

$$I = 2\alpha_s[(\chi^{(3)R,Im}_{1122} - \chi^{(3)R,Im}_{1212}).(A^y_s)]A^x_p(A^y_p)^* A^x_s L \quad (5.28a)$$

$$= 2\alpha_s[(\chi^{(3)R,Im}_{1122} - \chi^{(3)R,Im}_{1212}]I_p\sqrt{I^x_s}\sqrt{I_{LO}}.L \quad (5.28b)$$

Thus difference of pure imaginary resonant components of $\chi^{(3)}$ can be probed as OHD-RIKES signal.

Depending on the phase of A_{LO} with respect to A_s, four different type of responses are identified in OHD-RIKE as summarized in table **5.1**.

	Linear OHD-RIKES	**Circular OHD-RIKES**
$Im[A_{LO}] = 0$	$\chi_{1122}^{(3)R,Im} + \chi_{1212}^{(3)R,Im}$	$\chi_{1122}^{(3)R,Re} - \chi_{1212}^{(3)R,Re}$
$Re[A_{LO}] = 0$	$\chi_{1122}^{(3)R,Re} + \chi_{1212}^{(3)R,Re} + NR$	$\chi_{1122}^{(3)R,Im} - \chi_{1212}^{(3)R,Im}$

Table 5.1: The detected OHD-RIKES signal from the combinations of parameters in excitation light and phase of the local oscillator

.

The main properties of OHD-RIKES can thus be given as the following:

- OHD-RIKES signal is directly proportional to the pump intensity and proportional to the square root of the Stokes intensity and square root of the LO intensity.
- It is also proportional to the interaction length (L).
- It is linear in $\chi^{(3)}$, that means linear to number density of the probing molecules. Therefore straight forward application is possible in quantitative measurements.
- OHD-RIKES gives the possibility to detect pure real and pure imaginary components of $\chi^{(3)}$ separately.

In a nut shell, OHD-RIKE allow us to successfully measure different tensor elements of the nonlinear susceptibility $\chi^{(3)}$ which is not possible with SRS. It can determine resonant (imaginary part) and dispersive (real part) components separately. It combines the advantages of P-CARS and I-CARS spectroscopy. However it is worth emphasizing that, if an external LO is used, a third phase-coherent beam is need to be synthesize for the purpose, by the laser system which is not trivial. On the other hand, in the case[18], the LO is extracted by

the rotation of A_s, the disadvantage is related to the fact that the RIKE signal will be mixed with an SRS which appears because polarization direction used in detection is not exactly perpendicular to the polarization of the incident Stokes field. This mixing can create some problem in understanding the line-shape and also in resolving different components of the $\chi^{(3)}$ responses.

5.3 Balanced Detection RIKE Spectroscopy

We introduce *balanced-detection Raman Induced Kerr Effect* (BD-RIKE) as a novel CRS technique which shares the advantages of SRS, while at the same time suppressing the linear background signal and allowing for an easier shot-noise limited detection. As in normal RIKE, it relies on the Raman-induced birefringence that occurs when the pump-Stokes frequency detuning $\omega_p - \omega_s$ is in resonance with a vibrational transition Ω, leading to a polarization rotation of the Stokes field. Here in BD-RIKE, we efficiently measure such small rotation using a combination of a proper polarization splitter with a balanced detection configuration similar to that applied for electro-optic sampling in the THz domain. Balanced detection removes the Stokes linear background and effectively cancels the laser noise, allowing to easily achieve shot-noise limited detection.

We believe that BD-RIKE represents an important addition to the arsenal of CRS techniques, combining background-free detection typical of CARS, with the absence of NRB and linear concentration dependence typical of SRS.

Scheme of BD-RIKE Spectroscopy

An understanding of BD-RIKE can be obtained by presenting the experimental setup. The schematic of the setup is shown in Figure (5.5). This experimental setup encompasses a first waveplate, WP1, on the pump branch before the sample which is used as in any RIKE configuration to switch between linear and circular RIKE excitation, depending on choice of WP1 to be a half waveplate (HWP) and a quarter waveplate (QWP) respectively. The second waveplate, WP2, is added on the Stokes branch after the sample and before a Wollaston prism, that projects the Stokes field polarization on the two axes which are exactly along the X- and

Y-axes. Figure(5.6) represents the four possible configurations that come into play when, either a HWP [panel(a)] or a QWP [panel(b)] is used for WP2. The two separated orthogonally polarized outputs of Wollaston are sent to the two identical photodiodes of a balanced detector. The balanced detector provides a photocurrent I_{BD}, that is proportional to the difference between the optical powers of the Wollaston outputs. In the absence of pump, WP2 is adjusted in such a way that the Stokes field, when projected to the WP2 axes, produces equal intensity components and thus gives no signal ($I_{BD} = 0$), whatever is the choice of WP2.

When pump beam is on and the pump-Stokes frequency detuning, $\omega_p - \omega_s$, is in resonance with a vibrational transition Ω of the sample molecule, Raman-induced birefringence that occurs, leading to a polarization rotation of the Stokes field which makes the two outputs of Wollaston prism slightly unbalanced in intensity. This slight unbalancing generates a photocurrent I_{BD} proportional to the RIKE response. We call it BD-RIKE signal. The small BD-RIKES signal is probed by using the modulation transfer scheme. For this purpose the pump beam is acousto-optically modulated and the BD-RIKE signal is detected by a lock-in amplifier.

It should be noted that any static birefringence induced by the sample does not affect the measurement, which is only sensitive to the dynamic birefringence

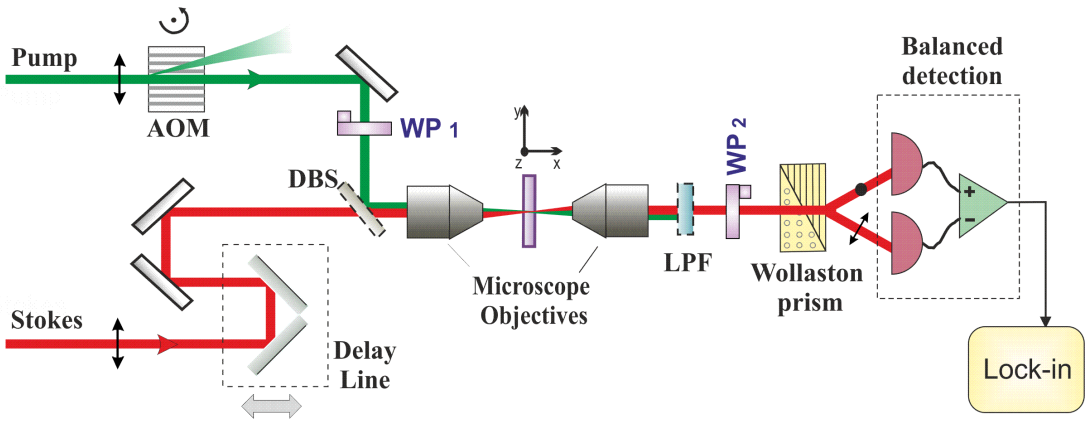


Figure 5.5: Schematic diagram for BD-RIKE. AOM: acousto-optic modulator; DBS: dichroic beam splitter; WP: waveplates; LPF: Long-pass filter rejecting pump photons.

induced by the pump beam. Because any static birefringence can be made canceled by balancing the two branches of Wollaston prism in the absence of pump beam. Furthermore, balanced detection inherently cancels online the fluctuations of the Stokes beam, allowing to reach shot-noise limited detection even at low modulation frequencies.

The four possible configurations depending on the type of excitation scheme (i.e. choice of WP1) and choice of waveplate ,WP2, in detection can be classified for simplicity in the further discussion. When HWP is in excitation, in analogy with linear RIKE, we call it *Linear BD-RIKE* and similarly when QWP is in excitation, we call it *Circular BD-RIKE*. Furthermore, for both Linear BD-RIKE and Circular BD-RIKE, two types of detection setups are possible according to choice of waveplate. We can list them as following:

- **Linear BD-RIKE**:(HWP in excitation)
  - HWP in detection
  - QWP in detection

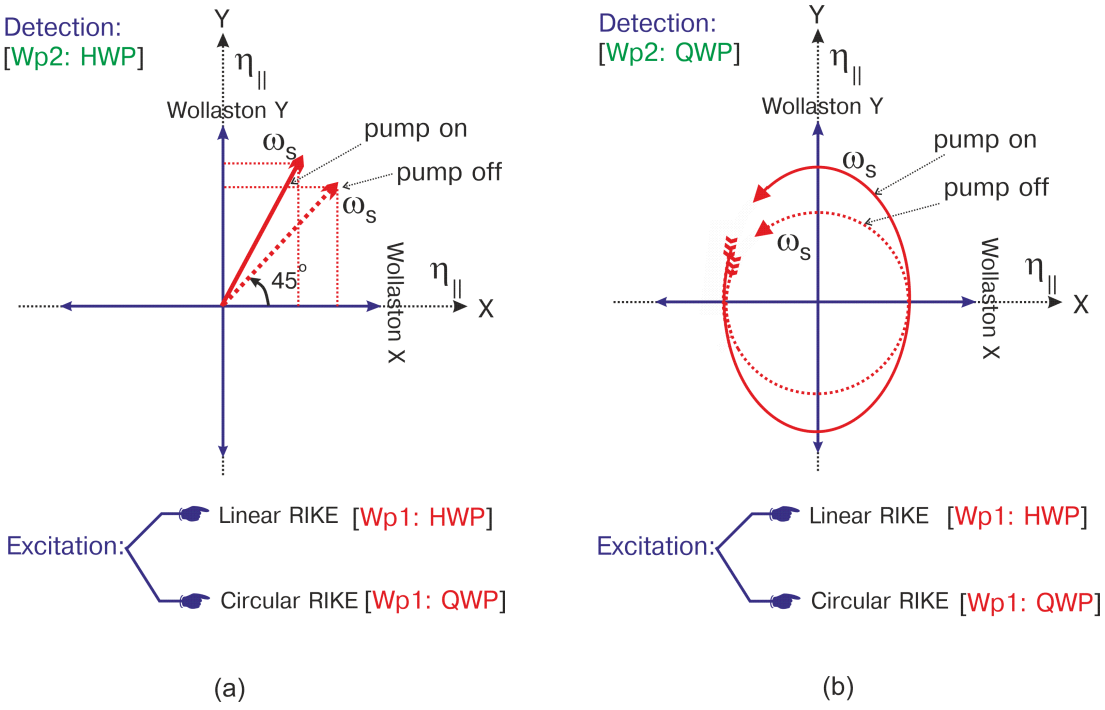


Figure 5.6: Polarization scheme for BD-RIKE(a) HWP in detection and (b) QWP in detection, for both, the isotropic sample(pump off) and the sample with induced birefringence(pump on).

- **Circular BD-RIKE**: (QWP in excitation)
  - HWP in detection
  - QWP in detection

Now we draw our attention towards theoretical significance of these four possible configurations for BD-RIKE.

5.3.1 BD-RIKE response

The response of BD-RIKE depends on the waveplate configurations and can be calculated by taking into account that I_{BD} can be shown (see Appendix E) to be proportional either to $Re[A_s^x.\Delta A_s^*]$ or to $Im[A_s^x.\Delta A_s^*]$.

More specifically balanced-detection with :

- (HWP in detection + Wollaston prism) gives: $I_{BD} \propto 2Re(A_s^x.\Delta A_s^*)$
- (HWP in detection + Wollaston prism) gives: $I_{BD} \propto 2Im(A_s^x.\Delta A_s^*)$

Here ΔA_s is the linear or circular RIKE signal, given by:

$$\Delta A_s = -i\alpha_s \chi_{eff}^{(3)} A_p^x \left(A_p^y\right)^* A_s^x.L \tag{5.29}$$

Linear BD-RIKE

In analogy with linear RIKE ,because excitation mechanism is same, we probe the same $\chi_{eff}^{(3)linear}$ given by equation(5.15), therefore:

$$\begin{aligned}
A_s^x.\Delta A_s^* &= A_s^x[-i\alpha_s \chi_{eff}^{(3)linear} A_p^x \left(A_p^y\right)^* A_s^x.L]^* && \text{(5.30a)}\\
&= [-i\alpha_s \chi_{eff}^{(3)linear}]^*.I_p I_s.L && \text{(5.30b)}\\
&= i\alpha_s([\chi_{1212}^{(3)R,Re} + \chi_{1122}^{(3)R,Re} + \chi_{1212}^{(3)NR,Re} + \chi_{1122}^{(3)NR,Re}] && \text{(5.30c)}\\
&+ i[\chi_{1212}^{(3)R,Im} + \chi_{1122}^{(3)R,Im}])^*.I_p I_s.L && \text{(5.30d)}\\
&= \alpha_s(i[\chi_{1212}^{(3)R,Re} + \chi_{1122}^{(3)R,Re} + \chi_{1212}^{(3)NR,Re} + \chi_{1122}^{(3)NR,Re}] && \text{(5.30e)}\\
&+ [\chi_{1212}^{(3)R,Im} + \chi_{1122}^{(3)R,Im}]).I_p I_s.L && \text{(5.30f)}
\end{aligned}$$

(a) HWP in detection + Wollaston prism:

The Detected intensity on balanced detector, by equation (5.30),will be:

$$I = 2Re(A_s^x.\Delta A_s^*) \tag{5.31a}$$
$$= 2\alpha_s[\chi_{1212}^{(3)R,Im} + \chi_{1122}^{(3)R,Im}].I_pI_s.L \tag{5.31b}$$

(b) QWP in detection + Wollaston prism:

Detected intensity on balanced detector, by equation (5.30),will be:

$$I = 2Im(A_s^x.\Delta A_s^*) \tag{5.32a}$$
$$= 2\alpha_s[\chi_{1212}^{(3)R,Re} + \chi_{1122}^{(3)R,Re} + \chi_{1212}^{(3)NR,Re} + \chi_{1122}^{(3)NR,Re}].I_pI_s.L \tag{5.32b}$$

Circular BD-RIKE

:

In analogy with circular RIKE ,because excitation mechanism is same, we probe the same $\chi_{eff}^{(3)circ}$ given by equation(5.15),therefore:

$$A_s^x.\Delta A_s^* = A_s^x[-i\alpha_s\chi_{eff}^{(3)circ}A_p^x\left(A_p^y\right)^*A_s^x.L]^* \tag{5.33a}$$
$$= [-i\alpha_s\chi_{eff}^{(3)circ}]^*.I_pI_s.L \tag{5.33b}$$
$$= i\alpha_s([\chi_{1122}^{(3)R,Im} - \chi_{1212}^{(3)R,Im}] + i[\chi_{1122}^{(3)R,Re} \tag{5.33c}$$
$$- \chi_{1212}^{(3)R,Re}])^*.I_pI_s.L \tag{5.33d}$$
$$= \alpha_s(i[\chi_{1122}^{(3)R,Im} - \chi_{1212}^{(3)R,Im}] \tag{5.33e}$$
$$+ [\chi_{1122}^{(3)R,Re} - \chi_{1212}^{(3)R,Re}]).I_pI_s.L \tag{5.33f}$$

(a) HWP in detection + Wollaston prism:

Detected intensity on balanced detector, by equation (5.30), will be:

$$I = 2Re(A_s^x.\Delta A_s^*) \tag{5.34a}$$
$$= 2\alpha_s[\chi_{1122}^{(3)R,Real} - \chi_{1212}^{(3)R,Real}].I_pI_s.L \tag{5.34b}$$

(b) QWP in detection + Wollaston prism:

Detected intensity on balanced detector, by equation (5.33),will be:

$$I = 2Im(A_s^x.\Delta A_s^*) \tag{5.35a}$$
$$= 2\alpha_s[\chi_{1122}^{(3)R,Imaginary} - \chi_{1212}^{(3)R,Imaginary}].I_pI_s.L \tag{5.35b}$$

The BD-RIKE responses probed in the four configurations can be summarized in the Table **5.2** :

-	Linear BD-RIKES	Circular BD-RIKES
HWP	$\chi^{(3)R,Im}_{1122} + \chi^{(3)R,Im}_{1212}$	$\chi^{(3)R,Re}_{1122} - \chi^{(3)R,Re}_{1212}$
QWP	$\chi^{(3)R,Re}_{1122} + \chi^{(3)R,Re}_{1212} + NR$	$\chi^{(3)R,Im}_{1122} - \chi^{(3)R,Im}_{1212}$

Table 5.2: The detected BD-RIKES signal arises from the different combinations of waveplates in excitation and detection

.

In the table three configurations can be identified where non-resonance(NR) contribution is absent. Moreover, the response can be selected according to the choice of waveplates and made it proportional either to real or to the imaginary part of the $\chi^{(3)}$. This adds an extremely powerful degree of freedom in selecting different molecular responses and their properties.

5.4 BD-RIKE experiments from a single fiber oscillator

The laser system we have used for BD-RIKE spectroscopy/ microscopy experiment is shown in Figure(5.7). This is the same amplified Er: fiber laser source which we have already discussed in Chapter (3) in section(3.6), as *Upgraded version of fiber-format CRS microscopy setup.*

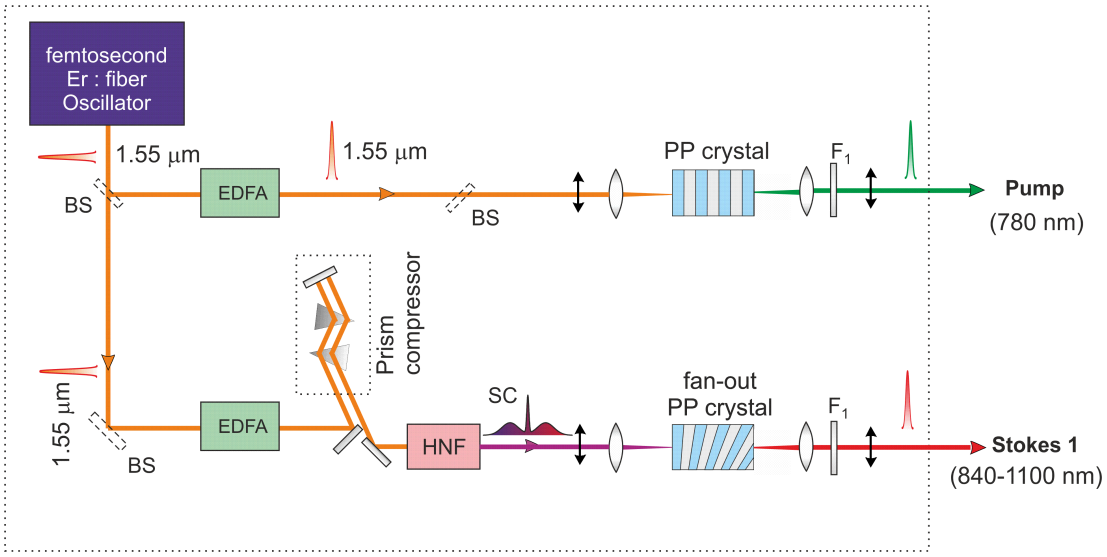


Figure 5.7: Laser system used for BD-RIKE experiment providing narrowband pump and Stokes pulses.

The BD-RIKES setup is shown in Figure (5.8). Pump and Stokes pulses are combined by a dichroic beam splitter and focused on the sample. A first waveplate (WP1) is used to control the pump polarization; it can be either a quarterwave plate (QWP) or a half-wave plate (HWP). Behind the sample, the linearly polarized Stokes is spectrally selected and, after passing through a second waveplate (WP2), is sent to a Wollaston prism that separates the beam into two equally intense replicas with perpendicular polarizations. These replicas are sent to a balanced detector providing zero output signal in the absence of pump, thus suppressing the Stokes light background. The pump beam is acousto-optically modulated and the BD-RIKE signal is detected by a lock-in amplifier. A small fraction of Stokes beam is extracted before the dichroic beam splitter by a beam-splitter which serve as reference.

All the four possible BD-RIKES configurations can be addressed by using proper combinations of HWP and QWP at waveplate positions WP_1 and WP_2. To obtain a BD-RIKE spectrum in each configuration, the Stokes wavelength is varied by translating vertically the PPLN crystal in the Stokes branch and at each wavelength, BD-RIKE signal given by lock-in is acquired. The simultaneous Stokes-wavelength readings from optical multi-channel analyzer(OMA) act as reference.

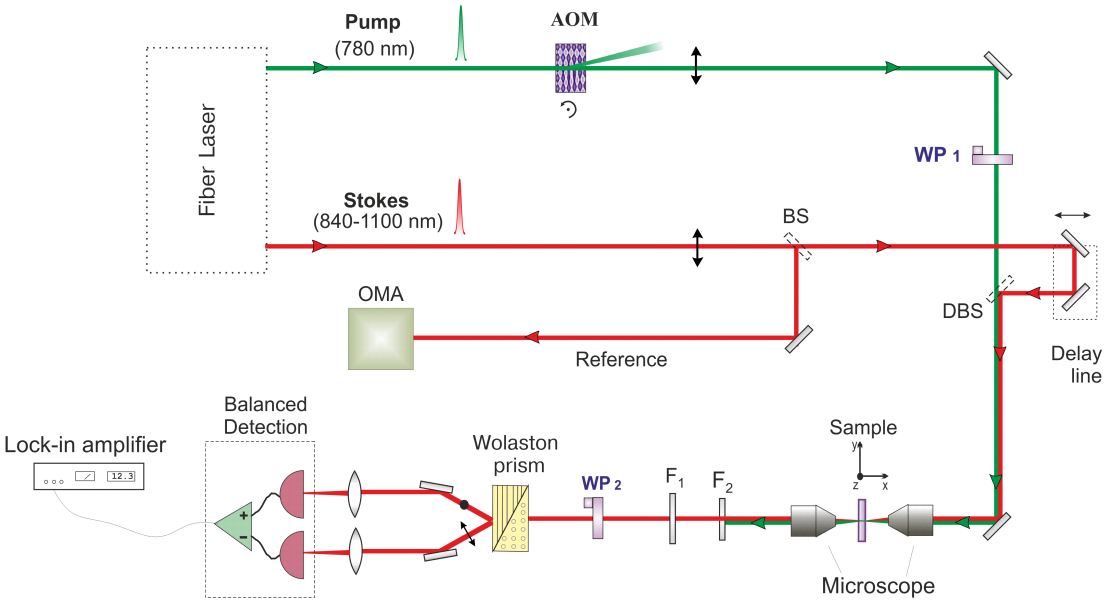


Figure 5.8: Experimental Setup for BD-RIKE spectroscopy/microscopy.

For microscopy, the pump-Stokes frequency-detuning is matched to a vibrational resonance of the sample molecule, and the sample is kept in the focal region and is moved in a transverse plane with the help of pizo-scanner. Pixel-by-pixel recording of the lock-in signal, gives the coherent Raman image of the sample plane at focus, which is referred as BD-RIKE image.

5.4.1 Experimental results

To test the system, we firstly took the Linear BD-RIKE spectrum of Acetone solution when tuned to the C-H stretching peak, with a HWP in detection, spectral position of the peak is in good agreement with the spontaneous Raman spectrum of Acetone[Figure(5.9)]. The spectrum comes out symmetric, which proves the fact that in Linear BD-RIKE with HWP in detection, we probe pure imaginary components of the $\chi^{(3)}$ involved. A fit of the spectrum using Lorentzian profile demonstrates undistorted Raman lineshape and nearly complete absence of NRB. The inset of the Figure(5.9) shows the result of a dilution test of Acetone in water, indicating a linear dependence of BD-RIKE on sample concentration. To this purpose, concentration of the Acetone solution was varied by mixing it with water and for each step, BD-RIKE signal is recorded. The inset shows the graph of BD-RIKES signal as a function of Acetone concentration, which is linear. This

proof the fact that BD-RIKES is directly proportional to the number density of the probed molecules.

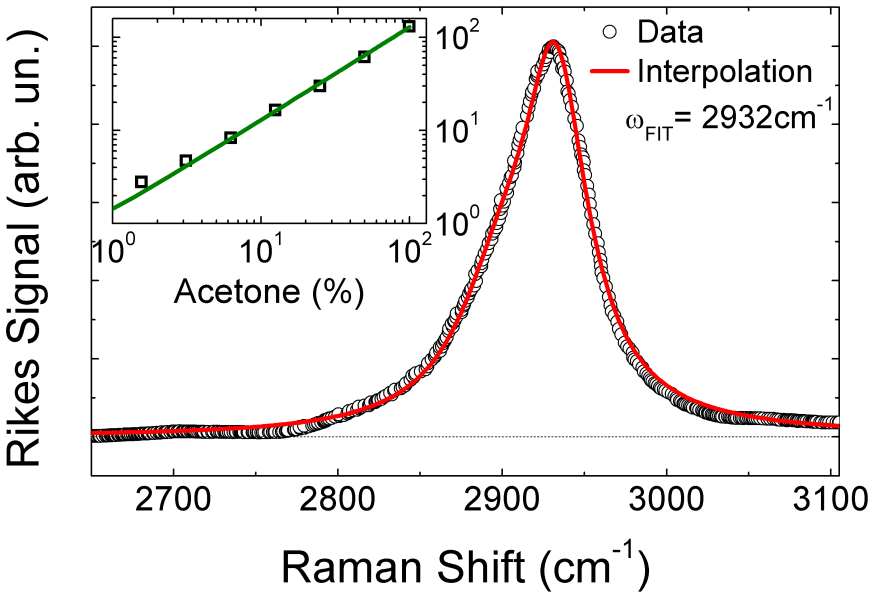


Figure 5.9: Linear BD-RIKE with HWP in detection;spectrum of Acetone solution for C-H stretching mode; In inset: RIKES signal dependence on Acetone concentration in water.

Graphs (5.10(a),(b),(c) and (d)) give the BD-RIKE spectra of all four possible combinations of WPs. The spectra are in good agreement with the aforementioned theoretical ones. In particular they prove that: **(1)** both (panel (a))Circular RIKES with QWP in detection and (panel (d)) Linear RIKES with HWP in detection, probe the pure imaginary components of the $\chi^{(3)}$ involved, while (panel (c)) Circular RIKES with HWP in detection probes the pure resonant real part of the $\chi^{(3)}$ involved.**(2)** Linear RIKES (panel(d))with QWP in detection provides a response which is the mixture of resonant and non-resonant parts of the $\chi^{(3)}$ involved.

To test the BD-RIKE microscope. We choose a blend of 3- m polystyrene (PS) and 6μm polymethylmethacrylate (PMMA) beads and probed it at the 3060 cm^{-1} PS resonance with 10 mW pump power, nearly 1 mW Stokes power and having a modulation frequency of 40 kHz. The corresponding RIKES image is shown in Figure (5.11(b)). To demonstrate the advantage of our approach, we show in Figure (5.11(a) and (b)) a comparison between SRS and BD-RIKE images, both taken in the same experimental conditions. The BD-RIKE image

(Figure 5.11(b)) shows a significantly better quality compared to the SRS ones (Figure 5.11(a)), as confirmed by the intensity profiles along the cross-sections given by the dotted lines, shown in (Figure 5.11(c)).

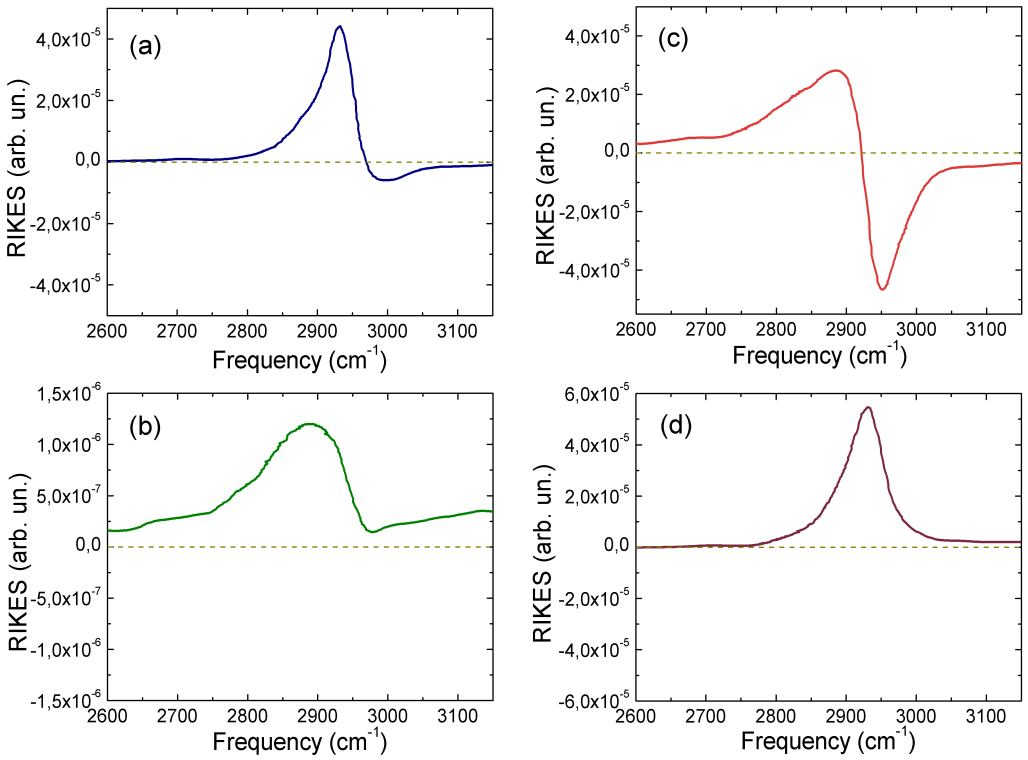


Figure 5.10: BD-RIKES spectra of Acetone in all the four configurations:(a)Circular RIKES with QWP in detection,(b)Linear RIKES with QWP in detection,(c)Circular RIKES with HWP in detection and (d)Linear RIKES with HWP in detection

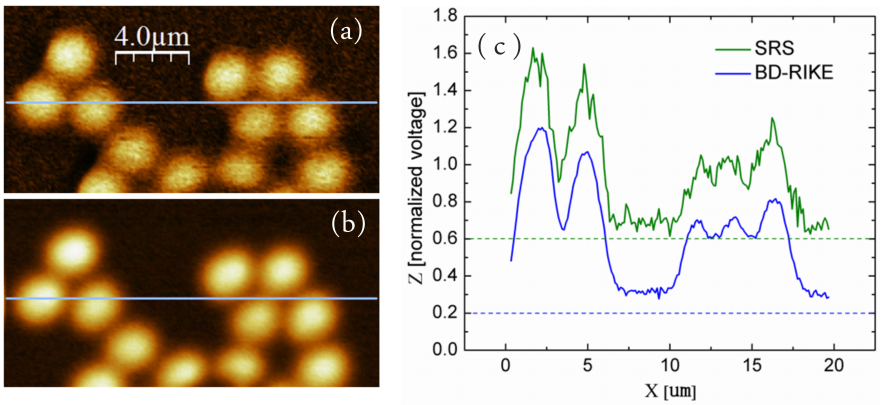


Figure 5.11: (a)SRS image of 3 micron PS beads. (b)Linear BD-RIKE image of 3 micron PS beads with HWP in detection, (c)Intensity profile across a line on images

5.5 Conclusions

We have presented a novel technique for CRS spectroscopy/microscopy, which on the one hand, offers the linear-background-free detection typical of CARS, as a result of the polarization management of the Stokes field and the balanced detection, and on the other hand, the typical linear dependence on the sample density of SRS without any NRB contribution.

Chapter 6

Conclusions

This thesis covers the research work done during my Ph.D. in the field of Coherent Raman spectroscopy/microscopy. In this period, three new approaches to Coherent Raman Spectroscopy (CRS) with overall much simplified laser excitation setups has been developed.

A novel versatile fiber-format system based on single femtosecond oscillator for Coherent Raman spectroscopy/microscopy, is developed. The setup offers performances close to the current state-of-the-art both for CARS and for SRS, but with significant advantages in terms of compactness and reconfigurability. In fact, several coherent Raman spectroscopy configurations can be easily implemented, including multiplex CARS, two-colour CRS imaging, and several non-resonant background suppression techniques in CARS. The results of the experiments: the single-frequency CARS spectroscopy, the implementation of interferometric NRB suppression technique in CARS and the multiplex CARS, performed on the setup, is reported in the thesis. The SRS spectrscopy/microscopy results with detection sensitivity as low as $\approx 2 \times 10^{-7}$, is demonstrated.

A novel configuration for broadband, time-resolved CARS spectroscopy/ microscopy , is reported, in which pump, Stokes and probe pulses are all derived from a single femtosecond Yb:KYW laser. The 1-MHz repetition rate of the system allows very intense CARS signals to be obtained over short acquisition times, while a delayed probe pulse ensures an efficient non-resonant background suppression.

A theoretical study and the experimental results of a novel approach called

balanced-detection Raman-induced Kerr effect (BD-RIKE) microscopy as a new powerful coherent Raman imaging technique, is presented. It combines the advantage of CARS i.e. the linear-background-free detection, with the main advantages of SRS i.e. the linear concentration dependence and non-linear background-free response.

Appendix A

Spontaneous Raman process

Classical theory in which both the electromagnetic radiation and the material system are treated classically, can provide useful insights into the main aspects of Raman scattering[89] process. For a molecule, the linearly induced electric dipole $P^{(1)}$ is given by

$$P^{(1)} = \alpha \cdot E, \tag{A.1}$$

where E is the electric field of the incident plane wave monochromatic radiation of frequency ω_l and α is the polarizability tensor of the molecule. The polarizability tensor is, in general, a function of the nuclear coordinates and hence of the molecular vibrational frequencies. Let us consider a single molecule scattering system space-fixed in its equilibrium configuration, but let the nuclei may vibrate about their equilibrium positions. The variation of the polarizability with vibrations of the molecule can be expressed by expanding each component $\alpha_{\rho\sigma}$ of the polarizability tensor α in Taylar series with respect to the normal coordinates of vibration, as follows :

$$\alpha_{\rho\sigma} = (\alpha_{\rho\sigma})_0 + \sum_k \left(\frac{\partial \alpha_{\rho\sigma}}{\partial Q_k}\right)_0 Q_k + \sum_{k,l} \left(\frac{\partial^2 \alpha_{\rho\sigma}}{\partial Q_k Q_l}\right)_0 Q_k Q_l + ..., \tag{A.2}$$

where $(\alpha_{\rho\sigma})_0$ is the value of $\alpha_{\rho\sigma}$ at the equilibrium configuration. $Q_k, Q_l.....$ are the normal coordinates of vibration associated with the molecular vibrational frequencies $\omega_k, \omega_l, ...$ and the summations are over all normal coordinates. The subscript '0' on the derivatives indicates that these are to be taken at the equilibrium configuration. Under the electrical harmonic approximation and considering only the term linear in Q, for one particular normal mode of vibration Q_k, equa-

tion (A.2) can be written as,

$$(\alpha_{\rho\sigma})_k = (\alpha_{\rho\sigma})_0 + \left(\frac{\partial \alpha_{\rho\sigma}}{\partial Q_k}\right)_0 Q_k \tag{A.3}$$

Since this equation is valid for all tensor components, we may write

$$\alpha_k = \alpha_0 + \alpha_k{}' Q_k \tag{A.4}$$

where α_k is a tensor with components $(\alpha_{\rho\sigma})_k$.

Assuming simple harmonic motion, that is mechanical harmonicity, Q_k is given by

$$Q_k = Q_{k_0} \cos(\omega_k t + \delta_k) \tag{A.5}$$

where Q_{k_0} is the motion amplitude and δ_k is a phase factor.

Introducing equation (A.5) in equation (A.4) , we obtain the time-dependence of the polarizability tensor resulting from the k^{th} molecular vibration :

$$\alpha_k = \alpha_0 + \alpha_k{}' Q_{k_0} \cos(\omega_k t + \delta_k) \tag{A.6}$$

Introducing the time dependence for E, $E = E_0 \cos(\omega_l t)$ and for α_k, in equation (A.1), we will obtain:

$$P^{(1)} = \alpha_0 E_0 \cos(\omega_l t) + \alpha_k{}' E_0 Q_{k_0} \cos(\omega_k t + \delta_k) \cos(\omega_l t) \tag{A.7}$$

Using the trigonometric identity

$$\cos A \cos B = \frac{1}{2}[\cos(A + B) \cos(A - B)],$$

we may write $P^{(1)}$ in the form :

$$P^{(1)} = P^{(1)}(\omega_l) + P^{(1)}(\omega_l - \omega_k) + P^{(1)}(\omega_l + \omega_k) \tag{A.8}$$

where

$$P^{(1)}(\omega_l) = \alpha_0 E_0 \cos(\omega_l t) \tag{A.9a}$$

$$P^{(1)}(\omega_l - \omega_k) = \alpha_k{}^{Ram} E_0 \cos[(\omega_l - \omega_k)t + \delta_k] \tag{A.9b}$$

$$P^{(1)}(\omega_l + \omega_k) = \alpha_k{}^{Ram} E_0 \cos[(\omega_l + \omega_k)t + \delta_k] \tag{A.9c}$$

and

$$\alpha_k{}^{Ram} = \frac{1}{2}\alpha_k{}'Q_k,$$

where α_0 and $\alpha_k{}'$ are the polarizability tensor component at equilibrium and the derived polarizability tensor component for a particular normal mode of molecular vibration Q_k at equilibrium respectively.

Appendix B

Spectral compression in periodically poled crystals

In a three wave mixing process where two light waves of optical frequencies ω_1 and ω_2, interact in a second order nonlinear crystal to generate the third light wave at optical frequency $\omega_3 = \omega_1 + \omega_2$, the intensity I_3 of this newly generated beam is given by,

$$I_3 = \alpha\chi^{(2)} I_1 I_2 . L^2 sinc^2(\frac{\Delta kL}{2}) \tag{B.1}$$

where $\alpha = \frac{512\pi^5}{n_1 n_2} n_3 \lambda_3^2 c$ is a constant for a material and the interacting frequencies.

In general, the process is called *sum frequency generation(SFG)*. In the particular case, when $\omega_1 = \omega_2 \equiv \omega_{FF}$ then $\omega_3 = \omega_1 + \omega_2 \equiv 2\omega_{SH}$ and the process is called *second harmonic generation(SHG)*.

The efficiency of the generation of the third beam is typically governed by the factor $sinc^2(\frac{\Delta kL}{2})$, where $\Delta k = k_1 + k_2 - k_3$ is called the *wave-vector mismatch* (in case of SHG, $\Delta k = 2k_\omega - k_{2\omega}$) and L is the interaction length. This implies that efficiency decreases as $|\Delta k|L$ increases and if L is greater than $1/\Delta k$, the ω_3 (In case of SHG, 2ω) wave get out of phase with its driving polarization wave and power starts flowing from ω_3 wave, back into the ω_1 and ω_2 waves (In case of SHG, ω wave). Hence a length

$$L_c = \frac{2}{\Delta k} \tag{B.2}$$

can be defined as *Coherence length* of interaction within which power flows from ω_1 and ω_2 waves to ω_3 wave. The L_c in a crystal in general is very small, because of the dispersion present in the medium for the interacting optical frequencies,

and the birefringence of the crystal is not enough to compensate it for a long interaction length in a normal phase-matching conditions.

Thus for a normal crystal, increasing the crystal length will not increase the SFG (or SHG) power. One can get just maximum efficiency when crystal length is an integral multiple of L_c. This fact is shown by curve(b) in Figure(B.1) for a normal crystal represented by curve(e)the same Figure.

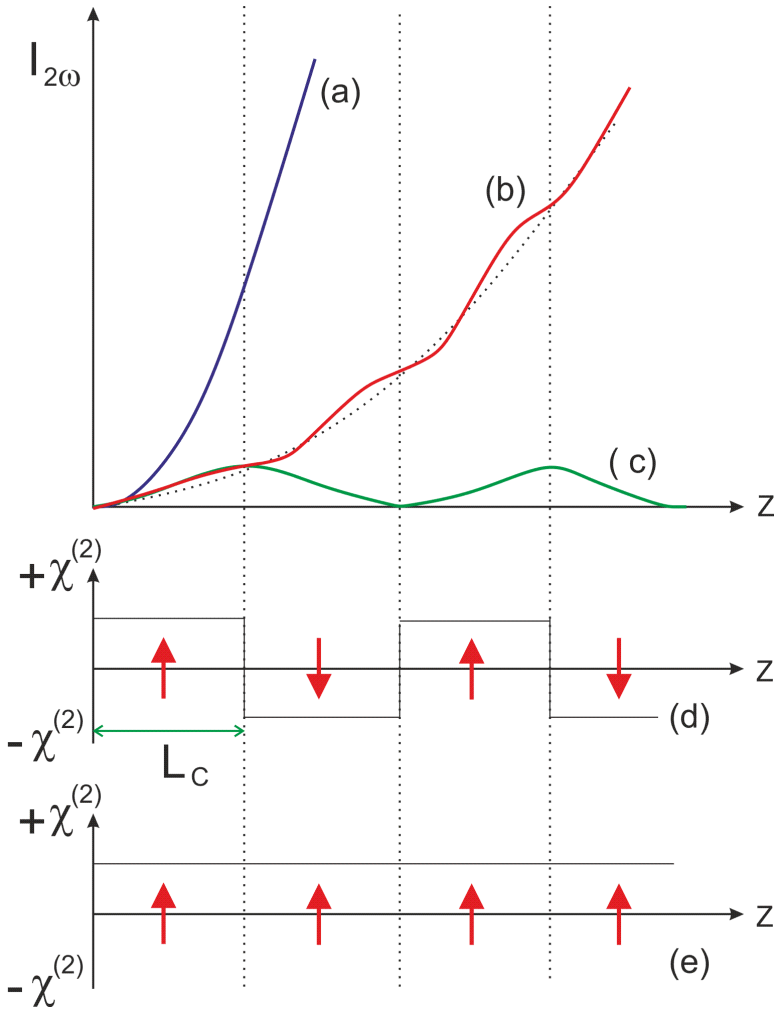


Figure B.1: Graph representing the second harmonic generation with respect to interaction length inside a material:(a)for a perfect phase-matching throughout the interaction length (b)for quasi-phase matching(QPM) (C)for phase-matching in a normal second-harmonic crystal (d)periodic orientation χ^2 in a periodically poled crystal in which QPM is satisfied and (e)χ^2 orientation in a normal second harmonic crystal.

,while the curve(a) in Figure(B.1) refers to an ideal case when perfect phase-matching occurs throughout the interaction length.

But with the help of quasi-phase matching (QPM) technique, it is possible to add constructively the successive coherence lengths in the crystal. QPM uses a periodically poles(PP) crystal, for example periodically poled Lithium Niobate (PPLN),for this purpose. PP crystals are fabricated in such a manner that orientation of the optic axis of the ferroelectric material is inverted periodically as a function of position within the crystal[Graph(d) in Figure(B.1)]. The inversion of the direction of the optic axis inverts the sign of the nonlinear coefficient of the crystal. If the period Λ of the alteration of optic axis direction is set equal to twice the L_c, then each time the field amplitude of the generated wave at the end of L_c is going to decrease as an effect of wave vector mismatch, a reversal of sign of nonlinear coefficient allows the field to continue to grow further. In this way QPM in PP crystals increases the conversion efficiency. This is represented by curve(b) in Figure(B.1).

Further more, SHG process in the presence of high group-velocity-mismatch between the fundamental frequency (FF) and the SH pulse can lead to the efficient generation of narrowband SH pulses starting from broadband FF ones through spectral compression by QMP technique in PP crystals[80; 72]. The spectral compression idea here can be understood as follows:

In general, for SHG, in order to achieve maximum attainable conversion efficiency, following phase matching condition should be satisfied:

$$\Delta k \equiv k(\omega) + k(\omega) - k(2\omega) \tag{B.3}$$

A very narrow portion of broadband FF spectrum satisfies this condition[see Figure(B.2)(a)]. Hence considering only this process conversion efficiency will be very low. But in broadband FF pulse, there are several frequency components $(\omega \pm \Delta\omega)$ which are symmetric with respect to the SH frequency, can give light at frequency 2ω by SFG process $[(\omega + \Delta\omega) + (\omega - \Delta\omega) = 2\omega]$ if the phase matching condition is nearly satisfied for this process, given by:

$$\begin{aligned} \Delta k &= k(\omega + \Delta\omega) + k(\omega - \Delta\omega) - k(2\omega) \\ &\approx k(\omega) + (\frac{\partial k}{\partial \omega})_{FF}\Delta\omega + k(\omega) - (\frac{\partial k}{\partial \omega})_{SH}\Delta\omega - k(2\omega) \\ &\approx [k(\omega) + k(\omega) - k(2\omega)] + [(\frac{\partial k}{\partial \omega})_{FF} - (\frac{\partial k}{\partial \omega})_{SH}]\Delta\omega \end{aligned} \tag{B.4}$$

By equation (B.3), first term will be zero,

$$\begin{aligned}\Delta k &\approx [(\frac{\partial k}{\partial \omega})_{FF} - (\frac{\partial k}{\partial \omega})_{SH}]\Delta\omega \\ &\approx [(\frac{1}{v_{gFF}}) - (\frac{1}{v_{gSH}})]\Delta\omega\end{aligned} \tag{B.5}$$

Equation (B.5) shows that this additional phase-matching condition can be satisfied for a broad spectra of the femtosecond FF spectrum if group velocity mismatch between the FF and SH pulses is quite high for the crystal[see Figure(B.2)(b)]. This SFG process dramatically increases the efficiency of SH signal.

It can be shown that the FWHM bandwidth $\Delta\omega_{SH}$ of the SH pulse is approximately given by[81]:

$$\Delta\omega_{SH} = 0.886\frac{2\pi}{|\delta|L} \tag{B.6}$$

where $\delta = \left(\frac{1}{v_{gFF}}\right) - \left(\frac{1}{v_{gSH}}\right)$

The equation (B.6) recommends that PP crystals, containing following properties:

- high nonlinear coefficient, allowing efficient conversion even with relatively low peak powers.
- high δ values, due to the large material dispersion and to the fact that in quasi-phase-matching the FF and SH are made to interact with the same polarization (parallel to the crystal optical axis).

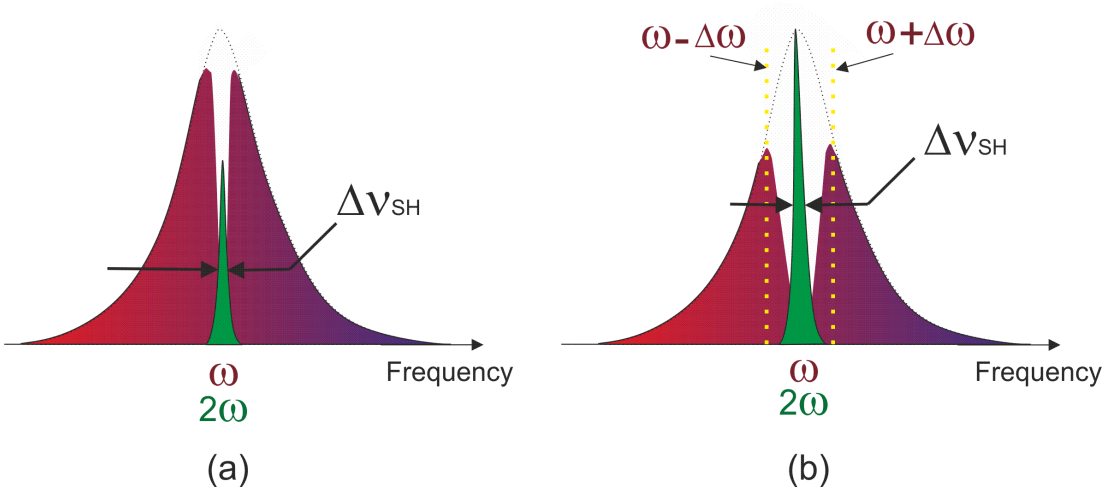


Figure B.2: Representation of phase-matching bandwidth for:(a)normal second harmonic crystal, (b)crystal with high group velocity mismatch and long interaction length.

- absence of spatial walk-off, which allows for the use of relatively long crystals, leading to large compression ratios, combined with tight focusing.

are the best choice for the synthesis of ps pulses, by spectral compression of fs pulses, for CRS microscopy.

Appendix C

Optical Kerr Effect

C.0.1 Kerr Effect

A strong electric field applied to material generates optical anisotropy inside the medium. Hence a single material can be characterized by two values of refractive indices; one is parallel to electric field vector denoted as $n_{\parallel}$ and the other is perpendicular to the applied electric field vector denoted by $n_{\perp}$. Suppose the strong electric field is applied along the X-direction inside the medium, then a linearly polarized (polarized in some direction in XY-plane)light field propagating along the z-direction will experience a phase difference Φ between its parallel to and perpendicular to X-direction components because of experiencing different refractive indices in the two directions. This induced phase-difference is called *birefringence* and is given by the relation:

$$\Phi = \frac{2\pi L}{\lambda}(n_{\parallel} - n_{\perp}) = 2\pi BLE^2, \tag{C.1}$$

where B is a constant, L is path length inside the medium and λ is the wavelength of incident light.

This phenomenon is called *Kerr Effect (OKE)*. Now consider a polarized light beam incident on a medium analyzed through two crossed polarizers placed before and after the medium respectively. In the absence of any applied electric field, no birefringence is induced in the medium and no light is detected after the second polarizer. But when a strong electric filed is applied to the medium, the birefringent induced in the medium partially depolarizes the light, so that an small intensity (I) of the light is detected after the second polarizer, given by:

$$I = I_0 \sin^2 \Phi \tag{C.2}$$

where I_0 is the intensity of the incident light and Φ is the induced phase-shift.

C.0.2 Optical Kerr Effect(OKE)

Optical Kerr Effect is the full optical version of the aforementioned normal Kerr effect. In OKE, the birefringence is induced by the strong electric field (generally available by laser sources) of the electromagnetic radiation incident on the medium. In practice, for OKE, two linearly polarized light at different optical frequencies with their planes of polarization at 45^0 to each other are focused on the sample. Then one of the light beam, usually the stronger one, induces birefringence inside the medium, and the second polarized light beam which falls on the sample through two crossed polarizers placed before and after the sample respectively, experiences a partial depolarization due to the induced birefringence by the first beam. The small intensity of this depolarized light is detected after the second polarizer.

In this way, in the OKE process, four fields are involved; the two fields are the electric field of first beam inducing birefringence (which according to equation C.1 acts as second power), third field is the second beam and the fourth one is the depolarized field which we detect after the second polarizer. This means OKE is the member of family of FWM processes, hence it can also be described like other third-order material responses by third-order induced polarization $P^{(3)}$ given by equation(1.19) as:

$$P_i^{(3)}(\omega_4) \propto \chi_{ijkl}^{(3)} E_j(\omega_1) E_k(\omega_2) E_l(\omega_3) \tag{C.3}$$

Here subscripts i,j,k,l refers to the polarization directions of the electric fields involved in the process.

We can consider an experimental geometry that polarization direction along the second polarizer is along Y-axis and polarization direction along first polarizer is along X-axis. The birefringence-inducing beam we call as *pump* and its electric field is denoted by E_p, and just to utilize the same terminology used in the

previous Chapters, we call the beam probing the birefringence as *Stokes* and its electric field as E_s. So here pump beam is polarized at 45^0 with respect to the X-axis while the Stokes is polarized along the X-axis. And depolarized light due to OKE is observed along polarization along Y-axis. In this geometry pump can be decomposed into two perpendicularly polarized components (having same phase) along X- and Y-axes.

As discussed before, in an isotopic medium, $\chi^{(3)}_{1111}$, $\chi^{(3)}_{1221}$, $\chi^{(3)}_{1212}$, $\chi^{(3)}_{1122}$ are the only non-vanishing independent elements of the third-order susceptibility tensor. With experimental geometry described above, it is possible to induce only two $\chi^{(3)}_{1212}$ and $\chi^{(3)}_{1122}$,generating following two third-order induced polarization components respectively(The numbers 1 and 2 are assigned to Y- and X-directions respectively):

$$P_1^{(3)\prime} \propto \chi^{(3)}_{1212} E_2(\omega_p) E_1(\omega_p) E_2(\omega_s) \tag{C.4a}$$

$$P_1^{(3)\prime\prime} \propto \chi^{(3)}_{1122} E_1(\omega_p) E_2(\omega_p) E_2(\omega_s) \tag{C.4b}$$

The differing element in above two induced third-order polarization components is the permutation of the two polarization components of the input pump beam. These two polarization components of the input pump beam are in phase, hence the two induced third-order polarization component waves are also in phase. They are also in phase with respect to the phase of the pump beam. They interfere constructively and just merely add. Therefore, total polarization in this experimental geometry will be:

$$P_1^{(3)} \propto (P_1^{(3)\prime} + P_1^{(3)\prime\prime}) \tag{C.5a}$$

$$\propto (\chi^{(3)}_{1212} + \chi^{(3)}_{1122}) E_2(\omega_p) E_1(\omega_p) E_2(\omega_s) \tag{C.5b}$$

This polarization is the source of OKE signal at the output of the second polarizer.

As we have already discussed in previous Chapters that far from the resonance with any optical transition, any material have two types of contributions to third-order nonlinear response to the application of three electric fields, which also reflects in microscopic level in the structure of third-order nonlinear susceptibility $\chi^{(3)}$ of the material. So in general $\chi^{(3)}$ has two types of responses:

- A pure electronic contribution which comes from the distortion of electronic clouds of the atoms and the molecules inside the sample. Practically it is instantaneous response and stays only till the duration of the excitation pulses.

- A nuclear contribution which comes from the partial orientation of the molecules in the excitation field and exists whenever molecules possess a non-isotropic polarizability. We can say, the strong excitation field affects the random orientation of the molecules and partially align them in the direction of the excitation fields, which generates a transient birefringence inside the medium. The spontaneous rotational motion of the molecules brings the system back to the isotropic equilibrium position within a time with is characteristic of the rotational dynamics of the molecules. Within this time period, the presence of the molecule can be investigated by probing this birefringence and observing the transmitted Stokes beam intensity through it.

  This nuclear contribution may consist of further following components:

  - An intramolecular vibrational Raman contribution which decay with dephasing time (typically of the order of picosecond)of the molecular vibrations.
  - An intermolecular librational contribution coming from librational motion of the molecule in the cage of the first neighborhood molecule. It decays very fast (typically of the order of less than 200 fs) due to inhomogeneous dephasing in the sample environment.
  - Another intermolecular contribution coming from density fluctuation and hence correlated to the collision-induced anisotropy of the molecular polarizability. It relaxes by the life-time of the local structure in the sample(very fast of the order of few hundreds of fs).
  - A rotational contribution of which life-time can span a wide range of values(few ps to several nanoseconds), depending on the size of molecules and the viscosity

Therefore each tensor element of $\chi^{(3)}$ in general have following kind of structure:

$$\chi^{(3)}_{ijkl} \propto (\chi^{(3)Nuclear Intermolecular}_{ijkl} + \chi^{(3)Electronic}_{ijkl}) + \chi^{(3)Nuclear Intramolecular,Raman}_{ijkl} \quad \text{(C.6)}$$

Now the third term in equation (C.6)can dominate if vibrational Raman mode Ω is in resonance with frequency detuning $(\omega_p - \omega_s)$of the pump and the Stokes beams. Thus when frequency-difference between pump and Stokes $(\omega_p - \omega_s)$ matches with the Raman active vibrational frequency of the molecule Ω, we mainly observe the Coherent Raman contribution in the OKE experiment. And then this phenonenon is called *Raman Induced Kerr Effect(RIKE).*

For RIKE spectroscopy, the first and second terms are real and have no chemical specific information of the molecule, and therefore they are undesired. The same type of these real contributions may also come from the other type of molecules present inside the sample(for example substrate molecules) which can give non-resonant background to the RIKE signal. The third term being resonant intramolecular is imaginary. Hence each $\chi^{(3)}_{ijkl}$ component can be written in the following familiar from:

$$\chi^{(3)}_{ijkl} \propto (\chi^{(3)R,Re}_{ijkl} + i\chi^{(3)R,Im}_{ijkl}) + \chi^{(3)NR,Re}_{ijkl} \quad \text{(C.7)}$$

where NR part of the $\chi^{(3)}$(the third term in equation(C.7)), is the source of NRB. Different components of $\chi^{(3)}_{ijkl}$ can be selected by employing different types of detection schemes in RIKE experiments.

Appendix D

Optical Heterodyne Detection

Optically Heterodyne Detection is a standard technique used in spectroscopy field. It is used to amplify small signals. A small homodyne signal ΔA_s interferes with a coherent field, at the same frequency and polarization of the signal field, called *local oscillator (LO)*. The overall intensity detected on photodetector is given as:

$$I = |\Delta A_s + A_{LO}|^2 \tag{D.1a}$$

$$= |\Delta A_s|^2 + |A_{LO}|^2 + 2Re[\Delta A_s].Re[A_{LO}] + 2Im[\Delta A_s].Im[A_{LO}] \tag{D.1b}$$

If amplitude of LO field is kept quite high as compared to the signal field i.e. $|A_{LO}| \ggg |\Delta A_s|$, the first term in equation (D.1b) will be negligible as compared to rest of three terms.

In addition, if the detection is done by modulating the pump field (i.e. the generator of signal field ΔA_s)and detecting the modulation transfer at the signal field through lock-in detection (this is called modulation transfer technique), the strong LO field term (that is the second term in equation (D.1b)) is also rejected. Then we detect only the following interferometric terms:

$$I = 2Re[\Delta A_s].Re[A_{LO}] + 2Im[\Delta A_s].Im[A_{LO}] \tag{D.2}$$

The phase of the LO field ($A_{LO} = Re[A_{LO}]+iIm[A_{LO}]$) can be set with respect to the signal field to get either $Re[A_{LO}] = 0$ or $Im[A_{LO}] = 0$ and in this way we probe the $Im[\Delta A_s]$ or $Re[\Delta A_s]$ each amplified by the LO field respectively.

Source of LO field:

We have discussed **Interferometric CARS** in Chapter 2. I-CARS utilizes the heterodyne detection scheme combined with modulation transfer technique. There the LO field at the anti-Stokes frequency (ω_{as}) is generated by a third phase-coherent independent beam and the phase of the LO field is varied to detect the CARS signal proportional to the real and imaginary component of the $\chi^{(3)}_{1111}$ and to suppress the NRB. This experimental situation is a bit tricky because it requires generation of a third phase-coherent beam with precise phase control mechanism and then to deal with three beams onto the sample.

Furthermore in all the coherent Raman spectroscopy experiments, the homodyne field A_{ω_4} is generated by the radiation from induced third-order polarization $P^{(3)}_{\omega_4}$. From equation (1.43), it is clear that A_{ω_4} is at 90^0 phase with respect to the $P^{(3)}_{\omega_4}$. Mathematically this fact can be written as:

$$A_{\omega_4} \propto -i[P^{(3)}_{\omega_4}] \tag{D.3a}$$

$$A_{\omega_4} \propto -i[\chi^{(3)}_{eff}].A_{\omega_1}.A_{\omega_2}.A_{\omega_3} \tag{D.3b}$$

$$Re[A_{\omega_4}] + iIm[A_{\omega_4}] \propto -i[\chi^{(3)}_{Real} + i\chi^{(3)}_{Imaginary}].A_{\omega_1}.A_{\omega_2}.A_{\omega_3} \tag{D.3c}$$

Comparing real and imaginary parts on both sides of equation (D.3), we have:

$$Re[A_{\omega_4}] \propto Im[\chi^{(3)}_{eff}].A_{\omega_1}.A_{\omega_2}.A_{\omega_3} \tag{D.4a}$$

$$Im[A_{\omega_4}] \propto -Re[\chi^{(3)}_{eff}].A_{\omega_1}.A_{\omega_2}.A_{\omega_3} \tag{D.4b}$$

Therefore the detected intensity in equation (D.2) transforms into

$$I = 2Re[A_{\omega_4}].Re[A_{LO}] + 2Im[A_{\omega_4}].Im[A_{LO}] \tag{D.5a}$$

$$\propto (2Im[\chi^{(3)}_{eff}]Re[A_{LO}] - 2Re[\chi^{(3)}_{eff}]Im[A_{LO}]).A_{\omega_1}.A_{\omega_2}.A_{\omega_3} \tag{D.5b}$$

In SRS, intrinsic heterodyne detection takes place between the generated SRG (or SRL) and the transmitted input Stokes (or pump) beam. Therefore, for SRS,

$A_{\omega_4} \equiv \Delta A_s \equiv SRG$ and $A_{LO} \equiv A_s$. And

$$\chi^{(3)}_{eff} \equiv \chi^{(3)}_{1111} = Re[\chi^{(3)R}_{1111} + \chi^{(3)NR}_{1111}] + iIm[\chi^{(3)R}_{1111}] \tag{D.6}$$

Equation (D.4)takes the form for SRS as:

$$Re[\Delta A_s] \propto Im[\chi^{(3)R}_{1111}].A_p.A_s.A_p \tag{D.7a}$$

$$Im[\Delta A_s] \propto -Re[\chi^{(3)R}_{1111} + \chi^{(3)NR}].A_p.A_s.A_p \tag{D.7b}$$

And the detected intensity in equation (D.2) for SRS transforms as:

$$I = 2Re[\Delta A_s].Re[A_{LO}] + 2Im[\Delta A_s].Im[A_{LO}] \tag{D.8a}$$

$$= 2Im[\chi^{(3)R}_{1111}].A_p.A_s.A_p.Re[A_s] - 2Re[\chi^{(3)R}_{1111} + \chi^{(3)NR}].A_p.A_s.A_p.Im[A_s] \tag{D.8b}$$

In SRS both frequency and polarization of generated SRG are in phase with transmitted Stokes beam.Hence inherently $Im[A_{LO}] \equiv Im[A_s] = 0$. This makes second term in equation (D.8b) identically zero. It implies that in SRS, heterodyne detection probes for following signal:

$$I = 2Im[\chi^{(3)R}_{1111}].A_p.A_s.A_p.[A_s] \tag{D.9a}$$

$$= 2Im[\chi^{(3)R}_{1111}].I_p.I_s \tag{D.9b}$$

That means SRS probes directly $Im[\chi^{(3)R}_{1111}]$ getting rid of NRB no matter whether it is present in the sample or not. But SRS has no facility to probe $Re[\chi^{(3)R}_{1111}]$ component. Hence SRS although good for chemical imaging, yet does not give complete information.

Optically heterodyne detection RIKE has the capability to probe different components of $\chi^{(3)}$. We will discuss this technique in Chapter 5.

Appendix E

Effect of waveplate and Wollaston prism on polarized light

In this supporting Chapter, a balanced detection output of a configuration consisting of: a wave plate, a Wollaston prism and balanced detector will be presented.

Waveplates alter the polarization state of a light wave traveling through it, by shifting the phase between two perpendicularly polarized components of the light wave. A typical wave plate is simply a birefringent crystal with carefully cut their crystal axis and chosen crystal thickness. The crystal is cut so that the optic axis (extraordinary axis) is parallel to the surfaces of the plate. Light wave polarized along this axis travels through the crystal at a different speed than light wave polarized perpendicular to it(along the ordinary axis), creating a phase difference between them. Depending on the material, the extraordinary refractive index can be greater or smaller than the ordinary one. The waveplate is characterized by the amount of relative phase, ϕ, that it generates on the two components, which is related to the birefringence Δn and the thickness L of the crystal by the following formula:

$\phi = \frac{2\pi \Delta n L}{\lambda}$

A quarter-wave plate creates a quarter-wavelength ($\lambda/4$) phase shift($\phi = \pi/2$) and can change linearly polarized light to circularly polarized light and vice versa by setting the angle between the optic axis of the waveplate and the linear polarization of the incident light wave to 45^0. A half-wave plate retards one polarization component by a half a wavelength ($\lambda/2$) and hence it introduces phase

shift of π. In this way, a linearly polarized light when incident upon it with its polarization direction making an angle of 22.5^0 with respect to the crystals optic axis, produces an outgoing light wave transformed into another linearly polarized light with its polarization direction at 45^0 with respect to the optic axis of the crystal.

The Wollaston prism is made up of two right birefringent prisms with perpendicular optic axes. As the light wave travels into the first prism, the two polarization components experience a different refractive index. Then, at the interface of the two prisms, the refractive indices experienced by the different polarization components change: the component traveling in the first prism along the ordinary axis travels along the extraordinary one in the second prism, and vice versa. Both components experience a refraction with different and opposite angles, so the two beams diverge from the prism in different directions, giving two linearly polarized beams with their polarization directions orthogonal to each other. Thus Wollaston prism separates the two polarizations.

Our balanced detection setup consists of a waveplate(HWP or QWP) followed by a Wollaston prism, and the outputs of Wollaston prism fall on twin photodiodes of a balanced detector[Figure(E.1)]. Balanced detector reads the difference

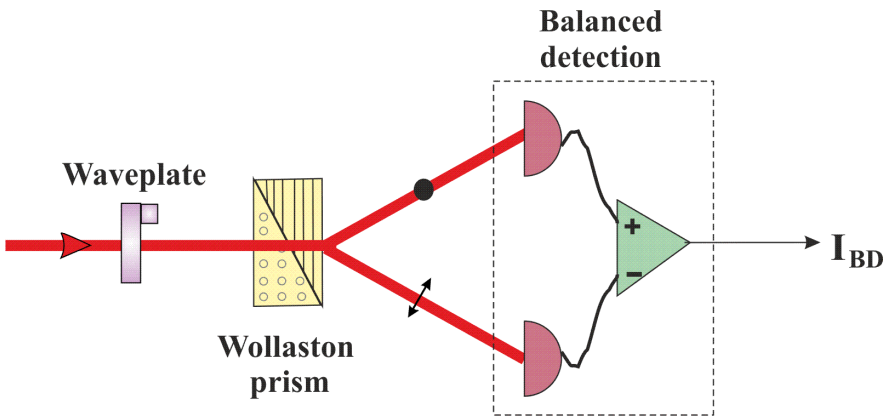


Figure E.1: Balanced detection with a waveplate and a Wollaston prism

between the intensities of the two outputs and gives output current proportional to this intensity difference multiplied by its internal gain. In the RIKE experiment when the pump is off, only Stokes beam is falling on the sample, HWP or QWP in front of the Wollaston is rotated in such a way that the two polarized

beams coming out of the Wollaston are equal in intensity. The balanced detector output is zero in this case. Now when pump (either polarized at 45^0 or circularly polarized in linear RIKE or Circular RIKE respectively) is also on with pump-Stokes frequency difference tuned to some Raman vibrational resonance of the sample, it creates birefringence in the sample and due to RIKE, Stokes polarization rotates slightly which generates intensity difference between the two beams coming out the Wollaston prism. It is our BD-RIKES signal which is detected by the balanced detector. Now we will see mathematically which physical quantity we measure at the output and what difference is made by the choice of HWP or QWP in front of Wollaston prism in it.

E.1 Half waveplate and Wollaston prism

E.1.1 Calculations for aligning the balanced detection setup: In absence of pump

Suppose a linearly polarized light field (let say in our case, Stokes field) incident on a waveplate (HWP or QWP). For simplicity, initially let us assume that polarization direction of the incident Stokes field is along X-axis where XY-axes are the laboratory frame of reference. The waveplate axes ($X'Y'$-axes, where Y' is the fast axis of the waveplate) are at α angle with respect to the laboratory axes [Figure(E.2)(a)].

Let us consider the incident field(here the Stokes field) in the laboratory frame of reference, as:

$$E_x = A_x e^{i\omega t} \tag{E.1}$$

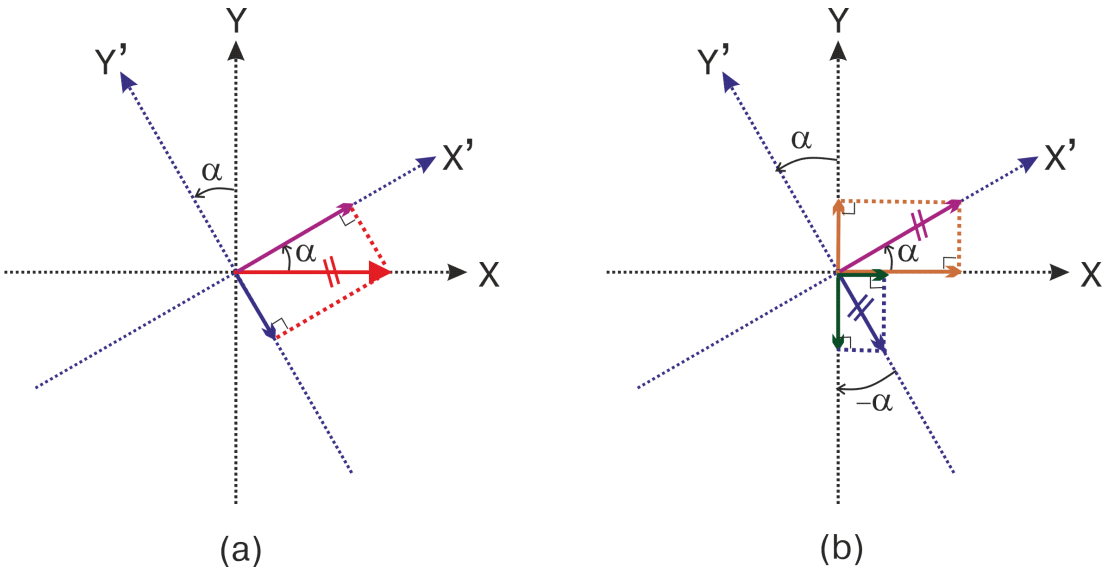


Figure E.2: Polarization scheme in balanced detection with waveplate and Wollaston prism, when pump is off (a) projection on waveplate axes in detection, (b) projection on Wollaston axes.

Projection on waveplate axes:

$$\begin{aligned} E_{xx'} &= E_x \cos\alpha = A_x e^{i\omega t}.\cos\alpha \\ E_{xy'} &= -E_x \sin\alpha = -A_x e^{i\omega t}.\sin\alpha \end{aligned} \tag{E.2}$$

After passing through HWP, electric fields become:

$$\begin{aligned} E_{xx'} &= A_x e^{i\omega t}.\cos\alpha \\ E_{xy'} &= -A_x e^{i\omega t}.\sin\alpha.e^{i\pi} \end{aligned} \tag{E.3}$$

Projecting these fields on Wollaston prism axes which are aligned on laboratory axes[Figure(E.2)(b)]:

$$\begin{aligned} F_x &= E_{xx'}\cos\alpha - E_{xy'}.\sin\alpha \\ &= A_x e^{i\omega t}.\cos^2\alpha - A_x e^{i\omega t}.\sin^2\alpha \\ &= A_x e^{i\omega t}.(\cos^2\alpha - \sin^2\alpha) \\ &= A_x e^{i\omega t}.\cos 2\alpha \end{aligned} \tag{E.4}$$

$$\begin{aligned} F_y &= E_{xx'}\sin\alpha + E_{xy'}.\cos\alpha \\ &= A_x e^{i\omega t}.\cos\alpha.\sin\alpha + A_x e^{i\omega t}.\sin\alpha.\cos\alpha \\ &= A_x e^{i\omega t}.2.\sin\alpha.\cos\alpha \\ &= A_x e^{i\omega t}.\sin 2\alpha \end{aligned} \tag{E.5}$$

where F_x and F_y are the fields coming out from the two branches of the Wollaston prism. The average intensities of these two fields are:

$$\begin{aligned} < |F_x|^2 > =< |A_x.\cos 2\alpha|^2 >= |A_x|^2.\cos^2(2\alpha) \\ < |F_y|^2 > =< |A_x.\sin 2\alpha|^2 >= |A_x|^2.\sin^2(2\alpha) \end{aligned} \tag{E.6}$$

In absence of the pump, to align the detector, these two intensities are to be balanced, that means:

$$\begin{aligned} < |F_x|^2 > =< |F_y|^2 > \\ \Rightarrow \cos^2(2\alpha) = \sin^2(2\alpha) \\ \Rightarrow \tan^2(2\alpha) = 1 \\ \Rightarrow \tan^(2\alpha) = \pm 1 \\ \Rightarrow 2\alpha = \frac{\pi}{4} + k\frac{\pi}{2} \\ \Rightarrow \alpha = \frac{\pi}{8} + k\frac{\pi}{4} \end{aligned} \tag{E.7}$$

where $k = 0, \pm 1, \pm 2, ...$

This indicates, HWP should be rotated by 22.5^0 with respect to the laboratory axis to balanced the detector in absence of the pump.

E.1.2 Calculations for balanced detection RIKE signal:pump is ON

When pump and Stokes both are on and their frequency difference is tuned to a vibrational resonance of the sample, intense pump generates birefringence inside the sample. Due to this Raman induced birefringence, Stokes polarization slightly rotates. Let us assume the Stokes polarization is rotated by θ angle with respect to its initial polarization direction i.e. laboratory X-axis[As shown in Figure(E.3)].

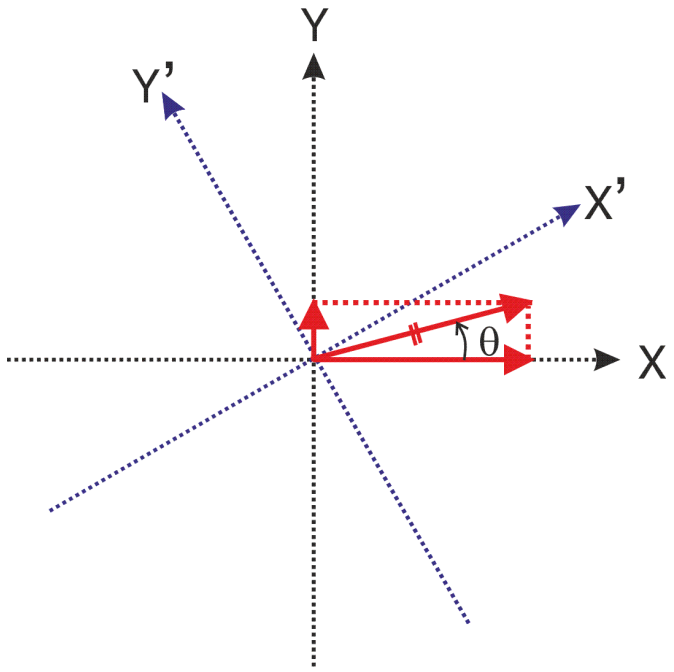


Figure E.3: Projection of the rotated Stokes polarization, due to RIKE on laboratory axes; XY-axes are laboratory axes and $X'Y'$-axes are the waveplate axes.

We will represent this rotated Stokes field by:

$$E = Ae^{i\omega t} \tag{E.8}$$

Let us decompose this input field in laboratory frame of reference as:

$$\begin{aligned} E_x &= E\cos\theta = A\cos\theta e^{i\omega t} \equiv A_x e^{i\omega t} \\ E_y &= E\sin\theta = A\sin\theta e^{i\omega t} \equiv A_y e^{i\omega t} \end{aligned} \tag{E.9}$$

These E_x and E_y fall on the waveplate. Now we will observe separately the effect of waveplate plus Wollaston on these two components and then combine them together.

$\boldsymbol{E}_x field$:

Here input field is $E_x = A_x e^{i\omega t}$ and waveplate axes are at α angle with respect to the laboratory frame. Effect of HWP plus Wollaston is exactly the same as we discussed in obtaining equations(E.4) and (E.5),therefore the fields at Wollaston output is given by [Figure E.4(1a) and (1b)]:

$$\begin{aligned} F_x &= A_x e^{i\omega t}.\cos 2\alpha \\ F_y &= A_x e^{i\omega t}.\sin 2\alpha \end{aligned} \tag{E.10}$$

$\boldsymbol{E}_y field$:

Here input field is $E_y = A_y e^{i\omega t}$ and waveplate axes are at α angle with respect to the laboratory frame.

Projection on waveplate axes[Figure E.4(2a)]:

$$\begin{aligned} E_{yx'} &= E_y \sin\alpha = A_y e^{i\omega t}.\sin\alpha \\ E_{yy'} &= E_y \cos\alpha = A_y e^{i\omega t}.\cos\alpha \end{aligned} \tag{E.11}$$

After passing through HWP, electric fields become:

$$\begin{aligned} E_{yx'} &= A_y e^{i\omega t}.\sin\alpha \\ E_{yy'} &= A_y e^{i\omega t}.\cos\alpha.e^{i\pi} = -A_y e^{i\omega t}.\cos\alpha \end{aligned} \tag{E.12}$$

Projecting these fields on Wollaston prism axes which are aligned on laboratory axes[Figure E.4(2b)]:

$$\begin{aligned} G_x &= E_{yx'}\cos\alpha - E_{yy'}.\sin\alpha \\ &= A_y e^{i\omega t}.\sin\alpha\cos\alpha + A_y e^{i\omega t}.\sin\alpha\cos\alpha \\ &= A_y e^{i\omega t}.(2.\sin\alpha\cos\alpha) \\ &= A_y e^{i\omega t}.\sin 2\alpha \end{aligned} \tag{E.13}$$

$$\begin{aligned} G_y &= E_{yx'}\sin\alpha + E_{yy'}.\cos\alpha \\ &= A_y e^{i\omega t}.\sin^2\alpha - A_y e^{i\omega t}.\cos^2\alpha \\ &= -A_y e^{i\omega t}.(\cos^2\alpha - \sin^2\alpha) \\ &= -A_y e^{i\omega t}.\cos 2\alpha \end{aligned} \tag{E.14}$$

Here F_x, F_y, G_x and G_y are the fields coming out at the two branches of the Wollaston prism. The total fields on the two branches separately are:

$$\begin{aligned} H_x &= F_x + G_x = A_x e^{i\omega t}.\cos 2\alpha + A_y e^{i\omega t}.\sin 2\alpha = [A_x.\cos 2\alpha + A_y.\sin 2\alpha]e^{i\omega t} \\ H_y &= F_y + G_y = A_x e^{i\omega t}.\sin 2\alpha - A_y e^{i\omega t}.\cos 2\alpha = [A_x.\sin 2\alpha - A_y.\cos 2\alpha]e^{i\omega t} \end{aligned} \tag{E.15}$$

Now we consider the case when the two channels were already balanced in the absence of the pump field. This condition is given by equation(E.7) i.e.

$$2\alpha = \frac{\pi}{4} + k\frac{\pi}{2} \tag{E.16}$$

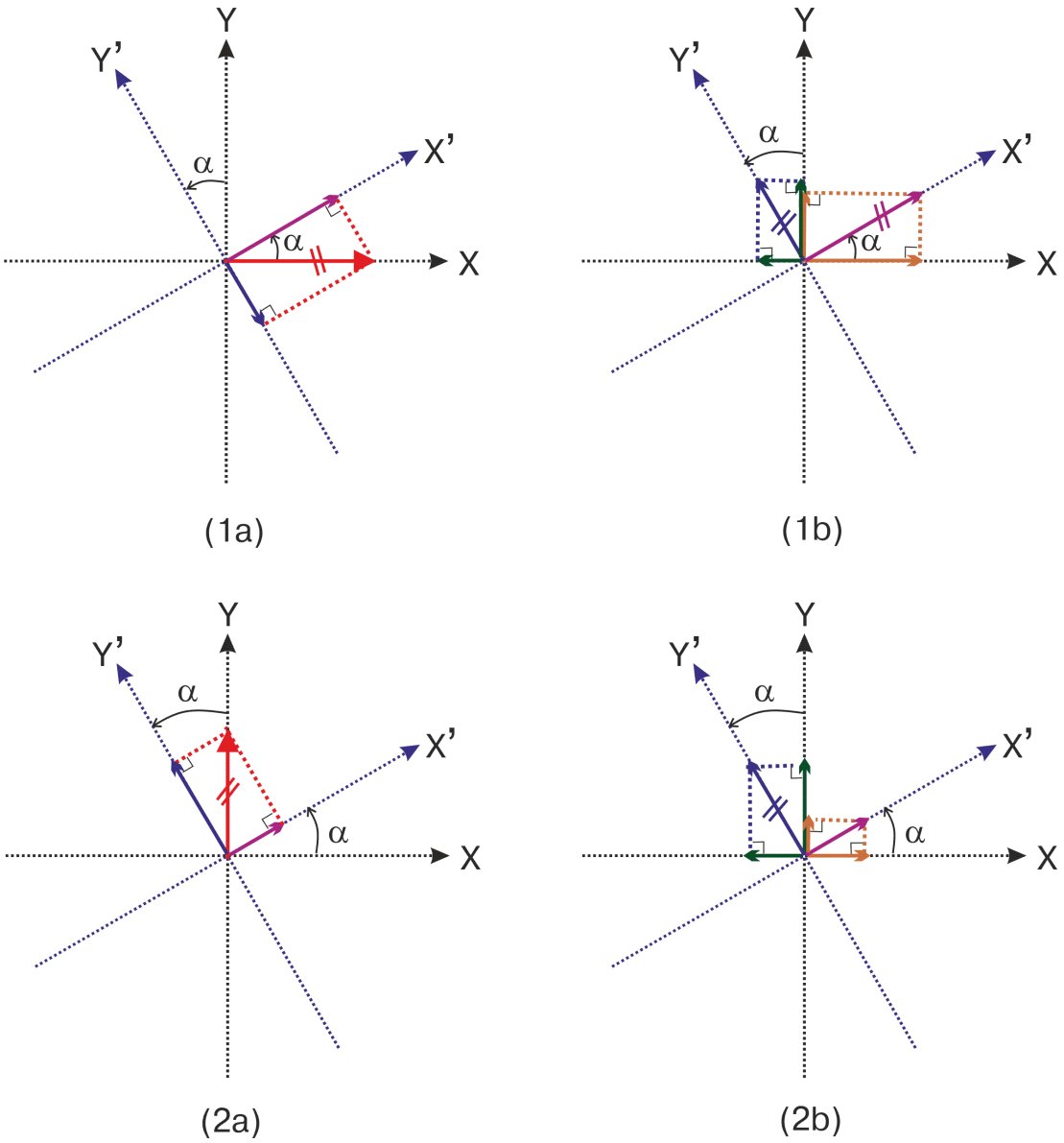


Figure E.4: Polarization scheme in balanced detection with waveplate and Wollaston prism when pump in on;(1a) and (2a):projection on waveplate axes of X- and Y-components of the field respectively, (1b) and (2b): projection on Wollaston axes of the field components.

where $k = 0, \pm 1, \pm 2, ...$

Considering these values of α in equations (E.15), two waveplate positions are possible:

(1) $cos2\alpha = sin2\alpha \Rightarrow 2\alpha = \frac{\pi}{4} + k\pi$

(2) $cos2\alpha = -sin2\alpha \Rightarrow 2\alpha = -\frac{\pi}{4} + k\pi$

Configuration(1): $2\alpha = \frac{\pi}{4} + k\pi$

$$\begin{aligned} H_x &= \frac{1}{\sqrt{2}}[A_x + A_y]e^{i\omega t} \\ H_y &= \frac{1}{\sqrt{2}}[A_x - A_y]e^{i\omega t} \end{aligned} \tag{E.17}$$

The intensities due to above fields are:

$$\begin{aligned} < |H_x|^2 > &=< |(H_x)(H_x)^*| > \\ &= \frac{1}{\sqrt{2}}[A_x + A_y].\frac{1}{\sqrt{2}}[A_x^* + A_y^*] \\ &= \frac{1}{2}[|A_x|^2 + A_x.A_y^* + A_y.A_x^* + |A_y|^2] \\ &= \frac{1}{2}[|A_x|^2 + |A_y|^2 + 2Re(A_x.A_y^*)] \\ < |H_y|^2 > &=< |(H_y)(H_y)^*| > \\ &= \frac{1}{\sqrt{2}}[A_x - A_y].\frac{1}{\sqrt{2}}[A_x^* - A_y^*] \\ &= \frac{1}{2}[|A_x|^2 - A_x.A_y^* - A_y.A_x^* + |A_y|^2] \\ &= \frac{1}{2}[|A_x|^2 + |A_y|^2 - 2Re(A_x.A_y^*)] \end{aligned} \tag{E.18}$$

Hence the intensity difference between the two channels is :

$$< |H_x|^2 > - < |H_y|^2 >= 2Re(A_x.A_y^*)] \tag{E.19}$$

This is our BD-RIKE signal.

Configuration(2):$2\alpha = -\frac{\pi}{4} + k\pi$

$$\begin{aligned} H_x &= \frac{1}{\sqrt{2}}[A_x - A_y]e^{i\omega t} \\ H_y &= -\frac{1}{\sqrt{2}}[A_x + A_y]e^{i\omega t} \end{aligned} \tag{E.20}$$

Performing the similar calculations as we did for configuration(1), we will arrive at the result:

$$< |H_x|^2 > - < |H_y|^2 >= -2Re(A_x.A_y^*)] \tag{E.21}$$

Equations (E.19) and (E.21) differ only in negative sign which means that in one configuration X-polarized intensity is higher than the Y-polarized one while in other configuration it is just opposite, but they are equal in magnitude.

E.2 Quarter waveplate and Wollaston prism

E.2.1 Calculations for aligning the balanced detection setup: In absence of pump

Suppose a linearly polarized Stokes field incident on the QWP. For simplicity, initially let us assume that polarization direction of the incident Stokes field is along X-axis where XY-axes are the laboratory frame of reference. The waveplate axes ($X'Y'$-axes, where Y' is the fast axis of the waveplate) are at α angle with respect to the laboratory axes [Figure(E.2)(a)].

Let us consider the incident field in the laboratory frame of reference as:

$$E_x = A_x e^{i\omega t} \tag{E.22}$$

Projection on QWP axes:

$$\begin{aligned} E_{xx'} &= E_x \cos\alpha = A_x e^{i\omega t}.\cos\alpha \\ E_{xy'} &= -E_x \sin\alpha = -A_x e^{i\omega t}.\sin\alpha \end{aligned} \tag{E.23}$$

After passing through QWP, electric fields become:

$$\begin{aligned} E_{xx'} &= A_x e^{i\omega t}.\cos\alpha \\ E_{xy'} &= -A_x e^{i\omega t}.\sin\alpha.e^{i\pi/2} \end{aligned} \tag{E.24}$$

Projecting these fields on Wollaston prism axes which are aligned on laboratory axes[Figure(E.2)(b)]:

$$\begin{aligned} F_x &= E_{xx'}\cos\alpha - E_{xy'}.\sin\alpha \\ &= A_x e^{i\omega t}.\cos^2\alpha + A_x e^{i\omega t}.e^{i\pi/2}.\sin^2\alpha \\ &= A_x e^{i\omega t}.(\cos^2\alpha + e^{i\pi/2}.\sin^2\alpha) \end{aligned} \tag{E.25}$$

$$\begin{aligned} F_y &= E_{xx'}\sin\alpha + E_{xy'}.\cos\alpha \\ &= A_x e^{i\omega t}.\cos\alpha.\sin\alpha - A_x e^{i\omega t}.e^{i\pi/2}.\sin\alpha.\cos\alpha \\ &= A_x e^{i\omega t}.(1 - e^{i\pi/2}).\sin\alpha.\cos\alpha \end{aligned} \tag{E.26}$$

where F_x and F_y are the fields coming out at the two branches of the Wollaston

prism. The average intensities of these two fields are:

$$\begin{aligned}
< |F_x|^2 > &=< |A_x.(\cos^2\alpha + e^{i\pi/2}.\sin^2\alpha)|^2 >= |A_x|^2.(\cos^2\alpha + e^{i\pi/2}.\sin^2\alpha) \\
&\quad (\cos^2\alpha + e^{i\pi/2}.\sin^2\alpha)^* \\
&= |A_x|^2.[\cos^4\alpha + \sin^2\alpha.\cos^2\alpha e^{i\pi/2} + \sin^2\alpha.\cos^2\alpha e^{-i\pi/2} + \sin^4\alpha] \\
&= |A_x|^2.[\cos^4\alpha + \sin^4\alpha] \\
< |F_y|^2 > &=< |A_x.(1 - e^{i\pi/2}).\sin\alpha.\cos\alpha|^2 > \\
&= |A_x|^2.((1 - e^{i\pi/2})\sin\alpha.\cos\alpha).((1 - e^{-i\pi/2})\sin\alpha.\cos\alpha) \\
&= |A_x|^2.\sin^2\alpha.\cos^2\alpha.(1 - e^{i\pi/2} + 1 - e^{-i\pi/2}) \\
&= |A_x|^2.2.\sin^2\alpha.\cos^2\alpha
\end{aligned} \tag{E.27}$$

In absence of the pump, to align the detector, these two intensities are to be balanced, that means:

$$\begin{aligned}
< |F_x|^2 > &=< |F_y|^2 > \\
\Rightarrow \cos^4\alpha + \sin^4\alpha &= 2.\sin^2\alpha.\cos^2\alpha \\
\Rightarrow \cos^2\alpha.(1 + \tan^4\alpha - 2\tan^2\alpha) &= 0
\end{aligned} \tag{E.28}$$

Now $\cos^2\alpha \neq 0$, because it cannot be solution. Then $(\tan^2\alpha - 1)^2 = 0 \Rightarrow \tan\alpha = \pm 1 \Rightarrow \alpha = \frac{\pi}{4} + k\frac{\pi}{2}$ Where $k = 0, \pm 1, \pm 2, ...$

This indicates, QWP should be rotated by 45^0 with respect to the laboratory axis to balance the detector in absence of the pump.

E.2.2 Calculations for balanced detection RIKE signal:pump is ON

When the pump and the Stokes both are on and their frequency difference is tuned to a vibrational resonance of the sample, intense pump generates birefringence inside the sample. Due to this Raman induced birefringence, Stokes polarization slightly rotates. Let us assume Stokes polarization is rotated by θ angle with respect to its initial polarization direction i.e. laboratory X-axis[As shown in Figure(E.3)]. We will represent this rotated Stokes field by:

$$E = Ae^{i\omega t} \tag{E.29}$$

Let us decompose this input field in laboratory frame of reference as:

$$\begin{aligned} E_x &= E\cos\theta = A\cos\theta e^{i\omega t} \equiv A_x e^{i\omega t} \\ E_y &= E\sin\theta = A\sin\theta e^{i\omega t} \equiv A_y e^{i\omega t} \end{aligned} \tag{E.30}$$

These E_x and E_y fall on the QWP. Now we will observe separately the effect of QWP plus Wollaston on these two components and then combine them together.

$\boldsymbol{E}_x field$:

Here input field is $E_x = A_x e^{i\omega t}$ and waveplate axes are at α angle with respect to the laboratory frame. Effect of QWP plus Wollaston will be exactly the same as we discussed in obtaining equations(E.25)and (E.26), therefore the fields at Wollaston output is given by[Figure E.4(1a) and (1b)]:

$$\begin{aligned} F_x &= A_x e^{i\omega t}.(\cos^2\alpha + e^{i\pi/2}.\sin^2\alpha) \\ F_y &= A_x e^{i\omega t}.(1 - e^{i\pi/2}).\sin\alpha.\cos\alpha \end{aligned} \tag{E.31}$$

$\boldsymbol{E}_y field$:

Here input field is $E_y = A_y e^{i\omega t}$ and waveplate axes are at α angle with respect to the laboratory frame.

Projection on waveplate axes[Figure E.4(2a)]:

$$\begin{aligned} E_{yx'} &= E_y\sin\alpha = A_y e^{i\omega t}.\sin\alpha \\ E_{yy'} &= E_y\cos\alpha = A_y e^{i\omega t}.\cos\alpha \end{aligned} \tag{E.32}$$

After passing through HWP, electric fields become:

$$\begin{aligned} E_{yx'} &= A_y e^{i\omega t}.\sin\alpha \\ E_{yy'} &= A_y e^{i\omega t}.\cos\alpha.e^{i\pi/2} \end{aligned} \tag{E.33}$$

Projecting these fields on Wollaston prism axes which are aligned on laboratory axes[Figure E.4(2b)]:

$$\begin{aligned} G_x &= E_{yx'}\cos\alpha - E_{yy'}.\sin\alpha \\ &= A_y e^{i\omega t}.\sin\alpha\cos\alpha - A_y e^{i\omega t}.e^{i\pi/2}.\sin\alpha\cos\alpha \\ &= A_y e^{i\omega t}.(1 - e^{i\pi/2}).\sin\alpha\cos\alpha) \end{aligned} \tag{E.34}$$

$$\begin{aligned} G_y &= E_{yx'}\sin\alpha + E_{yy'}.\cos\alpha \\ &= A_y e^{i\omega t}.\sin^2\alpha + A_y e^{i\omega t}.e^{i\pi/2}.\cos^2\alpha \\ &= A_y e^{i\omega t}.(\sin^2\alpha + e^{i\pi/2}.\cos^2\alpha) \end{aligned} \tag{E.35}$$

Here F_x, F_y, G_x and G_y are the fields coming out from the two branches of the Wollaston prism. The total fields on the two branches separately are:

$$\begin{aligned} H_x = F_x + G_x = [A_x.(\cos^2\alpha + e^{i\pi/2}.\sin^2\alpha) \\ + A_y.(1 - e^{i\pi/2}).\sin\alpha\cos\alpha]e^{i\omega t} \\ H_y = F_y + G_y = [A_x.(1 - e^{i\pi/2}).\sin\alpha.\cos\alpha \\ + A_y.(\sin^2\alpha + e^{i\pi/2}.\cos^2\alpha)].e^{i\omega t} \end{aligned} \tag{E.36}$$

Now we consider the case when the two channels were balanced in the absence of the pump field. This condition is given by the consequence of equation(E.28) i.e. $\Rightarrow \alpha = \frac{\pi}{4} + k\frac{\pi}{2}$ where $k = 0, \pm1, \pm2, ...$

With different values of k, the following two configurations(two QWP positions) are possible:

Configuration(1):$2\alpha = \frac{\pi}{4} + k\pi$

$$\begin{aligned} H_x = \frac{1}{2}[A_x.(1+i) + A_y.(1-i)]e^{i\omega t} \\ H_y = \frac{1}{2}[A_x.(1-i) + A_y.(1+i)]e^{i\omega t} \end{aligned} \tag{E.37}$$

The intensities due to above fields are:

$$\begin{aligned} < |H_x|^2 > &=< |(H_x)(H_x)^*| > \\ &= \frac{1}{4}[A_x.(1+i) + A_y.(1-i)].[A_x^*.(1-i) + A_y^*.(1+i)] \\ &= \frac{1}{2}[|A_x|^2 + i.(A_x.A_y^* - A_y.A_x^*) + |A_y|^2] \\ &= \frac{1}{2}[|A_x|^2 + |A_y|^2 - 2Im(A_x.A_y^*)] \\ < |H_y|^2 > &=< |(H_y)(H_y)^*| > \\ &= \frac{1}{4}[A_x.(1-i) + A_y.(1+i)].[A_x^*.(1+i) + A_y^*.(1-i)] \\ &= \frac{1}{2}[|A_x|^2 - i.(A_x.A_y^* - A_y.A_x^*) + |A_y|^2] \\ &= \frac{1}{2}[|A_x|^2 + |A_y|^2 + 2Im(A_x.A_y^*)] \end{aligned} \tag{E.38}$$

Hence the intensity difference between the two channels is :

$$< |H_x|^2 > - < |H_y|^2 >= -2Im(A_x.A_y^*)] \tag{E.39}$$

This is our BD-RIKE signal. Noticeable point is that RIKE signal is enhanced by the factor A_x.

Configuration(2):$2\alpha = -\frac{3\pi}{4} + k\pi$

$$\begin{aligned} H_x &= \frac{1}{2}[A_x.(1+i) - A_y.(1-i)]e^{i\omega t} \\ H_y &= \frac{1}{2}[-A_x.(1-i) + A_y.(1+i)]e^{i\omega t} \end{aligned} \tag{E.40}$$

Performing the similar calculations as we did for configuration(1), we will arrive at the result:

$$< |H_x|^2 > - < |H_y|^2 >= 2Im(A_x.A_y^*)] \tag{E.41}$$

Equations (E.39) and (E.41) differ only in negative sign which means that in one configuration, X-polarized intensity is higher than the Y-polarized one while in other configuration it is just opposite, but they are equal in magnitude.

Bibliography

[1] P. D. Maker and R. W. Terhune. Study of optical effects due to an induced polarization third order in the electric field strength. *Phys. Rev. A*, 137:801–818, 1963.

[2] M. Muller and A. Zumbusch. Coherent anti-stokes raman scattering microscopy. *Chem. Phys. Chem.*, 8:21562170, 2007.

[3] J. L. Oudar, R. W. Smith, and Y. R. Shen. Polarization-sensitive coherent anti-stokes raman spectroscopy. *Appl. Phys. Lett.*, 34:758–760, 1979.

[4] Ji-Xin Cheng, L. D. Book, and X. S. Xie. Polarization coherent anti-stokes raman scattering microscopy. *Opt. Lett.*, 26:1341–1343, 2001.

[5] A. Yu. Chikishev, G. W. Lucassen, N. I.Koroteev, C. Otto, and J. Greve. Polarization sensitive coherent anti-stokes raman scattering spectroscopy of the amide i band of proteins in solutions. *J. Biophys.*, 63:976–985, 1992.

[6] A. Yu. Chikishev N. I. Koroteev, C. Otto, and J. Greve. Polarization sensitive cars of the amide i band of pure and liganded chymotrypsin. *J. Raman. Spectrosc.*, 27:893–896, 1996.

[7] A. Pott, T. Doerk, J Ehlbeck, J. Hoschele, and J. Steinwandel. Polarization sensitive coherent anti-stokes raman scattering applied to the detection of no in a microwave discharge for reduction of no. *J. Phys. D*, 31:2485–2498, 1998.

[8] N. Nissum, J. M. Funk, and W. Kiefer. Polarization sensitive resonance cars spectroscopy of magnesium octaethylporphine. *J. Raman. Spectrosc.*, 30:605–610, 1999.

[9] Y. Saito, T. Ishibashi, and H. Hamaguchi. Polarization-resolved coherent anti-stokes raman scattering (cars) spectroscopy: A new probe of molecular symmetry throughaccurate determination of the raman depoalrization ratio. *J. Raman. Spectrosc.*, 31:725–730, 2000.

[10] E. O. Potma, C. L. Evans, and X. S. Xie. Heterodyne coherent anti-stokes raman scattering (cars) imaging. *Opt. Lett.*, 31:241–243, 2006.

[11] B. von Vacano, T. Buckup, and M. Motzkus. High-sensitive single beam heterodyne coherent ant-stokes raman scattering. *Opt. Lett.*, 31:2495–2497, 2006.

[12] M. Jurna, J.P. Korterik, C. Otto, and H.L. Offerhaus. Shot noise limited heterodyne detection of cars signals. *Opt. Express*, 15:15207–15213, 2007.

[13] F. Ganikhanov, C. L. Evans, B. G. Saar, and X. S. Xie. High-sensitivity vibrational imaging with frequency modulation coherent anti-stokes raman scattering (fm cars) microscopy. *Opt. Lett.*, 31:1872–1874, 2006.

[14] Y. S. Yoo, D. H. Lee, and H. Cho. Differential two-signal picosecond pulse coherent anti-stokes raman scattering microscopy by using a dual-mode optical parametric oscillator. *Opt. Lett.*, 32:3254–3256, 2007.

[15] A. Volkmer, L. D. Book, and X. S. Xie. Time-resolved coherent anti-stokes raman scattering microscopy: Imaging based on raman free induction decay. *Appl. Phys. Lett.*, 80:1505–1507, 2002.

[16] R. D. Hancock, F. R. Schauer, R. P. Lucht, and R. L. Farrow. Dual-pump coherent anti-stokes raman scattering measurements of nitrogen and oxygen in a laminar jet diffusion flame. *Appl. Opt.*, 36:3217–3226, 1997.

[17] J. Borysow, R. H. Taylor, and J.W. Keto. Raman induced kerr effect spectroscopy using pulsed lasers. *Optics Comm.*, 68:8086, 1988.

[18] C. W. Freudiger, M. B. J. Roeffaers, X. Zhang, B. G. Saar, W. Min, and X. S. Xie. Optical heterodyne-detected raman-induced kerr effect (ohd-rike) microscopy. *J. Phys. Chem. B*, jp1113834:A–H, 2011.

[19] C. W. Freudiger, W. Min, B. G. Saar, S. Lu, G. R. Holtom, C. He, J. C. Tsai, J. X. Kang, and X. S. Xie. Label-free biomedical imaging with high sensitivity by stimulated raman scattering microscopy. *Science*, 322:1857–61, 2008.

[20] R. Yuste. Fluorescence microscopy today. *Nat. Methods*, 2:902–904, 2005.

[21] M. R. Arnison, K.G. Larkin, C.J.R. Sheppard, N.I. Smith, and C. J. Cogswell. Linear phase imagimg using differential interference contrast microscopy. *J. Microsc.*, 214:7–12, 2004.

[22] R.D.Allen, N.S.Allen, and J.L.Travis. Video-enhanced contrast, differential interference contrast(a vec-dic)microscopy-a new method capable of analyzing microtubul-related mobility in the recticulopodial network of allogromia laticollaris. *Cell Motil. Cytoskeleton*, 1:291–302, 1981.

[23] S. Nie and S. R. Emory. Probing single molecules and single nanoparticles by surface-enhanced raman scattering. *Science*, 21:1102–1106, 1997.

[24] E. C. Le Ru, E. Blackie, M. Meyer, and P. G. Etchegoin. Surface enhanced raman scattering enhancement factors: A comprehensive study. *J. Phys. Chem. C*, 111:13794–13803, 2007.

[25] Sean J. Mulligan and Barin A. MacVcar. Two-photon fluoroscence microscopy: Basic principles, advangeages and risks. *Modern Research and Educational Topics in Microscopy*, 2007.

[26] M. Muller, J. Squier, K.R.Wilson, and G.J.Brakenhoff. 3d-microscopy of transparent objects using third-harmonic generation. *J. Microsc.*, 191:266–274, 1998.

[27] W.S. Warren, M.C. Fischen, and Y.T. Novel nonlinear contrast improves deep tissue microscopy. *Laser Focus World*, 43:99–103, 2007.

[28] Ye T., Fu D., and W. S. Warren. Nonlinear absorption microscopy. *Photochem. Photobiol.*, 85:631–45, 2009.

[29] Shoichi Yamaguchi and Tahei Tahara. Two-photon absorption spectrum of all trans retinal. *Chem. Phys. Lett.*, 376:237–243, 2003.

[30] C.V. Raman and K.S. Krishnan. A new type of secondary radiaion. *Nature*, 121:501–502, 1928.

[31] G. Landsherg and L. Mandelstam. *J. the Russian Physico-Chemical Society, Physics section*, 60:335, 1928.

[32] W. Demtroder. *Laser Spectroscopy.* Springer, third ed. edition, 2002.

[33] Iam Choon Khoo. *Liquid Crystals*, volume II. Wiley-Interscience, 2007.

[34] W. Min, S. Lu, M. Rueckel, G. R. Holtom, and X. S. Xie. Near-denerate four-wave -mixing microscopy. *Nano Lett.*, 9:2423–2426, 2009.

[35] Y. Prior. A complete expression for the third-order susceptibility ($\chi^{(3)}$)-perturbative and diagrammatic approaches. *IEEE J. Quantum Electron.*, QE-20:37–42, 1984.

[36] R. H. Pantell and H. E. Putoff. *Fundamentals of Quamtum electronics.* Wiley, New York, 1969.

[37] P. Lallemand and A. Anderson. *The Raman Effect*, volume I. 1971.

[38] G. L. Eesley. Coherent raman spectroscopy. *J. Quant. Spectrosc. Radial. Transfer*, 22:507–576, 1979.

[39] R. W. Terhune. *Bull. Am. Phys. Soc.*, 8:359, 1963.

[40] A. Zumbusch, G.R. Holtom, and X. S. Xie. Three-dimensional vibrational imaging by coherent anti-stokes raman scattering. *Phys. Rev. Lett.*, 82:41424145, 1999.

[41] J. X. Cheng, A. Volkmer, L. D. Book, and X. S. Xie. An epi-detected coherent anti-stokes raman scattering (e-cars) microscope with high spectral resolution and high sensitivity. *J. Phys. Chem. B*, 105:1277–1280, 2001.

[42] A. Volkmer, Ji-Xin Cheng, and X. S. Xie. Vibrational imaging with high sensitivity via epidetected coherent anti-stokes raman scattering microscopy. *Phys. Rev. Lett.*, 87:023901, 2001.

[43] Ji-Xin Cheng and X. S. Xie. Coherent anti-stokes raman scattering microscopy: instrumentation, theory,and applications. *J. Phys. Chem. B*, 108:827840, 2004.

[44] I. W. Schie1, T. Weeks1, G. P. McNerney, S. Fore, J. K. Sampson, S. W. Hogiu, J. C. Rutledge, and T. Huser. Simultaneous forward and epi-cars microscopy with a single detector by timecorrelated single photon counting. *Opt. Express*, 16:2168–2175, 2008.

[45] Ji-Xin Cheng, A. Volkmer, and X. S. Xie. Theoretical and experimental characterization of coherent anti-stokes raman scattering microscopy. *J. Opt. Soc. Am. B*, 19:1363–1375, 2002.

[46] C.L.Evans, E.O. Potma, M. Puorishaag, D. Cote, C.P.Lin, and X.S. Xie. Chemical imaging of tissue in vivo with video-rate coherent anti-stokes raman scattering microscopy. *Proc. Natl. Acad. Sci. USA*, 102:1680716812, 2005.

[47] I.Toytman, K.Cohn, T. Smith, D. Simanovskii, and D. Palanker. Non-scanning cars microscopy using wide-field geometry. *SPIE proceedings*, 6442:1–7, 2007.

[48] I.Toytman, K.Cohn, T. Smith, D. Simanovskii, and D. Palanker. Wide-field coherent anti-stokes raman scattering microscopy with non-phase-matching illumination. *Opt. Lett.*, 32:1941–1943, 2007.

[49] C. Heinrich, S. Bernet, and M. Ritsch-Marte. Wide-field coherent anti-stokes raman scattering microscopy. *Appl. Phys. Lett.*, 84:816818, 2004.

[50] R. W. Boyd. *Nonlinear Optics*. 2003.

[51] N. Bloembergen. The stimulated raman effect. *Am. J. Phys.*, 35:9891023, 1967.

[52] M.D. Levenson and S.S. Kano. *Introduction to Nonlinear Laser Spectroscopy.* 1988.

[53] W. Min, C. W. Freudiger, S. Lu, and X. S. Xie. Coherent nonlinear optical imaging: Beyond fluorescence microscopy. *Annu. Rev. Phys. Chem.*, 62:507–530, 2011.

[54] Ji-Xin Cheng, A. Volkmer, L. D. Book, and X. S. Xie. Multiplex coherent anti-stokes raman scattering microspectroscopy and study of lipid vesicles. *J. Phys. Chem. B*, 106:8493–8498, 2002.

[55] Conor L. Evans and X. Sunney Xie. Coherent anti-stokes raman scattering microscopy: Chemical imaging for biology and medicine. *Annu. Rev. Anal. Chem.*, 1:883–909, 2008.

[56] J.J.Wynne. Nonlinear optical spectroscopy of $\chi^{(3)}$ in $linbo_3$. *Phys. Rev. Lett.*, 29:650–653, 1972.

[57] M. D. Levenson and N. Bloembergen. Dispersion of the nonlinear optical susceptibility tensor in centrosymmetric media. *Phys. Rev. B*, 10:4447–4463, 1974.

[58] M. D. Levenson and N. Bloembergen. Dispersion of the nonlinear optical susceptibilities of organic liquids and solutions. *J. Chem. Phys.*, 60:1323–1327, 1974.

[59] I. Itzkan and D. A. Leonard. Observation of coherent anti-stokes raman scattering from liquid water. *Appl. Phys. Lett.*, 26:106–108, 1975.

[60] I. Chabay, G. K. Klauminzer, and B. S. Hudson. Coherent anti-stokes raman spectroscopy (cars): Improved experimental design and observation of new higher-order processes. *Appl. Phys. Lett.*, 28:27–29, 1976.

[61] R. F. Begley, A. B. Harvey, R. L. Byer, and B. S. Hudson. A new spectroscopic tool: Coherent anti-stokes raman spectroscopy. *Am. Lab.*, 6:11–21, 1974.

[62] R. F. Begley, A. B. Harvey, R. L. Byer, and B. S. Hudson. Raman spectroscopy with intense, coherent, anti-stokes beams. *J. Chem. Phys.*, 61:2466–2467, 1974.

[63] N. Djaker, P.F. Lenne, and H. Rigneault. Vibrational imaging by coherent anti-stokes raman scattering (cars) microscopy. *SPIE*, 2004.

[64] E. O. Potma, D. J. Jones, J. X. Cheng, X. S. Xie, and J. Ye. High sensitivity cars microscopy with two tightly synchronized picosecond lasers. *Opt. Lett.*, 27:1168–1170, 2002.

[65] D. J. Jones, E. O. Potma, J. X. Cheng, X. S. Xie, and J. Ye. Synchronization of two passively mode-locked, ps lasers within 20 fs for coherent anti-stokes raman scattering microscopy. *Rev. Sci. Instr.*, 73:2843–2848, 2002.

[66] J. X. Cheng, K. Y. Jia, G. Zheng, , and X. S. Xie. Laser-scanning coherent anti-stokes raman scattering microscopy and applications to cell biology. *Biophys. J.*, 83:502–509, 2002.

[67] C. L. Evans and X. S. Xie. Coherent anti-stokes raman scattering microscopy: Chemical imaging for biology and medicine. *Annu. Rev. Anal. Chem.*, 1:883909, 2008.

[68] E. R. Andresen. Tunable light source for coherent anti-stokes raman scattering microspectroscopy based on the soliton self-frequency shift. *Opt. Lett.*, 31:1328–1330, 2006.

[69] Vikas Kumar, R. Osellame, R. Ramponi, G. Cerullo, and M. Marangoni. Background-free broadband cars spectroscopy from a 1-mhz ytterbium laser. *Opt. Express*, 19:15143–15148, 2011.

[70] E. R. Andresen, C. K. Nielsen, J. Thgersen, and S. R. Keiding. Fiber laser-based light source for coherent anti-stokes raman scattering microspectroscopy. *Opt. Express*, 15:4848–4856, 2007.

[71] F. Ganikhanov, S. Carrasco, and X. S. Xie. Broadly tunable dual-wavelength light source for coherent anti-stokes raman scattering microscopy. *Opt. Lett.*, 31:1292–1294, 2006.

[72] M. A. Marangoni, D. Brida, M. Quintavalle, G. Cirmi, F. M. Pigozzo, C. Manzoni, F. Baronio, A. D. Capobianco, and G. Cerullo. Narrow-bandwidth picosecond pulses by spectral compression of femtosecond pulses in second-order nonlinear crystals. *Opt. Express*, 15:8884–8891, 2007.

[73] M. Marangoni, D. Brida, M. Conforti, A. D. Capobianco, C. Manzoni, F. Baronio, G. F. Nalesso, C. De Angelis, R. Ramponi, and G. Cerullo. Synthesis of picosecond pulses by spectral compression and shaping of femtosecond pulses in engineered quadratic nonlinear media. *Opt. Lett.*, 34:241–243, 2009.

[74] F. Tauser, F. Adler, and A. Leitenstorfer. Widely tunable sub-30-fs pulses from a compact erbium-doped fiber source. *Opt. Lett.*, 29:516–518, 2004.

[75] A. N. Bordenyuk, H. Jayathilake, and A. V. Benderskii. Coherent vibrational quantum beats as a probe of langmuir-blodgett monolayers. *J. Phys. Chem. B*, 109:1594115949, 2005.

[76] D. W. McCamant, P. Kukura, and R. A. Mathies. Femtosecond broadband stimulated raman spectroscopy: Apparatus and methods. *Rev. Sci. Instrum.*, 75:49714981, 2004.

[77] E. R. Andresen, J. Thgersen, and S. R. Keiding. Spectral compression of femtosecond pulses in photonic crystal fibers. *Opt. Lett.*, 30:20252027, 2005.

[78] F. Raoult, A. C. L. Boscheron, D. Husson, C. Sauteret, A. Modena, V. Malka, F. Dorchies, and A. Migus. Efficient generation of narrow-bandwidth picosecond pulses by frequency doubling of femtosecond chirped pulses. *Opt. Lett.*, 23:11171119, 1998.

[79] H. Luo, L. Qian, P. Yuan, and H. Zhu. Generation of tunable narrowband pulses initiating from a femtosecond optical parametric amplifier. *Opt. Express*, 14:1063110635, 2006.

[80] K. Moutzouris, F. Adler, F. Sotier, D. Trlein, and A. Leitenstorfer. Multimilliwatt ultrashort pulses continuously tunable in the visible from a compact fiber source. *Opt. Lett.*, 31:1148–1150, 2006.

[81] M. M. Fejer, G. A. Magel, D. H. Jundt, and R. L. Byer. Quasi-phase-matched second harmonic generation: tuning and tolerances. *IEEE J. Quantum Electron.*, 28:2631–2654, 1992.

[82] D. Pestov, R. K. Murawski, G. O. Ariunbold, X. Wang, M. C. Zhi, A. V. Sokolov, V. A. Sautenkov, Y. V. Rostovtsev, A. Dogariu, Y. Huang, and M. O. Scully. Optimizing the laser-pulse configuration for coherent raman spectroscopy. *Appl. Phys. Lett.*, 316:265–268, 2007.

[83] H. Kano and H. Hamaguchi. Dispersion-compensated supercontinuum generation for ultrabroadband multiplex coherent anti-stokes raman scattering spectroscopy. *J. Raman Spectrosc.*, 37:411–415, 2006.

[84] Y. J. Lee and M. T. Cicerone. Vibrational dephasing time imaging by time-resolved broadband coherent anti-stokes raman scattering microscopy. *Appl. Phys. Lett.*, 92:041108, 2008.

[85] D. Heiman, R. W. Hellwarth, M. D. Levenson, and G. Martin. Raman-induced kerr effect. *Phys. Rev. Lett.*, 36:189–192, 1975.

[86] R. Righini. Ultrafast optical kerr effect in liquids and solids. *SCIENCE*, 262:1386–1390, 1993.

[87] G. LiNa, T. ZhiLie, and X. Da. Theoretical investigation on raman induced kerr effect spectroscopy in nonlinear confocal microscopy. *Sci China Ser G-Phys Mech Astron*, 51:788–796, 2008.

[88] D. Klenerman, D.L. Gerrard, H. Herman, and M.T. Macpherson. Optically heterodyned raman-induced kerr-effect spectroscopy using a white-light contiuum. *Chem. Phys. Lett.*, 168:579–583, 1990.

[89] A. Long Derek. *The Raman effect: A unified treatment of the theory of Raman scattering by molecules*. John Willey and sons Ltd., 2002.